



MSc in Quantum Physics

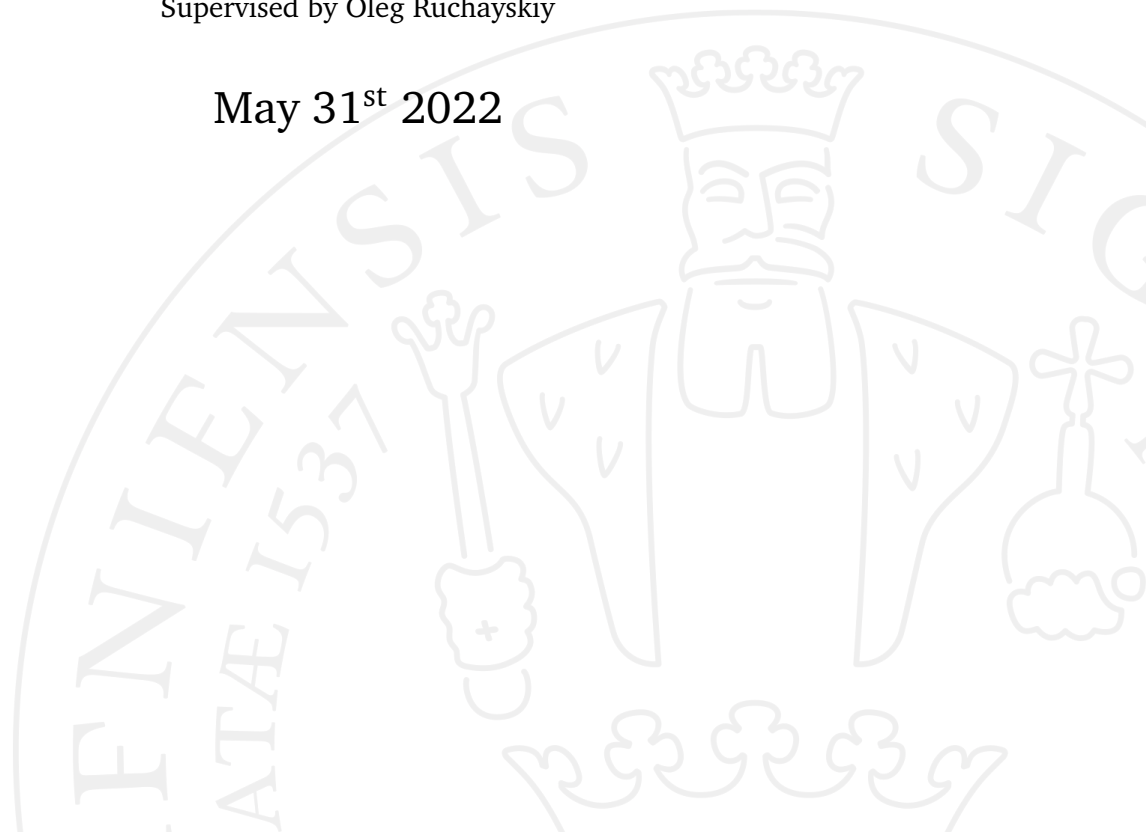
Piggyback Riding the Higgs Searches: A Hunt for Heavy Neutral Leptons with Tau Triggers

A study of the ATLAS experiment's sensitivity to Heavy Neutral
Leptons coupled to τ -leptons

Marie-Louise Riis

Supervised by Oleg Ruchayskiy

May 31st 2022



Marie-Louise Riis

Piggyback Riding the Higgs Searches: A Hunt for Heavy Neutral Leptons with Tau Triggers

MSc in Quantum Physics, May 31st 2022

Supervisor: Oleg Ruchayskiy

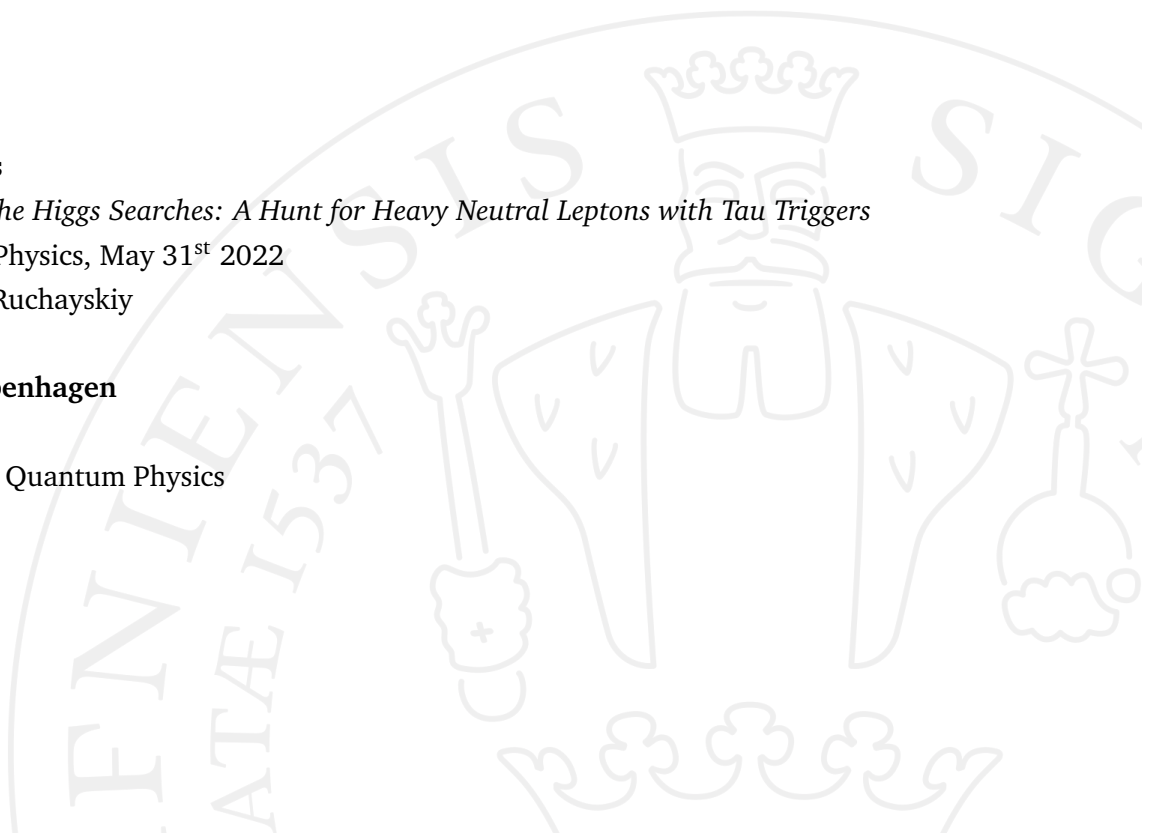
University of Copenhagen

Faculty of Science

Masters Degree in Quantum Physics

Blegdamsvej 17

2100 Copenhagen



Abstract

The Large Hadron Collider (LHC) at CERN is the most powerful particle accelerator today, performing collisions of protons at the highest achievable centre-of-mass energy, and a high *intensity of collisions* makes it possible to use its data to probe for *rare events*. LHC possesses sophisticated means, called *triggers*, in to single out events of interest from among the huge amount of background processes. A number these triggers have been specifically created to probe the nature of the Higgs boson.

In this thesis we demonstrate for the first time how the same technology could be used to search for hypothetical particles – Heavy Neutral Leptons (HNLs). HNLs can mediate neutrino oscillations and at the same time be responsible for generation of baryon asymmetry of the Universe. This makes them interesting candidates for ‘beyond the Standard Model particles’. HNLs have interactions with electron, muon and tau flavours, each governed by its own coupling constant. Up to now only couplings to the electron and muon flavors have been explored at the LHC and no probes of the interaction with the tau channel have been performed. We develop a search strategy that utilises existing LHC triggers tuned towards the detection of two tau-leptons.

We demonstrate that if production of heavy neutral lepton is accompanied by one or two jets triggers select a sizeable amount of the HNL-mediated events. The resulting signature process is a tri-lepton signal with two tau-leptons and one electron or muon and with extra jet(s). We demonstrate that the searches by the ATLAS experiment for such events hold a discovery potential or can improve the existing limits on the coupling strength between HNL and tau flavour by about an order of magnitude (during Run 3) or even more (during the high-luminosity phase). The improvements are possible within the mass range from about $5 \text{ GeV}/c^2$ to about $50 \text{ GeV}/c^2$. Our estimates are done at the signal-only level and may be over-optimistic. They demonstrate nevertheless the feasibility of piggy-back riding on the ‘shoulders’ of Higgs searches.

Contents

1	Introduction	1
2	The Standard Model - And Beyond	4
2.1	The Standard Model - A Brief Overview	4
2.1.1	Lepton flavour symmetries	6
2.2	The Need for Physics Beyond the Standard Model	7
2.2.1	Neutrino oscillations	7
2.2.2	Dark matter	8
2.2.3	Matter-antimatter asymmetry of the Universe	10
3	A Hypothesis of Heavy Neutral Leptons	12
3.1	Neutrino masses and extra neutrino states	12
3.1.1	An HNL Toy Model: One SM Neutrino and One HNL	12
3.1.2	Generalising to the case of several HNLs	16
3.1.3	Parameter counting for the Type I seesaw model	18
3.1.4	A Single HNL Coupled to the τ flavour	19
4	HNL Search Overview	21
5	The LHC & ATLAS	25
5.1	Large Hadron Collider	25
5.2	The ATLAS Experiment	25
5.3	ATLAS detector Geometry - A Brief Interlude	26
5.4	Tau-triggers at ATLAS	28
6	Data Generation	34
6.1	HeavyN Model	34
6.2	Data Generation	34
6.2.1	MadGraph & PYTHIA Setup	35
6.2.2	The Data Structure	36
7	Checks & Validations	39
7.1	A Couple of ‘Sanity’ Checks	39
7.2	Validation of HNL Decay Width	39

7.2.1	Charged Current	42
7.2.2	Neutral Current & Neutral-Charged Current Interference	43
7.2.3	QCD Corrections	44
7.2.4	Analytical Estimate vs. MadGraph	45
8	Data Analysis	48
8.1	Event Kinematics	48
8.2	Detector Efficiency	51
8.3	Prompt & Displaced Searches	56
8.4	On Rescaling a MadGraph HNL Cross Section	61
8.5	Single Event Sensitivity	62
8.5.1	SES Error Propagation	64
8.6	Exclusion Limits	65
9	Conclusion	72
10	Outlook & Future Work	75
11	Bibliography	77
A	HNL Invariant Mass Reconstructions with Varying Decay Widths	86
B	HNL Lorentz Factors	88
C	Approximation of Efficiencies after Decay	90
D	Solving for Single Event Sensitivity	93

Introduction

This thesis discusses physics at its most fundamental level – namely at the level of elementary particles, concerned with the smallest known constituents of matter. Before plunging into the details, let us very briefly describe its place in the “grand scheme of things”.

Over slightly more than a century a consistent picture of the world of particles has emerged. The model describing this received the name *the Standard Model* – a testament to that fact that it has passed numerous consistency checks, and that its many predictions have been successfully confirmed. Figure 1.1 below illustrates this by counterposing experimentally measured cross sections with their theoretical predictions within the Standard Model. One can see that the predictions hold across more than 13 orders of magnitude in cross sections (y-axis), which is an impressive feat!

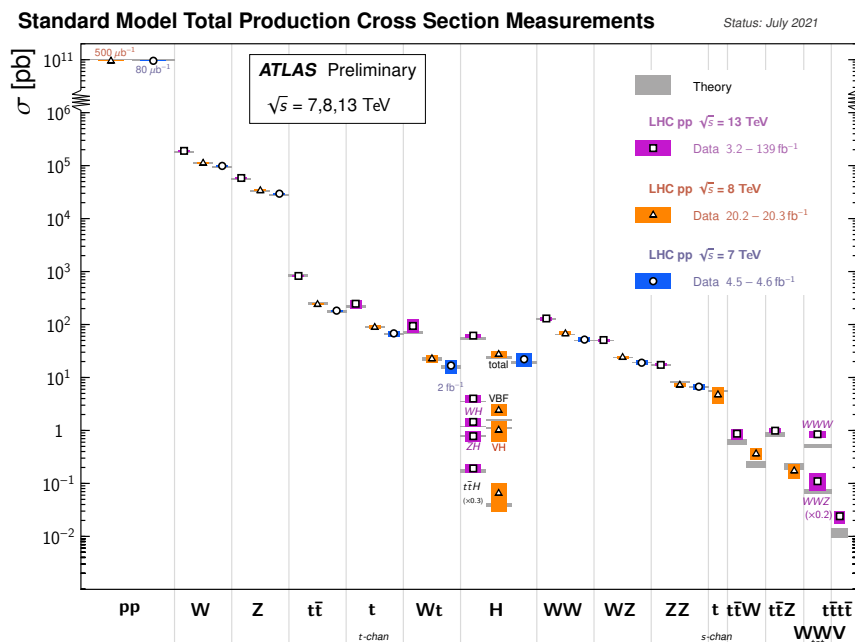


Figure 1.1.: Summary of production cross section measurements for several Standard Model processes (shown on the x-axis) performed by the ATLAS experiment at the LHC. Experimental measurements at different center-of-mass energies (\sqrt{s}) are shown in different colours. The corresponding theoretical predictions within the Standard Model are shown in grey. Figure from the ATLAS public note [1].

The most powerful particle physics accelerator, and thus the main tool to study the Standard Model, is the Large Hadron Collider (or LHC), located at CERN. It performs particle collision at enormous center-of-mass energies of 13 tera-electronvolt (13×10^{12} eV or 13 TeV is equivalent to 20.8 erg – quite a macroscopic energy) and at a rate of roughly 1 billion times per second. Overall these collisions generate an incredible amount of data, 160 Peta-bytes per year [2], which is being continuously analysed. The results of these analyses have been reported in more than **20 thousand research publications** (at the time of writing).^{*} Even if LHC had stopped today, analyses of already existing data would continue for decades, potentially bringing new unexpected discoveries, hidden in the LHC’s ‘big data’ [3].[†]

What then is the goal of this thesis? It proposes yet another analysis that can be performed at the Large Hadron Collider with existing and/or future data. This analysis is needed because along with the exploration of the Standard Model, researchers in particle physics are constantly searching for signals indicating new, yet undiscovered particles. There is no limit to the number of ideas for potential ‘new physics’ that could appear at the LHC. Therefore new ways to dissect the LHC’s ‘big data’ keep appearing. This thesis is one such idea. It utilises the power of the LHC *triggers* – hardware and software components, designed to reduce the data acquisition rate from Giga-Hertz (billions per second) to roughly kilo-Hertz (thousands per second) or even below. Special triggers have been designed for important Standard Model processes, tuned in particular towards the measurements of the Higgs boson. In this thesis we explore whether the same triggers can be used to probe for the signatures of some new particles, beyond the Standard Model (hence the somewhat tongue-in-cheek title with the ‘piggyback riding’).

The thesis is organised as follows. We begin in Chapter 2 with the brief introduction to the Standard Model and its observational drawbacks (also known as ‘*physics beyond the Standard Model*’). These drawbacks convince us that new as of yet unknown physics must exist, and with it potentially new particles. We then proceed with an introduction to a specific model of new physics – heavy neutral leptons in Chapter 3. We summarise in Chapter 4 what is known phenomenologically about these particles and identify interesting parts of the parameter space to be explored. In Chapter 5 we briefly overview the ATLAS detector and the way the searches for heavy neutral leptons are conducted at it. We then move towards the actual body of work, reviewing in Chapter 6

^{*}See this URL at the high-energy bibliographic database, <https://inspirehep.net> for up-to-date number.

[†]For example, Tevatron – LHC’s predecessor at Fermilab, USA – had its last collision on September 30, 2011. Some 10.5 years later the CDF collaboration reported the measurement of the W -boson mass performed with the astonishing precision of $(80\,433.5 \pm 9.4) \text{ MeV}/c^2$ and at statistically significant tension with the Standard Model prediction [4]. If confirmed, this result will indicate failure of the Standard Model at *precision frontier*.

the kind of Monte Carlo data we have generated, and how this is done. Chapter 7 is devoted to the data validation, where we perform various ‘sanity checks’ trying to ensure the correctness of our Monte Carlo data. Chapter 8 is devoted to the (Monte Carlo) data analysis, mimicking the actual LHC data analysis. Here we also summarise our results and explain why we believe our proposed analysis pipeline to be feasible, and that it allows us to probe a previously unexplored region of parameter space. We conclude in Chapter 9, where we also discuss where we have ‘cut corners’ in our analysis, as well as ideas for future development of this work.

The Standard Model - And Beyond

2.1 The Standard Model - A Brief Overview

Standard Model of particle physics (often referred to simply as *Standard Model* or SM for short) is a theory that describes all known elementary particles, their properties and interactions. The process of creation of the Standard Model took more than a century. The first elementary particle – electron – was discovered by the J. J. Thomson in 1897. The latest elementary particle – Higgs boson – was discovered at the Large Hadron Collider in CERN in 2012 [5, 6].*

The overall description of the content of the Standard Model and the properties of the elementary particles will take us too far afield [8]. Therefore, we will limit the discussion to a set of facts most important for the main subject of the current thesis.

The Standard Model includes 17 elementary particles that interact via three kinds of interactions (weak, strong and electromagnetic), see Table 2.1. Mathematically, these interactions are described via the *gauge principle*. The gauge group of the Standard Model is $SU(3) \times SU(2) \times U(1)$. Strong interactions are described by *Quantum Chromodynamics* – a non-Abelian gauge theory with the $SU(3)$ gauge group [9, 10]. Weak and electromagnetic interactions are described by the $SU(2) \times U(1)$ gauge group and are unified into the electroweak theory [11, 12, 13]. The electroweak symmetry is however *broken* via the Higgs mechanism [14, 15] leading to three massive mediators – the so-called *intermediate vector bosons* (W^\pm, Z^0) – and one massless photon. The Higgs particle is the manifestation of this mechanism.

The table of elementary particles (Figure 2.1) bears certain similarity with the chemical Periodic Table of elements. In particular, it also has *groups* (referred to as *generations* or *flavours* in this context). Particles in those groups have similar properties but increasing masses. Of specific importance for us are generation-related *global symmetries* that act in lepton sector (Table 2.2).

*A brief introduction to the history of the Standard Model and its main discoveries, can be found e.g. in [7].

Standard Model of Elementary Particles

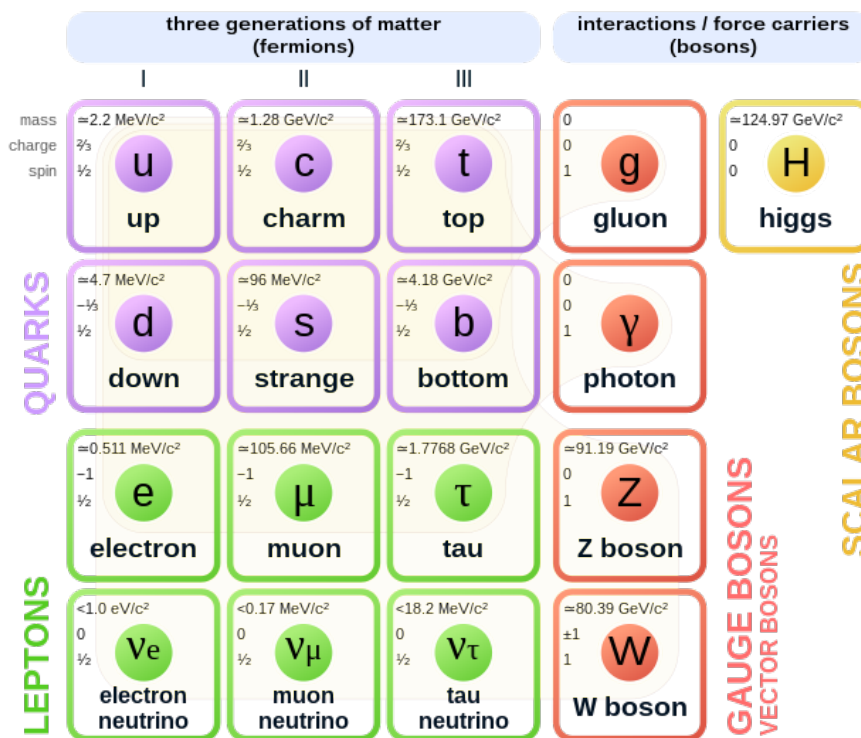


Figure 2.1.: Standard model of particle physics. Purple squares denote quarks, green squares – leptons, red squares are gauge bosons – mediators of interactions. Finally, the yellow square denotes the Higgs boson. The image is taken from the Wikipedia page https://en.wikipedia.org/wiki/Standard_Model.

	Particle name	Particle symbols	Interactions		
			Strong	Weak	Electromagnetic
Matter	Spin 1/2 particles				
	Quarks	$q \in \{u, d, s, c, b, t\}$	✓	✓	✓
	Charged leptons	$\ell \in \{e, \mu, \tau\}$	–	✓	✓
	Neutral leptons	$\nu \in \{\nu_e, \nu_\mu, \nu_\tau\}$	–	✓	–
Mediators	Spin 1 particles				
			Mediates interactions		
	Gluons	g	✓	–	–
	W -bosons	W^\pm	–	✓	–
	Z^0 -boson	Z^0	–	✓	–
	photon	γ	–	–	✓
	Spin 0 particle				
	Electroweak symmetry breaking and mass generation				
	Higgs boson	h^0	–	✓	–

Table 2.1.: Brief overview of the particle content of the Standard Model: their names, symbols, spins and types of interactions in which they participate or mediate.

Particle	L_e	L_μ	L_τ	L_{tot}
e^-	+1	0	0	+1
ν_e	+1	0	0	+1
μ^-	0	+1	0	+1
ν_μ	0	+1	0	+1
τ^-	0	0	+1	+1
ν_τ	0	0	+1	+1
other particles	0	0	0	0

Table 2.2.: Flavour lepton number assignments in the Standard Model. All antiparticles have opposite lepton numbers, so that $L_e(e^+) = -L_e(e^-) = -1$ or $L_\tau(\bar{\nu}_\tau) = -L_\tau(\nu_\tau) = -1$. The total lepton number, L_{tot} is defined as $L_e + L_\mu + L_\tau$.

2.1.1 Lepton flavour symmetries

For almost 30 years it has been known that involving charged leptons e^\pm, μ^\pm, τ^\pm demonstrate conservation of flavour lepton numbers (whose assignments are shown in Table 2.2). Searches for the processes like $\mu^\pm \rightarrow e^\pm + \gamma$ or $\mu^+ \rightarrow e^+ e^- e^+$ performed by experiments such as *SINDRUM II* [16], *MEG II* [17], *Mu2e* [18] have turned out negative, confirming that this symmetry exists and that the corresponding processes have branching ratios below 10^{-11} [8]. Additionally, searches for lepton flavour

violating processes in decays of neutral particles have been performed at the LHC via $Z^0 \rightarrow \ell_\alpha^\pm \ell_\beta^\mp$ and $h \rightarrow \ell_\alpha^\pm \ell_\beta^\mp$ with negative results [19, 20, 21, 22]., further confirming the symmetry.

Moreover, all processes, mediated by the “neutral current interactions” (*i.e.* proceeding via exchange of Z^0 -boson) preserve flavour (this observation is known as *the absence of flavour changing neutral current*) [23]. This, in particular concerns neutral-current scattering of neutrinos off nuclei:

$$\nu_\alpha + X \rightarrow \nu_\alpha + X' \quad (2.1.1)$$

All these numerous (non)observations are in line with the assumption of flavour lepton symmetries and the lepton charges assignments as in Table 2.2.

The conservation of all three lepton charges implies another conservation law – the conservation of total lepton number, defined as the sum of flavour numbers, $L_{tot} = L_e + L_\mu + L_\tau$. In the absence of it, a particle-antiparticle transition would become possible. The conservation of the total lepton number is being tested by experiments, known as *neutrinoless double beta decay* ($0\nu\beta\beta$), see e.g. [24] for review. It is the process when two neutrons undergo β -decays inside the nucleus with two electrons and no neutrinos being emitted. This process can only be possible if neutrinos are *virtual* and lepton number is not conserved.

2.2 The Need for Physics Beyond the Standard Model

2.2.1 Neutrino oscillations

Back in 1957 Bruno Pontecorvo proposed that “neutrinos” can change their “flavours” [25]. This was a bold proposal, given that electron neutrino was discovered a year before [26]) and it was still 5 years before neutrino of muon flavour was found [27]. The third generation of particles was not even discovered yet.

Fast-forward sixty five years. Today we know three generations of neutrinos (see Table 2.1). These particles are electrically neutral, participate in weak interactions in parity-violating ways. When the Standard Model was conceived, neutrinos were postulated as massless chiral particles [12].

In addition to that, unlike other SM leptons neutrinos *change flavours*, thus violating all three global lepton numbers, L_e, L_μ, L_τ . Namely, for a neutrino, created as a state $|\nu_\alpha\rangle$ there is a non-zero probability to be detected as a state of different flavour, $|\nu_\beta\rangle$ where $\alpha \neq \beta \in \{e, \mu, \tau\}$. Such a transition is called *neutrino oscillation* [28]. A Nobel prize of 2015 was awarded for the discovery of this phenomenon.

Neutrino oscillations imply first of all that neutrinos are *massive particles*. Indeed, neutrino oscillations are a manifestation of well-known quantum mechanical phenomena of a *mis-alignment* of the *charge* (flavour) states and *mass* (propagation) states. This mis-alignment is described by the so-called PMNS matrix (after Pontecorvo, Maki, Nakagawa, Sakata) [28]:

$$V^\nu \equiv \begin{pmatrix} 1 & 0 & 0 \\ 0 & \cos(\theta_{23}) & \sin(\theta_{23}) \\ 0 & -\sin(\theta_{23}) & \cos(\theta_{23}) \end{pmatrix} \begin{pmatrix} \cos(\theta_{13}) & 0 & \sin(\theta_{13})e^{-i\delta_{\text{CP}}} \\ 0 & 1 & 0 \\ -\sin(\theta_{13})e^{i\delta_{\text{CP}}} & 0 & \cos(\theta_{13}) \end{pmatrix} \begin{pmatrix} \cos(\theta_{12}) & \sin(\theta_{12}) & 0 \\ -\sin(\theta_{12}) & \cos(\theta_{12}) & 0 \\ 0 & 0 & 1 \end{pmatrix} \quad (2.2.1)$$

The corresponding parameters have been measured and constrained [29] and Figure 2.2. Neutrino oscillations experiments are classified based on how neutrinos are produced. Thus, there are

1. **Solar** neutrino experiments – neutrinos are produced in the Sun and reach Earth as a mixture of three flavour states.
2. **Atmospheric** neutrino experiments – neutrinos are produced when cosmic rays interact with the Earth’s atmosphere.
3. **Reactor** neutrino experiments – neutrinos are produced in nuclear reactors;
4. **Accelerator** neutrino experiments – neutrinos are produced at accelerators.

The combination of these experiments allow to determine 3 mixing angles, two mass square splittings and to obtain some restrictions on the CP phase, see Figure 2.2.

2.2.2 Dark matter

Modern cosmology is an impressive synergy between microscopic and cosmic scales. Thanks to it we can describe in remarkable details how the current complex state of the Universe had emerged from simple initial conditions. However, while The composition of the Universe is *measured* with high precision, some yet unknown particles are needed to *explain microscopic constituents* behind it.

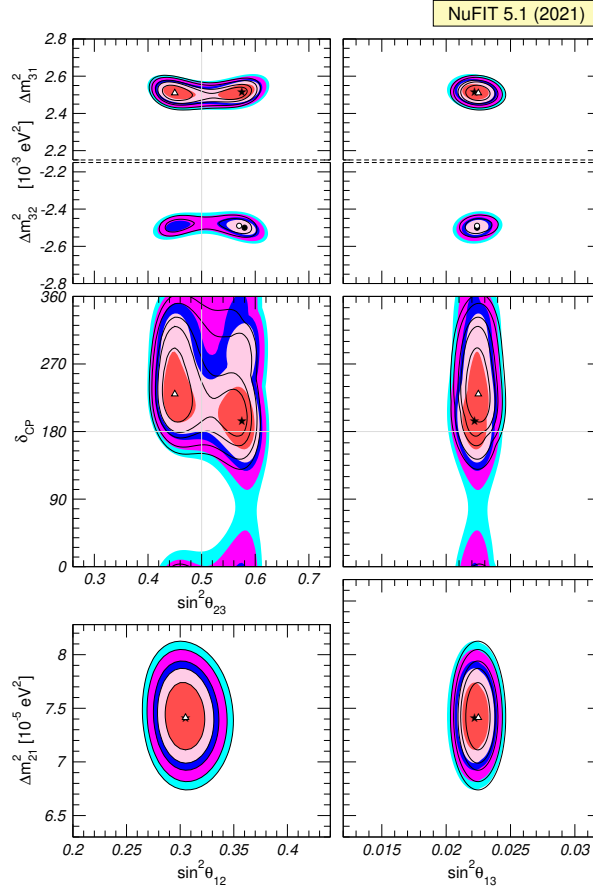


Figure 2.2.: Combined fits of all available neutrino experiments, providing constraints on parameters of the PMNS matrix and mass splittings. The definitions of the mixing angles and CP phase δ_{CP} can be found in Equation (2.2.1). The mass splittings determine oscillation frequency. Results are from the NuFIT project, [29].

Astronomers can account for movements of planets and satellites in our Solar system with astonishing precision without invoking any unknown substances. However, on larger scales (Galaxy and beyond) one inevitably detects a strong mismatch between the gravitational movement of objects and the amount of mass we can deduce with all our telescopes combined (see [31] for an excellent review). Cosmological measurements also indicate that about 25% of the total energy budget of the Universe does not interact with known particles or emit any light. This phenomenon is known as **dark matter** (see Figure 2.3).

Dark matter puzzle means that *either* the laws of gravity work differently on astronomically large scales *or* there exist unknown to us particles, copiously produced in the past and filling the Universe. The central hypothesis of today is that dark matter is made of particles. These particles are *not known to us!* The only known particle that fits the role – neutrino – accounts for about 1% of dark matter.

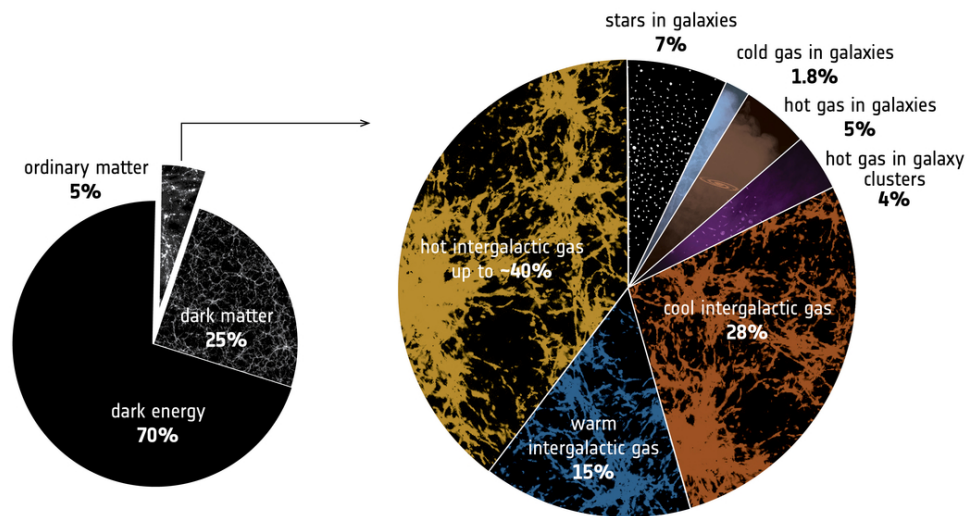


Figure 2.3.: “Cosmic pie”: dominant fractions of the total energy budget of the Universe: dark energy, dark matter, ordinary (or baryonic) matter. The latter constitutes all the visible objects in the Universe, including stars and planets. Figure courtesy of ESA [30].

The dark matter puzzle goes far beyond cosmology – it is one of our main indications that our "periodic table of elementary particles" is likely incomplete and more types of particles should exist. Any hints about the nature of dark matter provide valuable information about the properties of these particles and potential means of searches for them.

2.2.3 Matter-antimatter asymmetry of the Universe

According to modern cosmological model, the Universe in the past was hotter and denser with all the SM particles forming equilibrium thermal bath. With the Universe expansion, the temperature was dropping and therefore particles, whose masses significantly exceeded the temperature would annihilate. If the symmetry between matter and antimatter particles was *exact* – the cooling of the Universe left it almost void of all kinds of SM matter (excluding photons and neutrinos). The observations are clearly in contradiction with this prediction, implying that somewhere early in the Universe’s history the symmetry between matter and antimatter was violated. Once most of the matter-antimatter pairs annihilated, the leftover matter fills the Universe.

Its cosmological number density, n_B , is way below that of photons of the cosmic microwave background, n_γ , [32]:

$$\eta_B = \frac{n_B}{n_\gamma} = (1.23 \pm 0.02) \times 10^{-11}, \quad (2.2.2)$$

It turns out that this matter-antimatter asymmetry (often called *baryon asymmetry of the Universe* or *BAU*) cannot be generated via known particles and interactions. Indeed, as understood back in 1960s [33] 3 conditions should be satisfied to generate BAU from initially matter-antimatter symmetric state (see *e.g.* review [34]):

1. Baryon number (B) violation. As each proton or neutron carries 1 unit of baryon number, non-zero η_B implies non-conservation of the baryon number. This violation does occur in the SM via some quantum processes [34].
2. C and CP violation
 Particles and anti-particles must behave differently — otherwise particles and antiparticles could simultaneously use the B violation to make cancelling B and anti- B asymmetries. In the SM both C and CP *are* violated [35].
3. Departure of some of these above-mentioned processes from thermal equilibrium. In thermal equilibrium, there are no asymmetries in non-conserved quantum numbers (such as B). Therefore a non-equilibrium process (such as *e.g.* a phase transition) is needed. Unfortunately, in the SM electroweak phase transition is non-violent [36].

Thus, although all the necessary ingredients are present in the SM, the numbers “do not work out”. As a result, new particles are required to generate the matter-antimatter asymmetry of the Universe.

In the later sections we will introduce one such particles – *heavy neutral leptons*. These particles are very feebly interacting and therefore are out-of-equilibrium in the early Universe. The process of generation of BAU via heavy neutral leptons is known as *leptogenesis*.

A Hypothesis of Heavy Neutral Leptons

3.1 Neutrino masses and extra neutrino states

Neutrino oscillations imply that neutrinos are *massive* particles and that neutrino states with definite mass (*mass eigenstates*) do not have definite lepton flavour. Similarly, neutrino flavour eigenstates are *combinations* of these mass eigenstates. Schematically, this can be written as

$$|\nu_\alpha\rangle = \sum_i (V^\nu)_{\alpha i}^* |\nu_i\rangle \quad (3.1.1)$$

where the matrix $(V^\nu)_{\alpha i}$ is the PMNS matrix [28]. Oscillations are only possible if at least some of the states $|\nu_i\rangle$ have different masses, $m_i \neq m_j$ for $i \neq j$. As Standard Model neutrinos ν_α are strictly massless, *extra states* should be added to the SM Lagrangian to describe massive neutrino states. Next sessions will review models of neutrino masses.

3.1.1 An HNL Toy Model: One SM Neutrino and One HNL

The fermionic kinetic terms of the SM Lagrangian follow the form of the Dirac Lagrangian[37]:

$$\mathcal{L}_D^{\text{kin}} = \bar{\psi}(i\cancel{\partial} - m)\psi, \quad \text{where } \psi = \begin{pmatrix} \psi_L \\ \psi_R \end{pmatrix} \quad (3.1.2)$$

Here ψ is a 4-component Dirac spinor, $\bar{\psi} = \psi^\dagger \gamma^0$ is the adjoint spinor and $\psi_R(\psi_L)$ is a right-chiral(left-chiral) Weyl spinor. SM fermions are represented by Dirac spinors, and they obey the Dirac equation:

$$(i\cancel{\partial} - m)\psi = 0, \quad (3.1.3)$$

which are the equations of motion of the fermions. Writing these explicitly in terms of the chiral Weyl spinors (in Weyl basis), they become [38]:

$$i\cancel{\partial}\psi_L = m\psi_R \quad (3.1.4)$$

$$i\cancel{\partial}\psi_R = m\psi_L \quad (3.1.5)$$

for $m = 0$ the equations decouple, however for massive fermions the right- and left-chiral components are coupled to each other as they propagate. Since the SM neutrino oscillations have been observed (Sec. 2.2.1), there is no way around introducing a neutrino mass term. This requires a right-chiral neutrino component*.

There are two general, renormalisable and Lorentz invariant, types of fermion mass terms: Dirac and Majorana [see e.g. 35]. Owing to the chiral nature of weak interactions, left- and right-chiral components of the particles carry different $SU(2)$ and $U(1)$ hyper-charges. As a result, the Dirac mass term can only be generated from a Yukawa interaction between a fermion field and a scalar field, namely the Higgs field [37]:

$$\mathcal{L}_{\text{Yuk}} = -y\bar{L}_\alpha\tilde{H}\psi_R^{(\alpha)} + h.c., \quad L_\alpha = \begin{pmatrix} \nu_\alpha \\ l_\alpha^- \end{pmatrix}_L \quad \text{and} \quad \tilde{H} = -\frac{1}{\sqrt{2}} \begin{pmatrix} v \\ 0 \end{pmatrix} \quad (3.1.6)$$

where y is the dimensionless Yukawa coupling, L_α the left-chiral $SU(2)$ doublet, $\psi_R^{(\alpha)}$ the $SU(2)$ right-chiral singlet, and \tilde{H} is the (conjugated) Higgs doublet, $\tilde{H}_a \equiv \epsilon_{ab}H_b$, which after symmetry breaking takes the form shown in Eq. (3.1.6), where v is the vacuum expectation value. Thus, after the symmetry breaking the Yukawa interaction gives rise to the Dirac mass term, containing both left- and right-chiral Weyl spinors:

$$\mathcal{L}_D^{\text{mass}} = -m_D \begin{pmatrix} \psi_L^\dagger & \psi_R^\dagger \end{pmatrix} \gamma^0 \begin{pmatrix} \psi_L \\ \psi_R \end{pmatrix} = -m_D(\psi_R^\dagger\psi_L + \psi_L^\dagger\psi_R) \quad (3.1.7)$$

$$= -m_D\bar{\psi}\psi, \quad (3.1.8)$$

where $m_D = \frac{yv}{\sqrt{2}}$. Such a neutrino mass term can be constructed in the same way as for all the fermions of the SM, since its gauge invariance is achieved through the Higgs mechanism after spontaneous symmetry breaking.

As mentioned previously, Majorana mass term breaks gauge invariance. Therefore for the left-chiral neutrino components is not compatible with the SM gauge invariance.

*Technically a Majorana mass term could be constructed of the left-chiral (right-chiral) (anti)neutrino spinors. However since the (anti)neutrino spinors are not singlets under the SM gauge symmetries, a gauge invariant form of such a term can only be constructed as ‘‘operator of mass dimension 5’’ (i.e. non-renormalizable operator, known as Weinberg operator [39]). It should be stressed that there are *many* non-renormalizable operators, see e.g. [40]. Therefore we will not further pursue this wide direction.

However, the right-handed components, ψ_R are *gauge-singlets* not only with respect to the $SU(2)$ gauge group, but also for the $U(1)$ hyper-charge one. Indeed, hypercharges of the Higgs and neutrino are the opposite [see e.g. 37] and therefore ψ_R carries zero hyper-charge. As a result, for the right-chiral components of the neutrino, ψ_R , one can write a renormalizable Majorana mass term:

$$\mathcal{L}_M = -\frac{1}{2}M(\psi_R^\dagger\sigma_2\psi_R^* + \psi_R^T\sigma_2\psi_R), \quad (3.1.9)$$

where σ_2 is the Pauli matrix. Defining a spinor $\psi = \begin{pmatrix} \psi_R \\ 0 \end{pmatrix}$, it transforms as follows under charge conjugation:

$$C : \psi \rightarrow -i\gamma_2\psi^* = \begin{pmatrix} 0 \\ i\sigma_2\psi_R^* \end{pmatrix} \equiv \psi^c \quad (3.1.10)$$

From this a four component Majorana spinor can be constructed, consisting only of one chirality, and which is invariant under charge conjugation:

$$\psi_M = \psi + \psi^c = \begin{pmatrix} \psi_R \\ i\sigma_2\psi_R^* \end{pmatrix}, \quad \psi_M^c = \psi_M \quad (3.1.11)$$

Since the charge conjugated state of a spinor is equivalent to antiparticle, introducing a Majorana mass term introduces a direct coupling between a particle and its antiparticle, see Fig. 3.1.

Since the right-chiral neutrino and the left-chiral anti-neutrino are singlets under all the symmetries of the SM, any term constructed using only these will respect the SM gauge invariance. Adapting the notation $\psi_L^{(\nu)} = \nu_L$ and $\psi_R^{(\nu)} = N_R$ to denote neutrino Weyl spinors, the Dirac and Majorana mass terms can be combined and written as:

$$\mathcal{L}_{D+M}^{\text{mass}} = -\frac{1}{2} \begin{pmatrix} \nu_L^\dagger & N_R^T \end{pmatrix} \underbrace{\begin{pmatrix} 0 & m_D \\ m_D & M_M \end{pmatrix}}_M \begin{pmatrix} \nu_L^c \\ N_R \end{pmatrix} + h.c. \quad (3.1.12)$$

Here N_R is the added right-chiral neutrino component, a singlet under the SM gauge symmetries, and therefore ‘sterile’ in all SM interactions - hence the name ‘sterile neutrino’ is often used interchangeably with the right-chiral neutrino component.

Defining the spinors $N_\nu = \begin{pmatrix} \nu_L^c \\ N_R \end{pmatrix}$ and $\bar{N}_\nu = (\bar{\nu}_L \quad \bar{N}_R^c)$, Eq. (3.1.12) can be written more succinctly as:

$$\mathcal{L}_{D+M}^{\text{mass}} = -\frac{1}{2} \bar{N}_\nu \mathbf{M} N_\nu + h.c. \quad (3.1.13)$$

The spinors ν_L and N_R within N_ν represent the left- and right-chiral neutrino components as they interact with (or don't in the case of N_R) the weak force, i.e. 'flavour' or 'charge' basis. The mass matrix \mathbf{M} in Eq. (3.1.13) contains off-diagonal elements, and so ν_L and N_R are not the neutrino mass eigenstates. The mass eigenstates are found by a change of basis into one in which \mathbf{M} is diagonal. In the basis where \mathbf{M} the components of the spinor N'_ν will be the neutrino mass eigenstates, i.e. they are eigenstates of the free Hamiltonian, and so represent the neutrino states as they propagate space-time.

The rotation, in this two-dimensional example with only one added right-chiral neutrino, can be written in the form the rotation matrix:

$$O = \begin{pmatrix} \cos(\theta) & \sin(\theta) \\ -\sin(\theta) & \cos(\theta) \end{pmatrix} \quad (3.1.14)$$

The eigenvalues of \mathbf{M} are

$$m_{\nu,N} = \frac{1}{2} \left(M_M \mp M_M \sqrt{1 - \left(\frac{2m_D}{M_M} \right)^2} \right), \quad (3.1.15)$$

with the corresponding eigenstates $\begin{pmatrix} \nu \\ N \end{pmatrix}$. These eigenstates in the basis where the mass matrix is diagonal, often referred to as mass eigenstates are given by:

$$\nu = \cos(\theta) \nu_L - \sin(\theta) N_R^c \approx \nu - \theta N_R^c \quad (3.1.16)$$

$$N = \sin(\theta) \nu_L^c + \cos(\theta) N_R \approx N_R + \theta \nu^c \quad (3.1.17)$$

where the approximation is $\theta \ll 1$. This approximation is equivalent to the condition that $m_D \ll M_M$ under which the *mixing angle* θ is expressed via the parameters of the Lagrangian (3.1.13) via

$$\theta \equiv \frac{m_D}{M_M} \quad (3.1.18)$$

(Assuming the mixing angle θ to be very small is reasonable, since right-chiral neutrinos have not yet been observed [41]). The states ν and N , defined by Eqs. (3.1.16) are referred to as '*mass (eigen)states*', representing the particle states propagating with the well-defined dispersion relation. The state ν is – light neutrino state, while the state N

receives the name of *heavy neutral lepton* (or HNL). The states ν_L and N_R are referred to as ‘*charge eigenstates*’ or ‘*flavour eigenstates*’, representing the particle states as they interact weakly.

Inverting the relation (3.1.16) allows to find interactions of HNL. Remembering the weak interactions of ν_L from the SM, written in terms of flavour/charge eigenstates [35]:

$$\mathcal{L}_{CC} = \frac{g}{\sqrt{2}} \bar{e} \gamma^\mu (1 - \gamma_5) \nu_L W_\mu \quad (3.1.19)$$

$$\mathcal{L}_{NC} = \frac{g}{2 \cos \theta_W} \bar{\nu} \gamma^\mu (1 - \gamma_5) \nu_L Z_\mu \quad (3.1.20)$$

Changing basis and writing the Weak interactions in term of mass eigenstates instead, they become:

$$\tilde{\mathcal{L}}_{CC} = \frac{g \theta_N}{\sqrt{2}} \bar{e} \gamma^\mu (1 - \gamma_5) N W_\mu \quad (3.1.21)$$

$$\tilde{\mathcal{L}}_{NC} = \frac{g \theta_N}{2 \cos \theta_W} \bar{\nu} \gamma^\mu (1 - \gamma_5) N Z_\mu + \mathcal{O}(\theta^2) \quad (3.1.22)$$

And so N ‘inherits’ the interaction types of the flavour eigenstate ν_L , but suppressed by the mixing angle $\theta_N \ll 1$. This opens the door to exciting phenomenology of heavy neutral leptons, which could lead to eventual detection, as opposed to the truly ‘sterile’ particle N_R .

3.1.2 Generalising to the case of several HNLs

Before proceeding with the phenomenology of HNLs, a brief overview of a model containing multiple HNLs is in order. In Sec. 3.1.1 we outlined a toy version of the so-called “*Type-1 seesaw model*” [8, ch. 14] in which only one SM neutrino (left-chiral) and one HNL (right-chiral) were included. However, the SM sector includes 3 neutrino flavours, and a hypothetical dark sector could contain an arbitrary number, \mathcal{N} , of HNLs. Because of the observed SM neutrino oscillations, it is known that the mass eigenstates (ν_1, ν_2, ν_3) of the SM neutrinos are not degenerate, and so at least two of these have a non-zero mass (because two different mass splittings have been measured, see *e.g.* Figure 2.2 in Section 2.2.1). In the minimal case, where one of the three SM neutrinos is massless, *two HNLs* are required to provide the additional degrees of freedom, corresponding to the two neutrino masses. If all three SM neutrinos are massive masses, at least three HNLs would be required. There is in principle no upper limit to the number of HNLs it is possible to add to the SM, and so the following generalisation, following [42][43], is made for 3 SM neutrino flavours and \mathcal{N} HNLs.

Before Electro-Weak symmetry breaking (EWSB) the general form of the Seesaw type-1 Lagrangian is:

$$\mathcal{L}_{\text{seesaw}} = \mathcal{L}_{SM} + \frac{i}{2} \nu_{RI}^\dagger \bar{\sigma}^\mu \partial_\mu \nu_{RI} - (Y_{\alpha I}^\nu)^* (L_\alpha \cdot \tilde{\phi})^\dagger \nu_{RI} - \frac{M_I}{2} \nu_{RI}^T \nu_{RI} + h.c. \quad (3.1.23)$$

Here ν_{IR} are the new right-chiral states with $I = 1, \dots, \mathcal{N}$, and L_α is the SM left chiral SU(2) doublet $L_\alpha = \begin{pmatrix} \nu_\alpha \\ l_\alpha^- \end{pmatrix}_L$, where $\alpha = e, \mu, \tau$ and $\tilde{H}_\alpha = \varepsilon_{ab} H_b^*$, where H is the Higgs

doublet. This can after EWSB can be written as $H = \frac{1}{\sqrt{2}} \begin{pmatrix} 0 \\ v \end{pmatrix}$, where v is the vacuum expectation value (VEV). And so $(L_\alpha \cdot \tilde{H}) = \frac{v}{\sqrt{2}} \nu_{L\alpha}$ after EWSB. Now it is seen that the terms:

$$\mathcal{L}_D = - (Y_{\alpha I}^\nu)^* \frac{v}{\sqrt{2}} \nu_{L\alpha}^\dagger \nu_{RI} + h.c. \quad (3.1.24)$$

$$= - (m_D)_{\alpha I} \left(\nu_{RI}^\dagger \nu_{L\alpha} + \nu_{L\alpha}^\dagger \nu_{RI} \right) \quad (3.1.25)$$

become the Dirac mass terms with $(m_D)_{\alpha I} = \frac{v}{\sqrt{2}} (Y_{\alpha I}^\nu)^*$, resembling the Dirac mass term of Eq. (3.1.8). The combination of the Dirac and Majorana mass terms now resembles the expression (3.1.12) albeit in the matrix form:

$$\mathcal{L}_{D+M}^{\text{mass}} = -\frac{1}{2} \begin{pmatrix} \nu_L^T & (\nu_R^c)^T \end{pmatrix} \underbrace{\begin{pmatrix} 0 & m_D^T \\ m_D & M_M \end{pmatrix}}_{\mathbf{M}} \begin{pmatrix} \nu_L^c \\ \nu_R \end{pmatrix} + h.c. \quad (3.1.26)$$

$$\text{where } M_M = \begin{pmatrix} M_1 & & \\ & \ddots & \\ & & M_N \end{pmatrix}, \nu_L = \begin{pmatrix} \nu_{Le} \\ \nu_{L\mu} \\ \nu_{L\tau} \end{pmatrix} \text{ and } \nu_R = \begin{pmatrix} \nu_{R1} \\ \vdots \\ \nu_{RN} \end{pmatrix} \quad (3.1.27)$$

Like in Sec. 3.1.1 the flavour eigenstates, $\nu_{L\alpha}$ and ν_{RI} , are not aligned with the mass eigenstates.

The diagonalization of the mass term (3.1.26) allows to define *mixing angles*, similarly to the toy-model in Section 3.1.1. To obtain the relation between flavour and mass eigenstates the mass matrix \mathbf{M} can be diagonalised, using ‘Takagi’s factorisation’:

$$\mathbf{V}^T \mathbf{M} \mathbf{V} = \begin{pmatrix} m_1 & & \\ & \ddots & \\ & & m_{\mathcal{N}+3} \end{pmatrix} \quad (3.1.28)$$

where the unitary matrix \mathbf{V} has the form:

$$\mathbf{V} = \begin{pmatrix} V^\nu & \Theta \\ -\Theta^\dagger V^\nu & \mathbb{1} \end{pmatrix} \quad (3.1.29)$$

where V^ν is the PMNS matrix. The $3 \times \mathcal{N}$ matrix Θ is defined via

$$\Theta_{\alpha I} \equiv \frac{Y_{\alpha I}^\nu v}{M_I}. \quad (3.1.30)$$

The matrix \mathbf{V} performs the rotation from the *flavour* states ($\nu_{L\alpha}$ and ν_{RI} to the *mass eigenstates* ν_m, N_m :

$$\underbrace{\begin{pmatrix} \nu_{m_1} \\ \nu_{m_2} \\ \nu_{m_3} \\ N_{m_1} \\ \vdots \\ N_{m_{\mathcal{N}}} \end{pmatrix}}_{\text{Mass states}} = \mathbf{V} \underbrace{\begin{pmatrix} \nu_e \\ \nu_\mu \\ \nu_\tau \\ N_1^c \\ \vdots \\ N_{\mathcal{N}}^c \end{pmatrix}}_{\text{Flavour states}} \quad (3.1.31)$$

The mixing angles $\Theta_{\alpha I}$ are in general complex. The interaction matrix elements are proportional to them (see (3.1.21) and the next Chapter 4). However, production and decay probabilities depend on their absolute value only. Moreover, for several degenerate in mass HNL species these probabilities are summed over the species. Therefore it is convenient to introduce also the following quantities:[†]

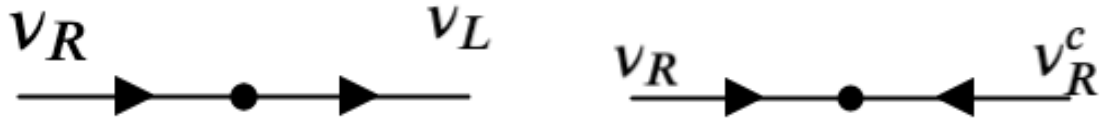
$$|\theta_{N\alpha}|^2 \equiv \sum_{I=1}^{\mathcal{N}} |\Theta_{\alpha I}|^2 \quad \text{as well as} \quad \theta_{\text{tot}}^2 \equiv \sum_{\alpha} |\theta_{N\alpha}|^2. \quad (3.1.32)$$

These quantities are real and non-negative and the results of experimental searches are usually expressed in their terms.

3.1.3 Parameter counting for the Type I seesaw model

It is instructive to count the number of extra parameters that the model with \mathcal{N} right-handed neutrinos brings. To begin with, it should be noted that the Majorana mass term is not invariant with respect to the global $U(1)$ transformations, such as $\nu_{RI} \rightarrow e^{i\lambda_I} \nu_{RI}$. Therefore, by suitable choice of the parameters λ_I one can ensure that the Majorana masses M_I are *real*. Once this redefinition of the right-chiral fields is done, the matrix $Y_{\alpha I}^\nu$ is a general complex $3 \times \mathcal{N}$ matrix. As such, it contains $3 \times \mathcal{N} \times 2$

[†]We note that there is no agreed standard for this notation. The corresponding mixing angles are often denoted by U_{α}^2 , by θ_{α}^2 (without the N subscript), by V_N^2 or $V_{N\alpha}^2$. We try to keep a consistent notation throughout this text, but different notations are encountered when we reproduce other works.



(a) Dirac mass term

(b) Majorana mass term

Figure 3.1.: Dirac (left) and Majorana (right) mass terms in the diagrammatic form. In both cases the vertex couples a left-chiral component with the right-chiral component. However, in the Dirac case the lepton number is conserved and thus there is a continuous flow of the lepton number (indicated by the arrows, pointing into the same direction). In the Majorana case, the left-chiral component is just charge conjugation of ν_R , i.e. ν_R^c . The charge conjugation flips the sign of the lepton number and therefore there is no continuous flow of the lepton number (indicated by the “colliding” arrows).

real parameters. However, we can still use the fact that all other terms of the SM Lagrangian are invariant with respect to the symmetry transformation, corresponding to the flavour lepton number: $L_\alpha \rightarrow e^{iq_\alpha} L_\alpha$. Thus, by suitable redefinition of the left-chiral doubles one can eliminate 3 parameters, leaving the total count to:

$$\text{Extra seesaw parameters} = \mathcal{N} + 3 \times \mathcal{N} \times 2 - 3 = 7\mathcal{N} - 3 \quad (3.1.33)$$

This number should be compared with the number of parameters, that can potentially be fixed in the neutrino sector. The PMNS matrix Eq. (2.2.1) contains 4 parameters. There are 3 masses (m_1, m_2, m_3) and two extra Majorana phases.[‡] Thus, in case of two HNLs, neutrino data can fix maximum 7 parameters (4 PMNS parameters, including the CP phase plus two masses and one Majorana phase). Formula (3.1.33) gives 11 parameters, thus leaving 4 of them unfixed: two HNL masses, a ratio of Yukawa couplings between two HNL “flavours” and a phase.

3.1.4 A Single HNL Coupled to the τ flavour

Parameter count (3.1.33), conducted in the previous Section shows that even in the simplest model with two HNLs, the mixing angles $|\theta_{N\alpha}|^2$ (see the definition (3.1.32)) are not uniquely fixed. Figure 3.2, left panel shows their allowed regions for normal (blue) and inverted (green) mass orderings. Looking at this Figure one can see that for the normal ordering, the mixing with electron neutrinos is always sub-dominant, not exceeding $\mathcal{O}(15\%)$ of the total mixing angle U_{tot}^2 . At the same time, the mixing, e.g.

[‡]Majorana masses of active neutrinos can in principle also be complex and by suitable redefinition of the neutrino states ν_i can be moved to the matrix V^ν . It is a convention to keep the PMNS matrix in the form (2.2.1) and assign Majorana phases to the neutrino masses.

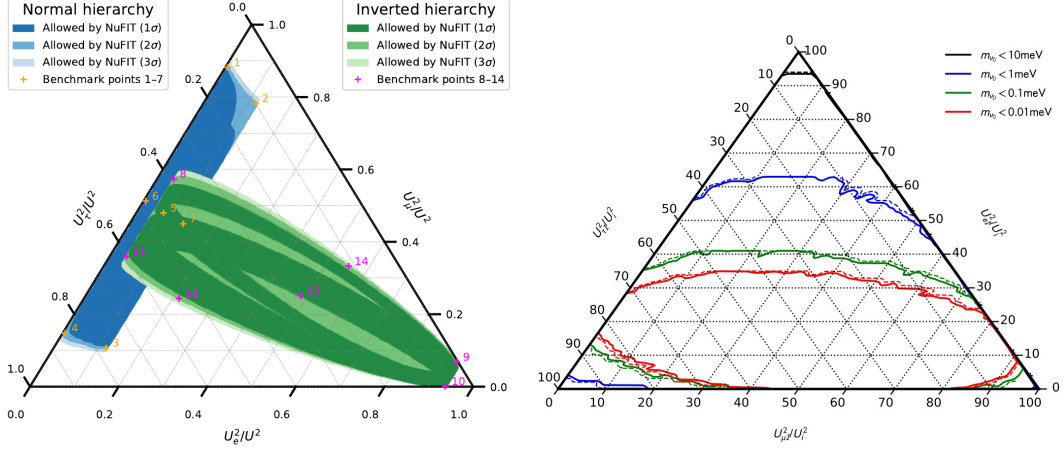


Figure 3.2.: Allowed regions of the mixing angles ratios $U_\alpha^2/U_{\text{tot}}^2$ as functions of unknown parameters (CP and Majorana phases, neutrino mass ordering, minimal neutrino mass, etc.). While in no cases do contours touch the corners of the triangle (which would constitute the mixing with a single flavour) the come *Left panel*: case of 2 HNLs with degenerate masses. The case of both ‘normal’ (blue) or ‘inverted’ (green) neutrino mass orderings are shown. Pink (orange) crosses with numbers show various benchmark datapoints that maximise/minimise some of the mixing angles. Figure from [42]. *Right panel* shows the case of 3 HNLs with degenerate masses for the normal neutrino mass ordering. The extend of the contours depend on the (unknown) mass of the lightest active neutrino, shown in the upper right corner. Figure from [44].

with τ -flavour can reach as much as 90% of the total mixings (benchmark points 3 and 4).

In the case of 3 HNLs, the situation may be even closer to the ‘single HNL dominance’, where $|\theta_{N\alpha}|^2 \approx \theta_{\text{tot}}^2$ (Figure 3.2, right panel, lower left corner). In this case $|\theta_{N\tau}|^2$ may constitute from 85% to more than 95% of the θ_{tot}^2 . One can also see that contours never enter the very corner of the ternary plot, demonstrating that, as expected, HNLs always couple at least to two flavours.

However, the existing LHC searches have been limited so far to the case of electron or muon single flavour dominance (see Section 4 below). This warrants the current investigation where the perspective of probing the mixing with the *tau*-flavour is analysed.

HNL Search Overview

Through the Dirac mass term HNLs “inherit” neutrino-like interactions with W^\pm , Z^0 and Higgs bosons. Schematic representation of these interactions is shown in Figure 4.1. In practical terms this means that HNLs can participate in any weak process in which neutrino can, if the process’s kinematics allows this. This in turn means that in any experiment where copious amounts of neutrinos are produced, searching for HNLs is a possibility.

Main production channels of HNLs include decays of on-shell vector bosons as well as (semi)leptonic decays of flavoured mesons and baryons [see e.g. 45, 46]. For example, a leptonic meson decay, e.g. $K^+ \rightarrow \mu^+ + \nu_\mu$ is accompanied by the decay $K^+ \rightarrow \mu^+ + N$, provided that this process is kinematically allowed (i.e. $M_N < m_K - m_\mu$).^{*} This creates the following “hierarchy” of experimental searches, depending on the HNL mass, M_N . For $M_N \leq m_B$ (the mass of B^\pm -mesons, $|b\bar{q}\rangle$) the HNLs are most efficiently produced in meson decays. Their searches are therefore mostly conducted at various fixed-target experiments, see e.g. [41]. Correspondingly, for $M_N \leq 2 \text{ GeV}$ (the mass of D^\pm mesons) HNLs can be produced in the charmed meson decay; below the kaon mass, $M_N \leq m_K$ they are produced in kaon experiments, etc.

Correspondingly, for $m_B < M_N < m_W, m_Z$ the main production channel becomes that of W/Z bosons decay. HNLs in the decay of Z^0 bosons were conducted at LEP [47]. Currently they are studied in the decays of W bosons produced at the Large Hadron Collider [48].[†]

Similarly, HNLs lighter than W -boson decay via virtual (off-shell) intermediate vector bosons. The decays can be 3-body, purely leptonic, involving a pair of opposite charge leptons and a neutrino, $N \rightarrow \ell_\alpha^+ \ell_\beta^- \bar{\nu}_\gamma$ or can be semi-leptonic (involving a charged lepton or a neutrino and one or several mesons in the final state), see Figure 4.2.

Phenomenology of heavy neutral leptons has been discussed since early 1980s [see e.g. 49, 50, 51, 52, 53]. The recent works that summarize the results are [54, 45, 46].

^{*}The branching ratio for the latter process is suppressed by the mixing angle $|\theta_{N\mu}|^2$ as compared to the $\text{Br}(K^+ \rightarrow \mu^+ + \nu_\mu)$.

[†]In this thesis we limit ourselves to $M_N < m_W$ and therefore do not discuss production/decay modes of heavier HNLs.

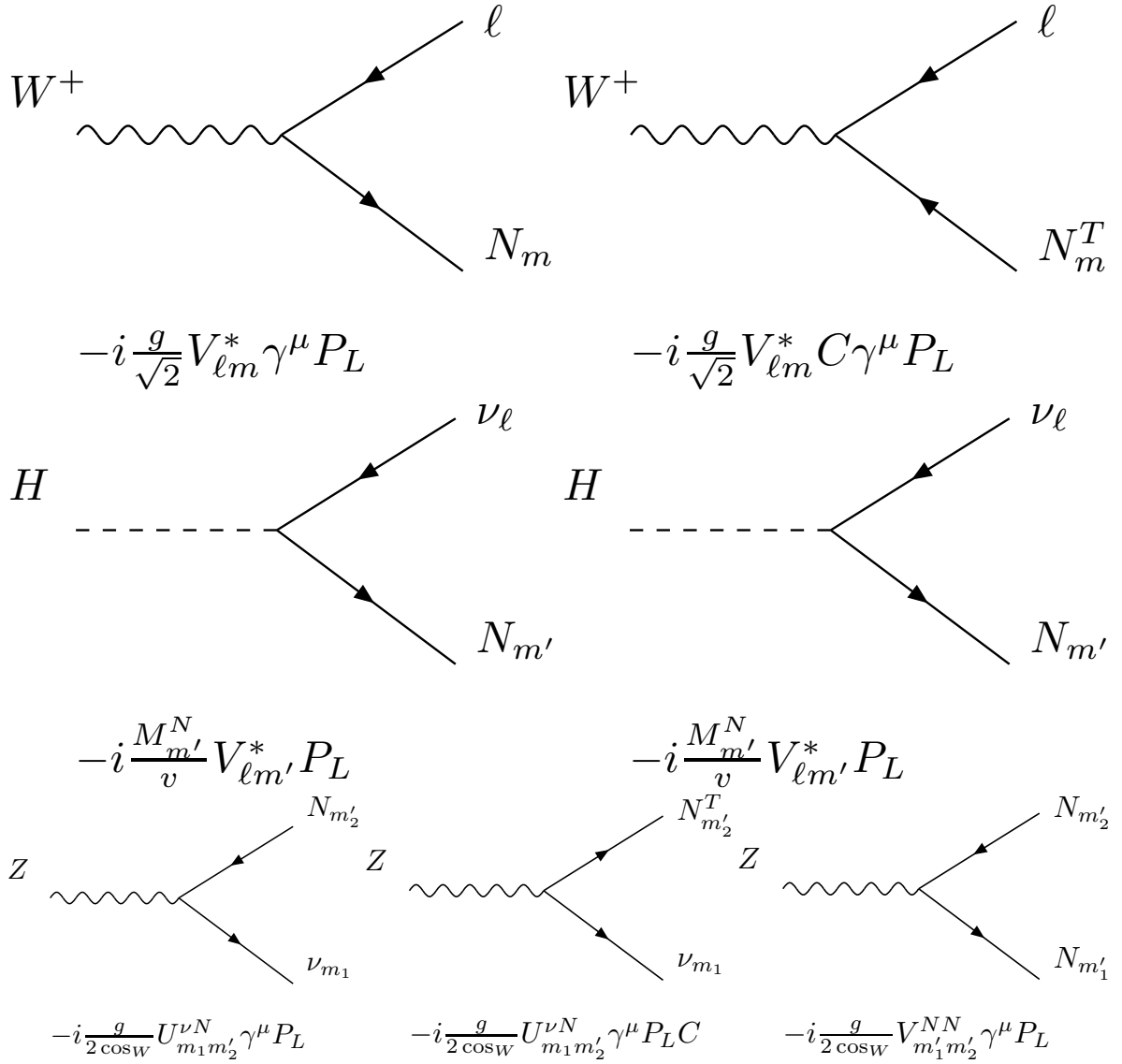
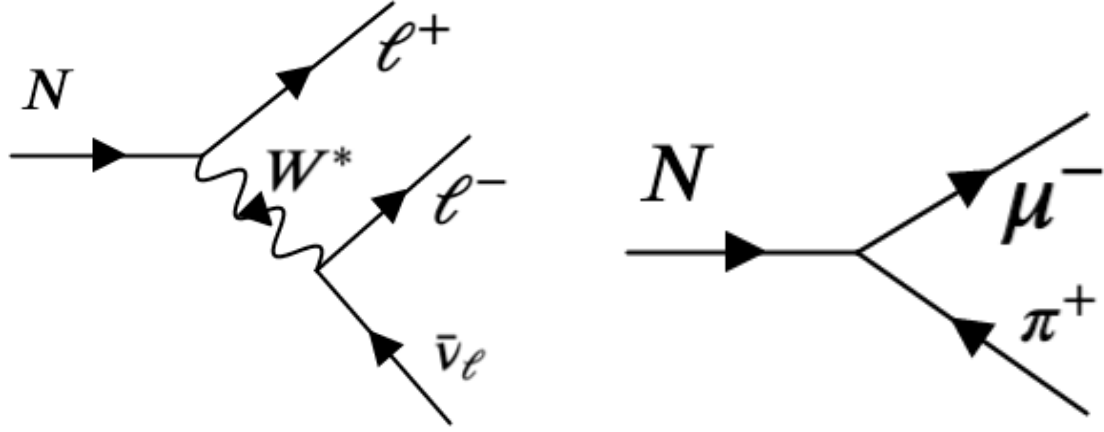


Figure 4.1.: Interaction vertices of heavy neutral leptons with W (top), Z (bottom) and Higgs bosons (middle). HNLs are denoted by N_m , massive states of SM neutrinos are denoted by ν_m , flavour neutrino states are ν_ℓ .

Two vertices for each type of interaction is due to Majorana nature of HNLs. The vertices involving only Standard model particles are not shown. The Feynman rules are present and the diagrams are taken from [45].

Many particle physics experiments have searched for HNL in the past, for the most up-to-date compilation of results see [55]. Major on-going experiments (such as ATLAS, CMS, LHCb, and NA62 in CERN, T2K and Belle in Japan) include HNL searches into their scientific programs [56, 57, 58, 59, 60, 61, 62, 63, 64, 65, 66, 67, 68, 69, 70, 71, 48, 72].



(a) Leptonic decay mode $N \rightarrow \ell^+ \ell^- \bar{\nu}_\ell$

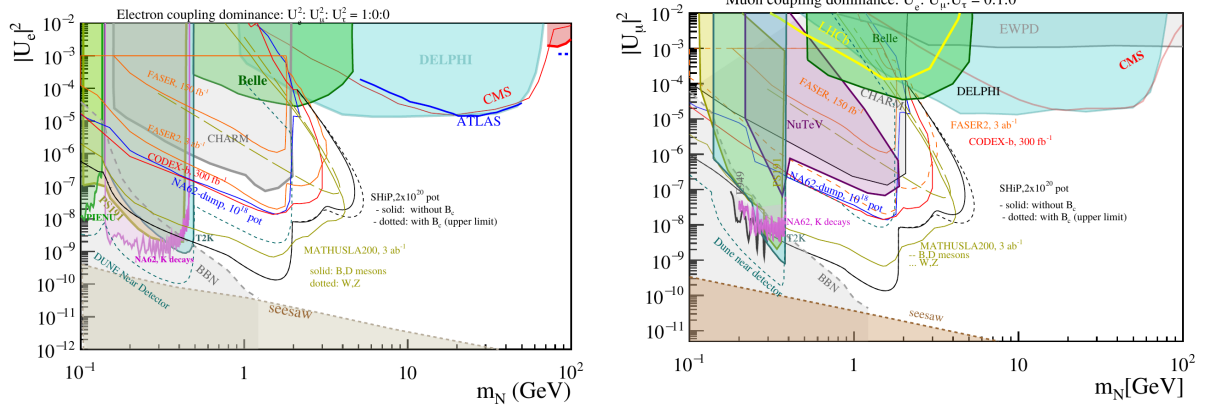
(b) Semi-leptonic decay mode, $N \rightarrow \mu^- \pi^+$.

Figure 4.2.: Typical decays of heavy neutral leptons mediated by charge current interactions (off-shell W -bosons). Left panel: leptonic decay into two opposite sign leptons ℓ^\pm and a neutrino. The leptons can be of the same or different flavours. Right panel: semi-leptonic decay of HNL to a muon and a pair of $u\bar{d}$ quarks, that hadronize into a single π^+ .

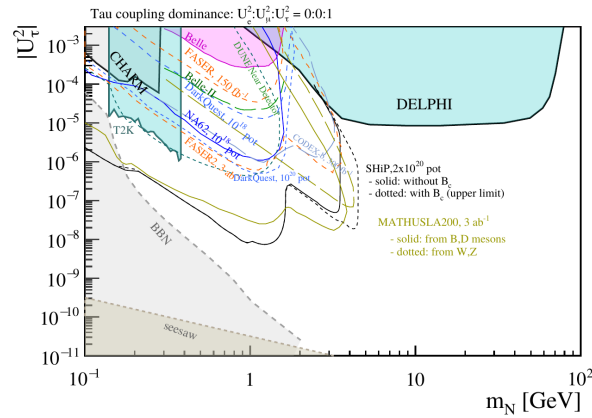
Figures 4.3a–4.3c summarize existing (shaded) and future (contour) limits on HNLs with $M_N \leq 100$ GeV. Each plot considers only HNLs mixed with one specific flavour – e, μ or τ .[‡]

Figure 4.3c demonstrates that the strictest bounds on HNLs coupled with τ neutrinos in the mass range $M_N \in [2 : 75]$ GeV are set by DELPHI – a LEP1 experiment – and is based on direct searches in Z boson decays $Z \rightarrow \nu N$ following by leptonic or semi-leptonic HNL decays [47]. Future searches with *e.g.* SHiP experiment [73] will improve the limits for HNL masses $M_N \leq m_B - m_\tau$ but do not affect larger masses. In particular, there are no LHC probes of $|\theta_{N\tau}|^2$ mixing. This is due to the fact that τ leptons are short-lived and are difficult to detect at ATLAS and/or CMS. This warrants the investigation of the current thesis – *can ATLAS experiment provide competitive bounds for HNLs mixing with τ for masse above few GeV?*

[‡]In realistic models, HNLs mix with *several* flavours at the same time (as dictated by neutrino oscillation data). In this case the bounds can be drastically different [42].



(a) Current bounds on HNL mixing with electron flavour (b) Current bounds on HNL mixing with muon flavour.



(c) Current bounds on HNL mixing with tau flavour.

Figure 4.3.: Current and future experimental bounds on HNL mixing angle U_α^2 as a function of the HNL mass for $M_N \leq 100$ GeV. The bounds are for the mixing with a single flavours, indicated on the y axis. Shaded regions are excluded from the past experiments. Contours are projected sensitivities of the future Intensity Frontier experiments. The lower brown shaded region denotes the region of HNL mixings that is too small to account for the observed neutrino masses (*i.e.* no seesaw mechanism is possible). The plots are taken from [41].

The LHC & ATLAS

5.1 Large Hadron Collider

The Large Hadron Collider (LHC) is the world's largest and most powerful particle collider experiment. It is operated by CERN and consists of the accelerator ring, which measures 27 km in circumference, and the 4 major detectors/experiments: ATLAS, ALICE, CMS and LHCb.

In any collider experiment there are two central parameters, determining the kind of physics it is able to explore. The first key parameter is the centre of mass energy. This determines what particles and processes are within the reach of the experiment. The second key parameter is the instantaneous luminosity, $\mathcal{L}(t)$, which determines the collision rate of the experiment [35]. This in turn can be used to calculate the number of events of a given type produced in the lifetime of the experiment:

$$N = \sigma \int \mathcal{L}(t) dt, \quad (5.1.1)$$

where σ is the cross section of the process in question. For brevity we will henceforth refer to the time-integrated luminosity simply as \mathcal{L} or 'luminosity'.

At the LHC protons are collided at centre of mass energies of up to $\sqrt{s} = 13$ TeV [74]. The integrated luminosity of the data collected after the Run 2 (2016–2018) reaches $\mathcal{L} = 139 \text{ fb}^{-1}$ for each of the ATLAS/CMS experiments with an uncertainty of 1.7% [75]. It is expected that in the future runs the integrated luminosity will reach $\mathcal{L} = 3000 \text{ fb}^{-1}$ [74].

5.2 The ATLAS Experiment

Throughout this thesis we will focus specifically on searching for HNLs using the ATLAS detector. An experiment such as ATLAS is well suited for HNL searches in the mass range $M_N \in [\text{few} : 75] \text{ GeV}$. A high-energy, high-intensity proton-proton collider experiment such as ATLAS produces copious amounts of especially W bosons, and is therefore extremely well suited for this kind of direct search. The production rates of

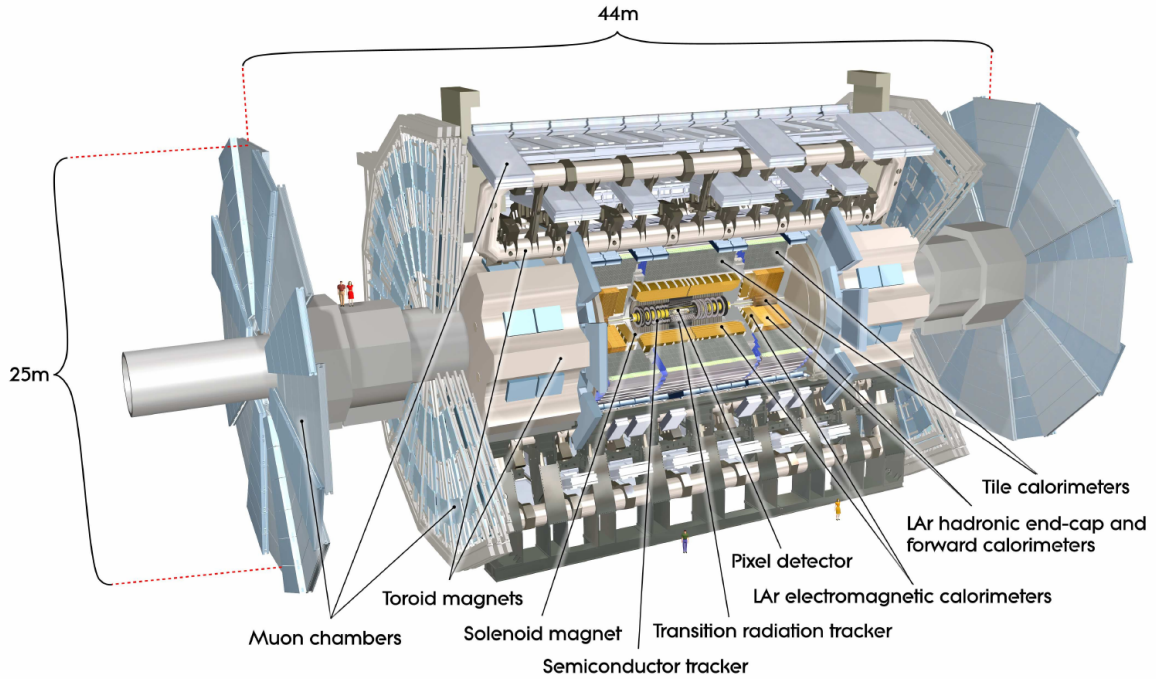


Figure 5.1.: A cut-away view of the ATLAS detector. From ref. [76].

both Z and Higgs bosons are too low to reach sensitivity in an area of the $M_N - |\theta_{N\tau}|^2$ parameter space which has not yet been excluded.

5.3 ATLAS detector Geometry - A Brief Interlude

Before moving on to discussions of detector specific triggers or detection requirements, a brief introduction to the geometry of the ATLAS detector, along with notation definitions which will be used from hereon out, are in order. The definitions in this section are a synthesis of those given in [35] (Ch. 10.9) and [78].

Fig. 5.3 shows a stylised version of the approximately cylindrical ATLAS detector, which is more realistically portrayed in Fig. 5.1. Conventionally a right-handed, Cartesian coordinate system is used as reference for the events happening within the detector. This constitutes the laboratory frame of reference, whose origin is placed at the centre of the detector coinciding with the interaction point between the opposing beams, with the z -axis following the beam line. The transverse plane is then spanned by the x - and y -axes.

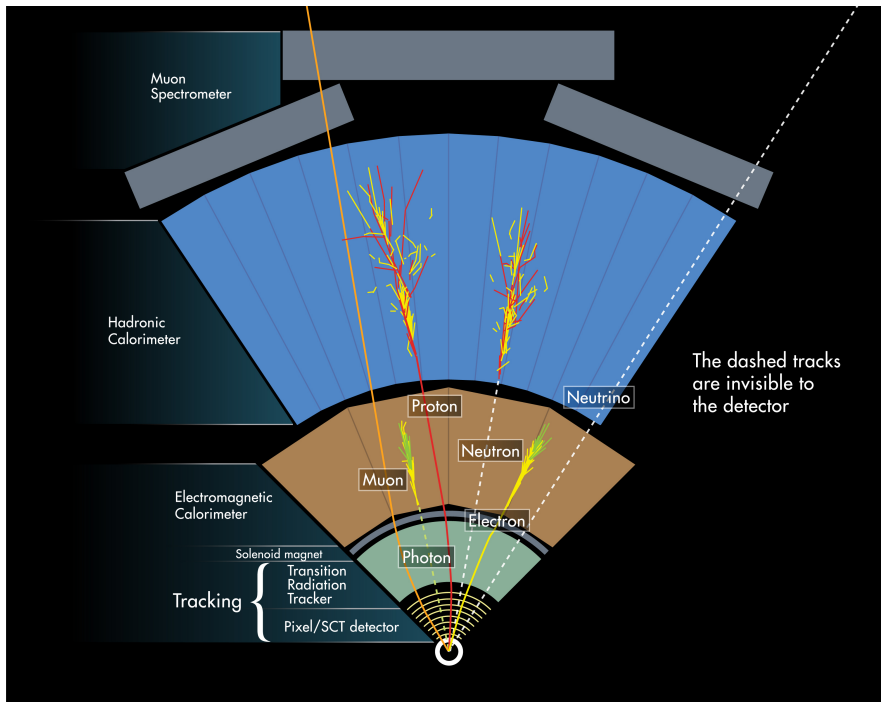


Figure 5.2.: The ATLAS detector viewed transversely, illustrating the individual detector layers. From innermost to outermost: Tracking, electromagnetic calorimeter, hadronic calorimeter and muon spectrometer [76]. Image from: [77]

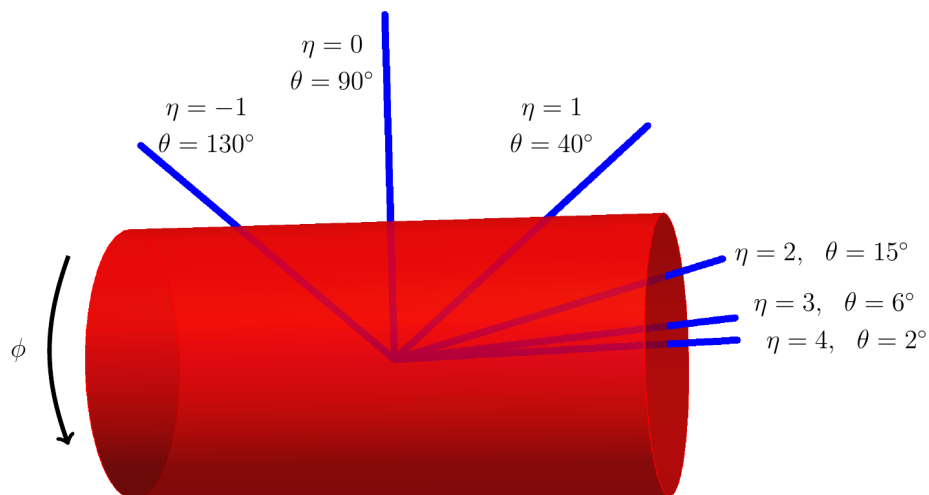


Figure 5.3.: A schematic illustration of the ATLAS detector geometry, stylised as a cylinder, with explicit measures of pseudorapidity. Figure from [78]. The z -axis is defined to follow the beam line, running through the centre of the cylinder from left to right. The numerical value of the pseudorapidity $|\eta|$ runs from 0 to ∞ , or π to 0 expressed as the polar angle θ . The azimuthal angle ϕ runs around the beam from 0 to 2π .

A very central kinematic quantity in collider physics using toroidal detectors, such as the ATLAS detector, is transverse momentum p_T . The amount of transverse momentum a given particle carries determines how much energy it will deposit in the calorimeters of the detector, and so it is an important factor in determining if the particle will be picked up as a signal in the detector. Transverse momentum is defined as:

$$p_T = \sqrt{p_x^2 + p_y^2} \quad (5.3.1)$$

Another important property of particles one might wish to detect, is that they are travelling in a direction which will allow them to interact with the detector and not simply let them escape detection by propagating in parallel to the beam line. To keep track of this pseudorapidity η is conventionally used instead of the (lab. frame) polar angle θ , since the difference between two pseudorapiditys is invariant under boosts along the beam axis - an important feature in hadron colliders. The pseudorapidity is given by:

$$\eta = -\ln \left[\tan \left(\frac{\theta}{2} \right) \right] = \tanh^{-1} \left(\frac{p_z}{|\vec{p}|} \right) \quad (5.3.2)$$

Here \vec{p} signifies the 3-momentum. Where it is needed the 4-momentum will simply be referred to as p . The azimuthal angle is fully within the transverse plane and is given by:

$$\phi = \tan^{-1} \left(\frac{p_x}{p_y} \right) \quad (5.3.3)$$

The angular separation ΔR between two particle momenta will also become a useful concept later in this thesis, and is defined as follows:

$$\Delta R = \sqrt{(\Delta\phi)^2 + (\Delta\eta)^2} \quad (5.3.4)$$

Having now established the most fundamental geometric quantities needed in this thesis, we can now move on to discussing the specifics of detecting HNLs in the ATLAS experiment.

5.4 Tau-triggers at ATLAS

When the ATLAS experiment is running the GHz rate of events occurring within the detector is far higher than the rate at which the experiment is able to record them. This necessitates the use of a selection system, which can prioritise the events of potential scientific importance and save these, in real time. This selection system is called ‘the

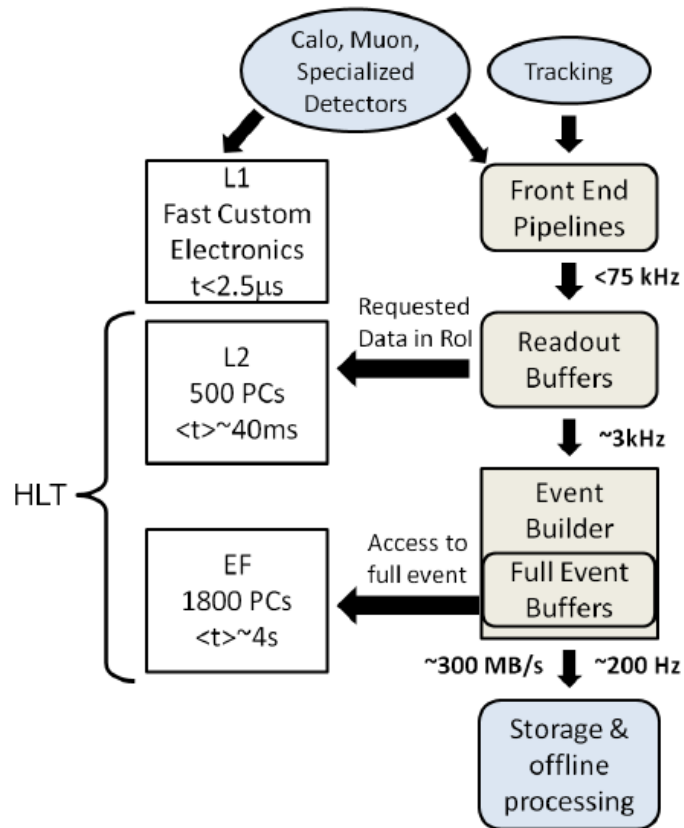


Figure 5.4.: A schematic of the ATLAS trigger system. The left column shows the L1 (‘level 1’, hardware-based) and HLT (high level trigger, software-based) trigger levels along with their response times and data rates. Figure from [80].

ATLAS Trigger and Data Acquisition System’ (TDAQ), see Figure 5.4. The set of triggers relevant to this thesis are the ATLAS $\tau\tau$ -triggers described in [79], which this section is based on. But first, a few words on triggers in general.

Triggers are essentially a set of detection criteria, comprised of tracking information, energy deposits (or lack there of) in the different calorimeters, timing information etc. and a set of sophisticated algorithms combining the information to classify/reconstruct individual particles and whole events. Schematically the TDAQ consists of a set of hardware-based triggers, L1, which accepts or rejects events initially, resulting in a rate of < 75 kHz accepted events. These are then passed through the software-based ‘high-level triggers’ (HLT), which further reduce the event acceptance rate to around 200 Hz, after which the accepted events are stored for analysis.

In order to search for new physics in a collider experiment, in the case of this thesis, searching for an HNL coupled to τ at ATLAS, it is important to know which triggers are suitable to the purpose. These will determine how to search and at what efficiency the experiment will be able to detect the desired signatures. During the search for the

Higgs boson at ATLAS a number of triggers were developed to match the expected signatures of Higgs interactions and decays, thus aiding the discovery of the Higgs. These triggers were developed further in the wake of the Higgs discovery to study its interactions with greater precision. The trigger requirements described in [79], summarised in Figure 5.7, were developed to trigger on hadronically decaying tau leptons, which provides the strongest signal of Higgs' coupling to charged leptons, $h \rightarrow \tau^+\tau^-$.

Detecting tau leptons in ATLAS requires a reconstruction from its decay products, as opposed to both electrons and muons which can be detected directly using information from the inner, electromagnetic tracker in combination with the electromagnetic calorimeters and muon calorimeters respectively. The need for such a reconstruction inherently makes the searches relying on detection of τ leptons more complicated, than those relying on e and μ leptons. Furthermore, when venturing into τ lepton reconstruction the energy/momentum of the resulting tau neutrino is carried out of the detector, undetected. This means overall less energetic (visible) decay products from which the τ lepton must be reconstructed, and with the reduction in energy/momentum, the rate of events which pass the trigger requirements decrease.

Since τ detection relies on reconstruction of its decay products, different trigger requirements would need to be considered for the different types of τ decays. τ leptons can decay either leptonically ($\tau \rightarrow \nu_\tau l \nu_l$, where $l = e, \mu$), which happens in $(35.21 \pm 0.06)\%$ of the time, or hadronically ($\tau \rightarrow \nu_\tau$ hadrons) in the remaining 64.79% of τ decays[81].

When studying HNLs coupled only to τ and are produced in W decays, as is the focus of this thesis, the process at leading order looks as the one depicted in Fig. 5.5. We will refer to the τ created in the same vertex as the HNL as the 'primary' charged lepton, the τ from the decay vertex of the HNL as the 'secondary' charged lepton, and finally, the lepton l_α originating from the (virtual) W as the 'tertiary' charged lepton. This type of process results in a tri-lepton signature (as discussed in Chap. 4). Since the triggers are able to distinguish electrical charge, in order to minimise SM background we will keep to considering only the lepton number violating processes (LNV) in which both τ leptons have the same charge. In addition to this we will only consider the cases in which the third lepton, l_α , has opposite charge to the τ leptons, and keep $\alpha = e, \mu$, i.e. a trilepton signature of the form: $\tau^\pm \tau^\pm l_\alpha^\mp$. The processes resulting in such signatures are listed in Table 5.1.

Since HNLs coupled to τ can be searched for by looking for a pair of hadronically decaying τ leptons, we want to explore if it is feasible to 'piggyback ride' the search for the Higgs boson, by using these $\tau\tau$ triggers. Since these triggers are designed

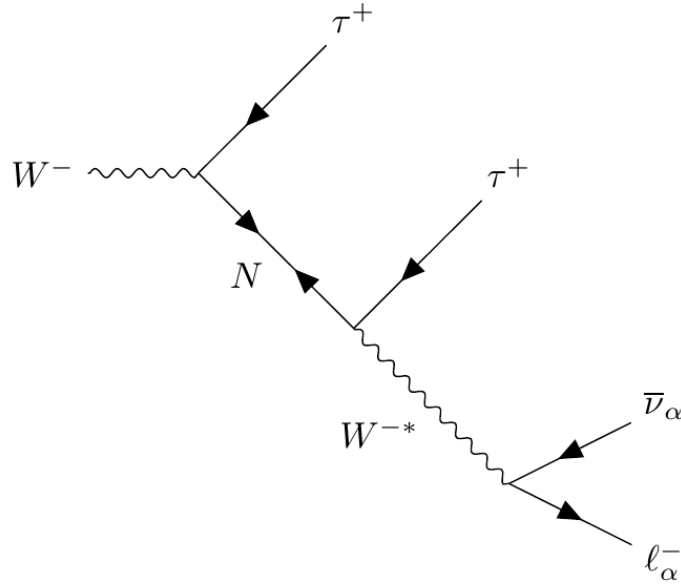


Figure 5.5.: Leading order Feynman diagram of a W decaying to a τ lepton and an HNL, and its subsequent decay into charged leptons, $W \rightarrow \tau^+ N, N \rightarrow \tau^+ l_\alpha \bar{\nu}_\alpha$. Throughout this thesis we will refer to the charged lepton originating directly from the W decay as the ‘primary’ lepton, the lepton originating from the decay vertex of the HNL as the ‘secondary’ lepton, and the final lepton l_α as the ‘tertiary’ lepton.

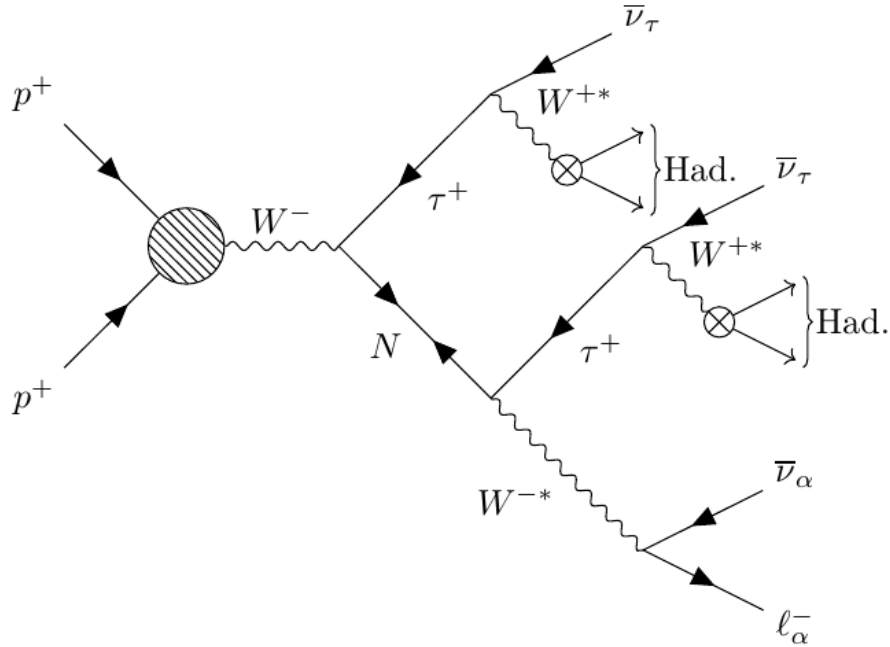


Figure 5.6.: Leading order Feynman diagram of the process $pp \rightarrow \tau^+ N, N \rightarrow \tau^+ l_\alpha \bar{\nu}_\alpha$, with both τ^+ subsequently decaying hadronically.

Process	ΔL	MadGraph Process string
$W^+ \rightarrow \tau^+(N \rightarrow \tau^+ e^- \bar{\nu}_e)$	-2	p p > ta+ n1, n1 > ta+ e- ve~
$W^- \rightarrow \tau^-(N \rightarrow \tau^- e^+ \nu_e)$	+2	p p > ta- n1, n1 > ta- e+ ve
$W^+ \rightarrow \tau^+(N \rightarrow \tau^+ \mu^- \bar{\nu}_\mu)$	-2	p p > ta+ n1, n1 > ta+ mu- vm~
$W^- \rightarrow \tau^-(N \rightarrow \tau^- \mu^+ \nu_\mu)$	+2	p p > ta- n1, n1 > ta- mu+ vm

Table 5.1.: The 4 possible tree-level HNL processes leading to signatures of the type $\tau^\pm \tau^\pm l_\alpha^\mp$, where $\alpha = e, \mu$. These are all lepton number violating (LNV) processes. Since the HNL in this thesis is assumed to only couple to τ , only LNV processes are possible, if charged leptons of the same flavour are required to have the same sign charge. The format of the table is inspired by[42]. Since all these processes rely on W^\pm boson decay, at the LHC there will be a slight asymmetry in cross sections between those processes with net positive and net negative charge, because of the net positive charge of the initial protons of $\mathcal{O}(40\%)$ [82], see also Chapter 7. Besides this charge asymmetry, it is reasonable to assume lepton universality[35] between the processes containing e and μ , since their masses are negligible at the energies considered, and are both identically zero in the HeavyN model[83] used for data generation here. with the above in mind, the focus for the remainder of this thesis will be on process 3: $W^+ \rightarrow \tau^+(N \rightarrow \tau^+ \mu^- \bar{\nu}_\mu)$.

for detecting hadronically decaying taus, this will be the focus of the thesis. The full process from proton proton collision to HNL production and subsequent decay is sketched in Fig. 5.6. The trigger requirements of the $\tau\tau$ triggers described in [79], are summarised in Fig. 5.7 in terms of the geometric quantities defined in Section 5.3.

Trigger	Typical offline selection	Trigger selection		Trigger rate at $1.2 \times 10^{34} \text{ cm}^{-2} \text{ s}^{-1}$	
		L1	HLT	L1 [kHz]	HLT [Hz]
τ	$p_T^\tau > 170 \text{ GeV}$	60	160	5.2	15
2τ	$p_T^\tau > 40, 30 \text{ GeV}, p_T^{\text{jet}} > 80 \text{ GeV}$	20i,12i,25	35,25,-	6.7	35
$\tau+e$	isolated e , $p_T^e > 18 \text{ GeV}$, $p_T^\tau > 30 \text{ GeV}, p_T^{\text{jet}} > 80 \text{ GeV}$	15i,12i,25	17i,25,-	3.4	9
$\tau+\mu$	isolated μ , $p_T^\mu > 15 \text{ GeV}$, $p_T^\tau > 30 \text{ GeV}, p_T^{\text{jet}} > 80 \text{ GeV}$	10,12i,25	14i,25,-	1.7	7
$\tau+E_T^{\text{miss}}$	$p_T^\tau > 40 \text{ GeV}, E_T^{\text{miss}} > 150 \text{ GeV}$, $p_T^{\text{jet}} > 70 \text{ GeV}$	20i,45,20	35,70,-	1.8	8
2τ with L1Topo	$p_T^\tau > 40, 30 \text{ GeV}, \Delta R(\tau, \tau) < 2.6$	20i,12i,2.9	35,25,-	5.9	39
	$p_T^\tau > 40, 30 \text{ GeV}, \Delta R(\tau, \tau) < 2.6$, $p_T^{\text{jet}} > 80 \text{ GeV}$	20i,12i,2.9,25	35,25,-,-	3.8	24

Figure 5.7.: List of $\tau\tau$ -triggers in ATLAS Run 2, from [79].

Data Generation

When we want to study the phenomenology of hypothetical laws of nature within particle physics, such as the theory of HNLs, a very handy set of tools is the collection of event generators, e.g. MadGraph [84], PYTHIA [85], SHERPA [86], etc. Here an ‘event’ should be understood as the hard scattering of two particles and their resulting decay products, or alternately a single particle decaying [87]. An event could for instance be a proton-proton collision, the resulting intermediate states and final state particles, those which could be observed given an idealised detector. Such event generators make the study of numerous hypotheses, detector sensitivities and detector performances much more accessible. Especially, when we wish to study a hypothesis like HNLs, in a context where analytical calculations are unfeasible, or even impossible – which is the case when considering the events taking place within the LHC, since these processes are very QCD heavy.

6.1 HeavyN Model

Heavy neutral leptons are described within the MadGraph via a special model, called HeavyN. The HeavyN FeynRules model[83] contains the Feynman rules of the HNL Lagrangian terms (see, e.g. [45]), and works as an add-on to event generators, extending the SM with (up to) three HNLs. For the purposes of this thesis, only one of these is set to have non-zero parameters. The HeavyN model is used in other studies of HNLs in connection to ATLAS, see for instance [42], and so it is the model we have chosen to work with as well.

6.2 Data Generation

The HNL searches at ATLAS are centred around searching for the trilepton signatures $e^\pm e^\pm \mu^\mp$ and $\mu^\pm \mu^\pm e^\mp$ as a result of HNL hypotheses where a single HNL couple to either e or μ [88].

The goal of this thesis is to make a qualified estimate as to whether ATLAS has any sensitivity beyond the Delphi limit, around $|\theta_\tau|^2 \approx 10^{-5}$ [41](see also Fig. 4.3c), to a

single HNL coupled only to τ , or if it is indeed as unfeasible as to warrant the lack of exploration seen in HNL searches from ATLAS[88] and CMS[89, 90], where only $|\theta_e|^2$ and $|\theta_\mu|^2$ are explored.

Specifically we focus on the reappropriation of ATLAS' $\tau\tau$ -triggers to searching for HNLs. The triggers are described in Sec. 5.4.

In order to arrive at a sensitivity estimate of the ATLAS detector to the HNL hypothesis of this thesis, we are reliant on Monte Carlo simulated data. This will allow us to know the hypothetical HNL production rate in pp-collisions, as well as the HNL decay widths as functions of the hypothesis parameters. MC generated data will also help us investigate the intricacies of the HNL event kinematics, and ultimately allow us to estimate how well these kinds of events would be able to survive the ATLAS triggers described in Sec. 5.4. Here follows an outline of the work done in order to obtain such MC generated data.

6.2.1 MadGraph & PYTHIA Setup

The event generator used for parton level data generation in this thesis is MadGraph5_aMC@NLO v3.1.0[91] together with the HeavyN model [92, 83], specifically the SM_HeavyN_Gen3Mass_NLO version of the model. In this version of the HeavyN model, the third generation of SM fermions, i.e. top and bottom quarks and τ lepton, have non-zero masses. The tau decays, particle showering and hadronization are handled by PYTHIA 8.3[87].

Rather than listing the full parameter and run cards here we will simply list the changes made to the default cards*:

Deviations from the default parameter card:

- Set m_{N2} and m_{N3} to zero, along with the corresponding mixing parameters, V_{eN2} , $V_{\mu N2}$, $V_{\tau N2}$ and V_{eN3} , $V_{\mu N3}$, $V_{\tau N3}$. The HeavyN model supports multiple HNLs, but In this thesis a model with only a single HNL is considered.
- Set m_{N1} to a selection of values within [5; 50] GeV.

*The full parameter and run cards can be found online. Cards for HNL event generation: *Parameter card* (<https://pastebin.com/7S3b4K06>) and *run card* (<https://pastebin.com/0rUR9HLk>). Cards for decay width calculation: *Parameter card* (<https://pastebin.com/Y6sTgAA3>) and *run card* (<https://pastebin.com/DL5zRkes>).

- Set $V_{\tau a N1}$ to 10^{-3} , a value large enough as to not cause trouble for the numerical integration, otherwise resulting in the cross section of the process being zero.
- Set the mixing parameters $V_{e N1}$ and $V_{\mu N1}$ to zero, since only the case in which the single HNL couples to tau is considered.

Deviations from the default run card:

- Set both the total energies of beam 1 and 2 to 6500 GeV, to reflect the most recent LHC run centre of mass energy $\sqrt{s} = 13$ TeV[74].
- Set the number of events to generate to 40.000.
- Remove all p_T cuts, both lower and upper.

This last adjustment of removing all p_T cuts is particularly important in the context of efficiency estimation. To accurately estimate the detector efficiency the data generated should be as close to the hypothesised physical reality (SM + HNL) as possible. Generating data with a predetermined lower p_T cut, would result in a larger fraction of generated events passing the p_T trigger requirements, and thus inflate the efficiency estimate relative to reality. And similarly the efficiency would be underestimated if upper bounds are placed on the generated particles' p_T .

With the above described setup the foundation for generating the data of interest to this thesis has been laid. The event structure to be generated should reflect the process shown in Fig. 5.6. The process is generated in MG following the commands shown in Fig 6.1.

6.2.2 The Data Structure

Before proceeding with the analysis of the generated data a few remarks on the structure of the generated data and how it has been processed are in order.

As we were beginning to generate data using MG and subsequently processing this data, we worked only at parton level, meaning no particle showering or hadronisation was taken into account. The structure of each generated event was very similar to that shown in Fig. 6.2, with a simpler particle status convention and including the particle 4-momenta, stored in the file format 'LHE'. The structure of the generated parton level event almost one-to-one reflect the tree-level Feynman diagram in Fig. 5.6. Approaching the data generation at parton level, however neat the event structure

```

1  import model SM_HeavyN_Gen3Mass_NLO
2  generate p p > ta+ n1, n1 > ta+ mu- vm~ @ 0
3  add process p p > ta+ n1 j, n1 > ta+ mu- vm~ @ 1
4  add process p p > ta+ n1 j j, n1 > ta+ mu- vm~ @ 2
5  output lnv_ta+ta+mu-_Gen3Mass_2jets_PYTHIA_40000evt_scan
6  launch lnv_ta+ta+mu-_Gen3Mass_2jets_PYTHIA_40000evt_scan
7  shower=PYTHIA8
8  done
9  Cards/default_run_card_nocuts.dat
10 Cards/default_param_card_hnl_HeavyN_Gen3Mass_NLO.dat
11 set VtaN1 1e-3
12 set mN1 scan:[5.0,10.0,20.0,30.0,40.0,50.0]
13 done

```

Figure 6.1.: An example of the commands passed to MG to generate the process $pp \rightarrow \tau^+ N \rightarrow \tau^+ \tau^+ \mu^-$, with up to 2 hard jets, letting PYTHIA8 handle the tau decays and showering. The procedure for generating data samples with 0 (up to 1) jet(s) is the same as the above, except omitting line(s) 3 (and 4).

made the data processing, proved incomplete in significant ways. Firstly, MG alone with the imported HeavyN model proved ill equipped to handle tau decays[†].

Furthermore, the absence of particle showering meant that the Ws produced on-shell, in the absence of any jets, would have no transverse momentum component whatsoever. This in turn means that the particles we are interested in observing, would not be able to acquire the transverse momentum required to pass the trigger conditions listed in Fig. 5.7.

These issues necessitated the inclusion of PYTHIA to handle tau decays, particle showering and hadronisation. This meant transitioning from LHE file format to ‘HEPMC’ files. Where LHE files have a simple and deterministic event structure, making the processing of the files relatively accessible, the HEPMC files are many times larger, and thus much more time consuming to generate, and each event is represented by thousands of lines of particle interactions which complicates the data processing significantly[‡]. One need to know the structure of the process generated to (manually) navigate the data files, extracting information about the relevant particles,

[†]When the HeavyN model was left to handle the tau decays at parton level, this resulted in a strange ‘boosting’ of the momentum of the decay products. We discussed the issue with Ruiz, who is behind the HeavyN model. This led to the correction of some model specific parameters, and we were informed that the model was not intended to handle tau decay, and that we should use e.g. PYTHIA for this purpose.

[‡]The HEPMC files are compressed files – 40,000 events in a compressed HEPMC file takes up roughly 3 GB, 10 GB if it is not compressed. A special thanks is here owed to Jean-Loup Tastet for

```

2716 ----- PYTHIA Event Listing (hard process) -----
2717
2718      no      id  name      status  mothers  daughters  colours
2719      0       90 (system)   -11     0     0     0     0     0     0
2720      1      2212 (p+)      -12     0     0     3     0     0     0
2721      2      2212 (p+)      -12     0     0     4     0     0     0
2722      3       -1 (dbar)   -21     1     0     5     0     0    501
2723      4        2 (u)      -21     2     0     5     0    501     0
2724      5        24 (W+)     -22     3     4     6     7     0     0
2725      6  9900012 (nu_Re)  -22     5     0     8    10     0     0
2726      7      -15 tau+     23     5     0     0     0     0     0
2727      8      -15 tau+     23     6     0     0     0     0     0
2728      9       13 mu-     23     6     0     0     0     0     0
2729     10      -14 nu_mubar  23     6     0     0     0     0     0
2730                                Charge sum: 1.000      Momentum sum:
2731
2732 ----- End PYTHIA Event Listing -----

```

Figure 6.2.: An excerpt from a PYTHIA log showing the ‘hard’ process, i.e. the overall structure of the process generated, corresponding to the Feynman diagram in Fig. 5.6. This exemplifies the system of particle IDs common to both MG and PYTHIA, along with the structure of mother and daughter particles, used to keep track of each particle’s generation and decay.

i.e. those involved in the hard process listed in Fig. 6.2, and these are identified using a standardised Monte Carlo numbering scheme [93]. This ‘manual’ approach to extracting information from HEPMC files makes it unfeasible to explicitly analyse the information pertaining to the hadronic decay products of the tau leptons, as well as the particles involved in jets that might be present in some events. This shall become relevant a little later on, but for now, let us take a look at the generated data.

providing a script to read the compressed HEPMC files line-by-line, thus avoiding having to decompress the data files.

Checks & Validations

7.1 A Couple of ‘Sanity’ Checks

After generating the desired data, and before proceeding with the main analysis in Chapter 8 we make a few ‘sanity checks’ and validations.

The first such check is reconstructing the invariant mass of each of two of decaying particles in the process pictured in Fig. 5.6: W and N . This is a way of checking that the data we have generated actually corresponds to the intended process, as well as to check that the scripts for reading and analysing the data are able to locate the right particles in the HEPMC files. The distributions of reconstructed invariant masses are shown in Fig. 7.1 and 7.2.

To ensure compliance between the HeavyN model and the SM implemented in MadGraph, we conducted a check examining the ratio of W^+ to W^- production within the SM, and checking that it translates into the ratio between the W^\pm -mediated processes $pp > \tau^\pm N$, and thus indicating a correct coupling of of MG and the HeavyN model. See Fig. 7.3.

7.2 Validation of HNL Decay Width

Reliably knowing the decay width of the HNL in the theoretical framework considered, is essential for all the following efficiency and sensitivity estimates. This is the case since both rescaling of the MG generated cross sections and the probability of the HNL decaying promptly, displaced or outside the detector all depend heavily on the HNL decay width.

The HNL decay width will scale with the mixing angle: $\Gamma_N \propto |\theta|^2$ [42], detailed in see Sec. 8.4. However, the decay width is also heavily, and non-trivially, dependent on M_N , as this determines what decay channels are kinematically allowed. Since we are here considering HNLs in a mass range from 5 GeV up to 50 GeV, we will be relying on HNL decay width values obtained through a combination of analytical approximations and

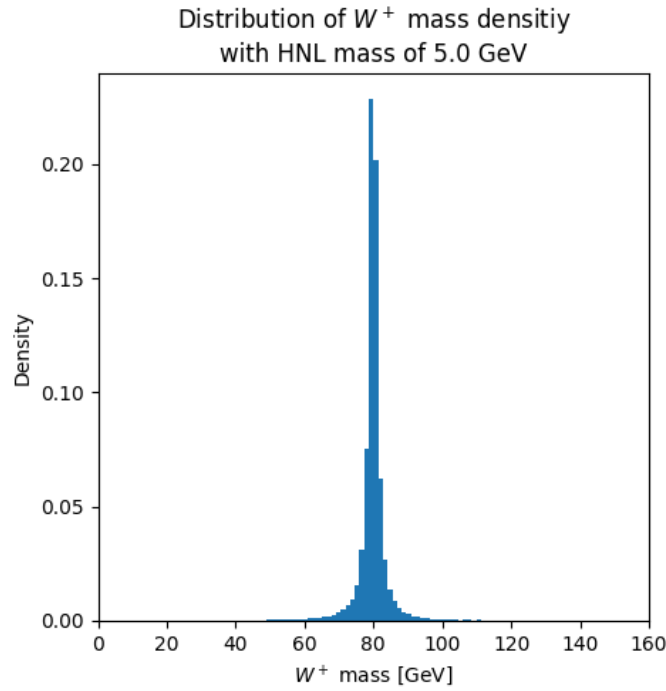
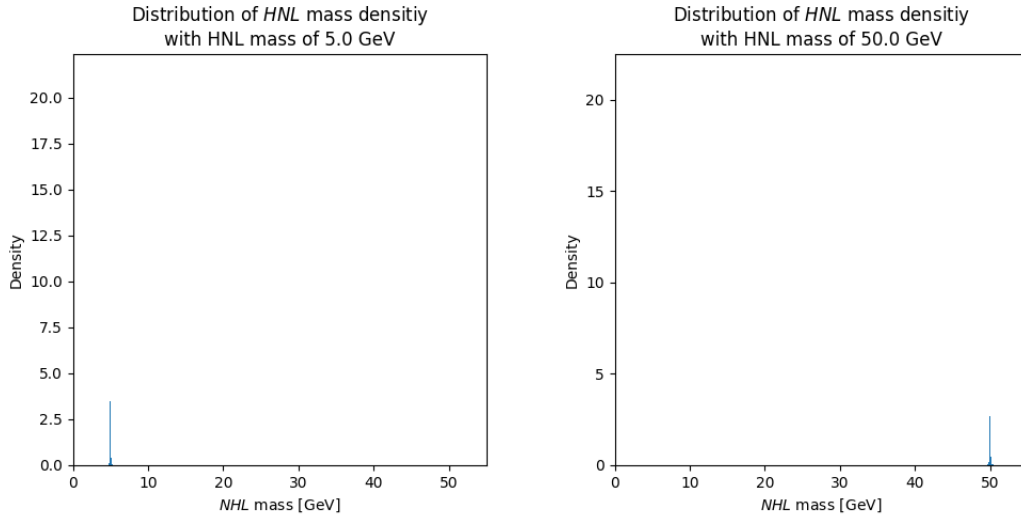


Figure 7.1.: Reconstructed invariant mass of the on-shell W .



(a) Reconstructed invariant mass of the HNL for $M_N = 5$ GeV. **(b)** Reconstructed invariant mass of the HNL for $M_N = 50$ GeV.

Figure 7.2.: Reconstructed invariant mass of the HNL for $M_N = 5, 50$ GeV. The widths of these mass distributions are extremely narrow compared to that of the M_W distribution. This fits with what we would expect to see, given the $\Gamma_W = (2.085 \pm 0.042)$ GeV [81], as opposed to the reference decay width of the HNL used in data generation of $\mathcal{O}(\Gamma_{N,\text{ref}}) \approx 10^{-3}$ GeV.

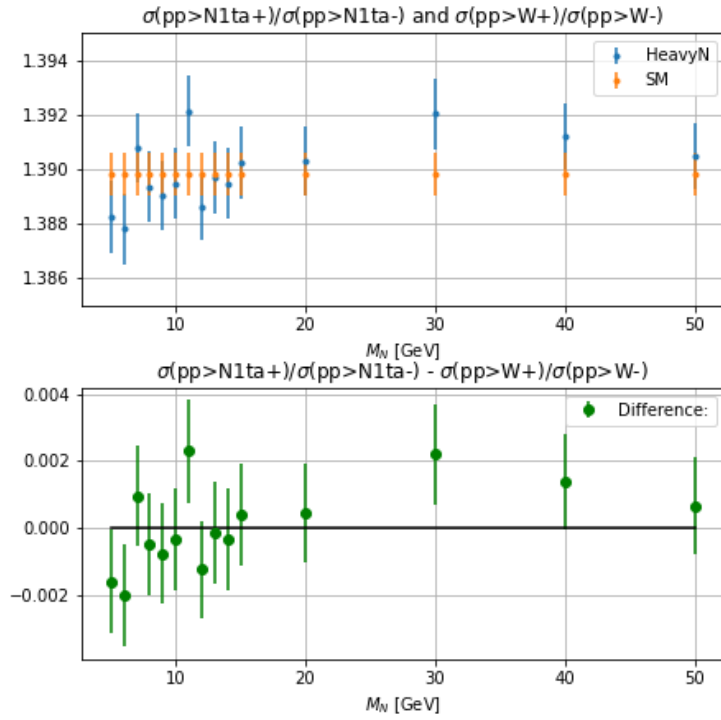


Figure 7.3.: The ratios of $\frac{\sigma(pp \rightarrow N\tau^+)}{\sigma(pp \rightarrow N\tau^-)}$, as generated in MadGraph using the HeavyN model, and $\frac{\sigma(pp \rightarrow W^+)}{\sigma(pp \rightarrow W^-)}$, using only the SM, are shown in the top panel. Since the processes $\sigma(pp \rightarrow N\tau^\pm)$ are mediated by W^\pm , the ratio of $N\tau^\pm$ production rates should be the same as for W^\pm . The bottom panel shows the difference between the two ratios. Within the errors, which are propagated from the errors reported by MadGraph, the ratios can be concluded to be in agreement.

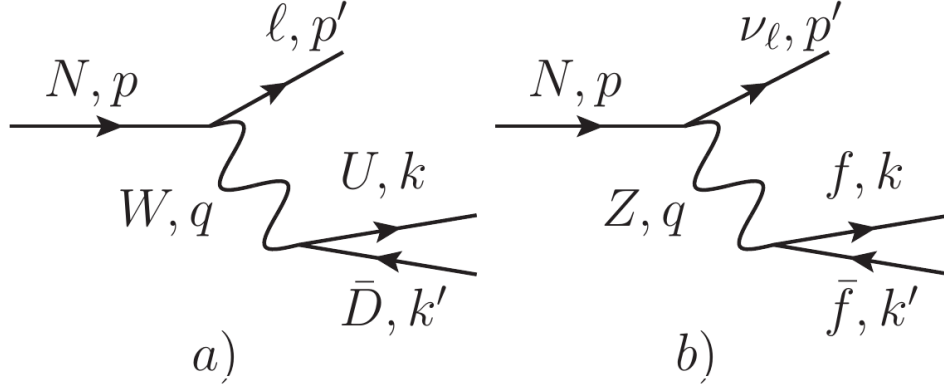


Figure 7.4.: Examples of HNL decay channels: a) charged current-mediated decay and b) Neutral current-mediated decay. Figure from [94].

MC simulations, each according to their strength. The analytical approximation will also serve as validation of the MC generated decay widths*.

Since the HNL has ‘inherited’ the interaction types of the SM model neutrino, as described in Sec. 3, its decay channels can be categorised as either charged or neutral current mediated, see Fig. 7.4. To obtain the full decay width the contributions from each decay channel is summed over[35]:

$$\Gamma_N = \sum_j \Gamma_j \quad (7.2.1)$$

The following decay width calculations are based on [94] Sec. 3.1.1, 3.1.2 and 3.2.2, considering tree-level HNL decay, calculated as Fermi interactions, incorporating an estimated QCD correction, which is here implemented for $M_N \leq 10$ GeV. The decay width estimates are done for one charge configuration, but due to the Majorana nature of the HNL considered here, an additional factor of 2 is applied to each partial decay width during calculation (not shown in the subsequent equations), since the charge conjugated processes also contribute.

7.2.1 Charged Current

The charged current mediated decay channels take the forms: $N \rightarrow l_\alpha^- \nu_\beta l_\beta^+$, where $\alpha \neq \beta$, and $N \rightarrow l_\alpha^- U_i \bar{D}_j$, exemplified in Fig. 7.4a. Here U_i is an up-type quark, $i = u, c$ and \bar{D}_j a down-type quark, $j = d, s, b$, having omitted the top quark, since it is kinematically disallowed in HNL decay within the considered range of M_N . The

*The decay widths obtained through MadGraph simulations are very sensitive to simulation initialisation - in this case especially the run-card options, and so a validation or cross-check is critical.

$\alpha = \tau$	Hadronic	Leptonic
CC	$\tau^- u \bar{d}$, $\tau^- c \bar{d}$ $\tau^- u \bar{s}$, $\tau^- c \bar{s}$ $\tau^- u \bar{b}^\dagger$, $\tau^- c \bar{b}^\ddagger$	$\tau^- e^+ \nu_e$ $\tau^- \mu^+ \nu_\mu$
NC	$\nu_\tau u \bar{u}$, $\nu_\tau d \bar{d}$ $\nu_\tau c \bar{c}$, $\nu_\tau s \bar{s}$ $\nu_\tau b \bar{b}^*$	$\nu_\tau e^+ e^-$, $\nu_\tau \nu_e \bar{\nu}_e$ $\nu_\tau \mu^+ \mu^-$, $\nu_\tau \nu_\mu \bar{\nu}_\mu$ $\nu_\tau \nu_\tau \bar{\nu}_\tau$
CC+NC	-	$\nu_\tau \tau^+ \tau^-$

Table 7.1.: All the kinematically allowed tree-level HNL decay channels, sorted into leptonic and hadronic and sorted by current mediation type. † is kinematically inaccessible for $M_N \leq 5$ GeV, ‡ for $M_N \leq 5$ GeV and * for $M_N \leq 8$ GeV.

hadronic decay channels here have also been estimated by those to individual quarks. This is modified to include some QDC corrections, see Sec. 7.2.3. See Table 7.1 for an overview of the kinematically allowed tree-level HNL decay channels.

The charged current mediated contribution to the HNL decay width is given by:

$$\Gamma(N \rightarrow l_\alpha^- U_i \bar{D}_j) = N_W \frac{G_F^2 M_N^5 |\theta_\alpha|^2}{192\pi^3} I(x_u, x_d, x_l) \quad (7.2.2)$$

where $x_l = \frac{m_{l_\alpha}}{M_N}$, $\frac{m_{U_i}}{M_N}$, $\frac{m_{\bar{D}_j}}{M_N}$ and $N_W = N_c |V_{ij}|^2$. Here $N_c = 3$ is the number of colours and V_{ij} is the CKM matrix element corresponding to the final state quarks U_i and \bar{D}_j . And finally the function $I(x_u, x_d, x_l)$, which is a result of the non-negligible masses of the final state particles. It is given by:

$$I(x_u, x_d, x_l) \equiv 12 \int_{(x_d+x_l)^2}^{(1-x_u)^2} \frac{dx}{x} (x - x_l^2 - x_d^2)(1 + x_u^2 - x) \sqrt{\lambda(x, x_l^2, x_d^2) \lambda(1, x, x_u^2)} \quad (7.2.3)$$

where $\lambda(a, b, c) = a^2 + b^2 + c^2 - 2ab - 2ac - 2bc$. The integral in Eq. (7.2.3) is solved numerically for each of the contributing decay channels. Eq. (7.2.2) is the same for the charged current-mediated process $N \rightarrow l_\alpha^- \nu_\beta l_\beta^+$, $\alpha \neq \beta$, when setting $N_W = 1$.

7.2.2 Neutral Current & Neutral-Charged Current Interference

The HNL decay channels illustrated in Fig. 7.4b are purely neutral current-mediated, for $f \neq \alpha$, however for $f = \alpha$ charged current interference terms must be considered.

f	C_1^f	C_2^f
u, c	$\frac{1}{4} \left(1 - \frac{8}{3} \sin^2(\theta_W) + \frac{32}{9} \sin^4(\theta_W) \right)$	$\frac{1}{3} \sin^2(\theta_W) \left(\frac{4}{3} \sin^2(\theta_W) - 1 \right)$
d, s, b	$\frac{1}{4} \left(1 - \frac{4}{3} \sin^2(\theta_W) + \frac{8}{9} \sin^4(\theta_W) \right)$	$\frac{1}{6} \sin^2(\theta_W) \left(\frac{2}{3} \sin^2(\theta_W) - 1 \right)$
$l_\beta, \beta \neq \alpha$	$\frac{1}{4} \left(1 - 4 \sin^2(\theta_W) + 4 \sin^4(\theta_W) \right)$	$\frac{1}{2} \sin^2(\theta_W) \left(2 \sin^2(\theta_W) - 1 \right)$
$l_\beta, \beta = \alpha$	$\frac{1}{4} \left(1 + 4 \sin^2(\theta_W) + 4 \sin^4(\theta_W) \right)$	$\frac{1}{2} \sin^2(\theta_W) \left(2 \sin^2(\theta_W) + 1 \right)$

Table 7.2.: Definitions of C_1^f and C_2^f in Eq. (7.2.4) from [94].

For all the final states where f is either quarks or charged leptons, the decay width contribution is:

$$\Gamma(N \rightarrow \nu_\alpha f \bar{f}) = N_Z \frac{G_F^2 M_N^5 |\theta_\alpha|^2}{192\pi^3} \times \left[C_1^f \left((1.14x^2 - 2x^4 - 12x^6) \sqrt{1-4x^2} + 12x^4(x^4 - 1)L(x) \right) + 4C_2^f \left(x^2(2 + 10x^2 - 12x^4) \sqrt{1-4x^2} + 6x^4(1 - 2x^2 + 2x^4)L(x) \right) \right], \quad (7.2.4)$$

where $x = \frac{m_f}{M_N}$, $L(x) = \log \left[\frac{1-3x^2-(1-x^2)\sqrt{1-4x^2}}{x^2(1+\sqrt{1-4x^2})} \right]$, $N_Z = 1$ for final state leptons or $N_Z = N_c$ for quarks and C_1^f and C_2^f are given by Table 7.2. Eq. (7.2.4) also holds for the case where $\alpha = \beta$, since the charged current interference is accounted for in C_1^f and C_2^f .

For final states consisting only of neutrinos, the decay width contribution is given by:

$$\Gamma(N \rightarrow \nu_\alpha \nu_\beta \bar{\nu}_\beta) = (1 + \delta_{\alpha\beta}) \frac{G_F^2 M_N^5 |\theta_\alpha|^2}{768\pi^3} \quad (7.2.5)$$

7.2.3 QCD Corrections

The partial decay width calculations outlined in Sec. 7.2.1 & 7.2.2 are calculated assuming only contributions from individual quarks. This is of course an assumption with limitations. As M_N approaches (but is still kept well above) the QCD mass scale, $\Lambda_{\text{QCD}} \approx 200 \text{ MeV}$ [95], QCD corrections will affect the decay width significantly. For $M_N > 2m_\pi$ multi-hadron final states becomes accessible. The effect of this can be approximated by the ratio of the partial decay width of τ leptons into hadrons and the

partial (tree-level) decay width of τ into single meson final states. The higher order corrections, Δ_{QCD} , are given by:

$$1 + \Delta_{\text{QCD}} \equiv \frac{\Gamma(\tau \rightarrow \nu_\tau + \text{hadrons})}{\Gamma_{\text{tree}}(\tau \rightarrow \nu_\tau \bar{u}q)} \quad (7.2.6)$$

$$\Delta_{\text{QCD}} = \frac{\alpha_s}{\pi} + 5.2 \frac{\alpha_s^2}{\pi^2} + 26.4 \frac{\alpha_s^3}{\pi^3} \quad (7.2.7)$$

Δ_{QCD} is modified for HNL corrections by taking the strong coupling as a function of the HNL mass, $\alpha_s(M_N)$, and evaluating Eq. (7.2.7). A factor of $1 + \Delta_{\text{QCD}}$ is then multiplied to the partial HNL decay widths with hadronic final states in Eq. (7.2.2) & (7.2.4). This is done for $M_N \leq 10$ GeV.

7.2.4 Analytical Estimate vs. MadGraph

The HNL decay widths have, besides the analytical estimates above, been calculated using MadGraph. This is done by following the method outlined in [42]: The HNL decay widths are simplified by the fact that $\theta_e = \theta_\mu = 0$ in the model considered here, and so the full HNL decay width reduces to the partial width from HNL- τ coupling[†]:

$$\Gamma_N(M_N, \theta_e, \theta_\mu, \theta_\tau) = \sum_{\beta=e,\mu,\tau} |\theta_\beta|^2 \times \hat{\Gamma}_\beta(M_N) = |\theta_\tau|^2 \times \hat{\Gamma}_\tau(M_N) \quad (7.2.8)$$

The decay width $\hat{\Gamma}_\tau(M_N)$ is computed in MadGraph for a number of M_N values between 5 and 50 GeV, by generating the process `n1 > all all all` with the mixing angle $\theta_\tau = 1$ and subsequently rescaling with $|\theta_\tau|^2$.

A comparison of the analytically estimated decay widths and the MadGraph generated decay width are shown in Fig. 7.5. The errors on the analytical approximation stemming from SM particle masses have been neglected, due to the complication of propagating them correctly, combined with the errors simply being extremely small. The only error considered on the analytical estimate is therefore the $\approx 10\%$ error on the QCD correction Δ_{QCD} as estimated by [94]. For the MadGraph generated decay widths the error is taken as the error reported by MadGraph. The decay widths seem to agree rather well until around $M_N = 40$ GeV, where the two start to visibly differ. The ratio between the MG generated and Fermi approximated HNL decay widths is also shown in Fig. 7.5, which make the differences much more visible. Here the trend of difference as M_N grows becomes much more obvious. This difference is to be expected, as when the M_N increases the assumption which the Fermi approximation is built around, namely $M_N \ll M_W, M_Z$, no longer holds. As a result, for $M_N > 10$ GeV we

[†]See Sec. 8.4 for more details on rescaling of decay widths and cross sections from MadGraph data.

will rely on the MG generated decay widths, since the finite mass of W and Z is here taken into account.

At the opposite end of the considered mass range the simulated and analytically approximated decay widths also differ increasingly as M_N decreases. This however is due to QCD effects. When generating HNL decay widths in MadGraph, as outlined above, this is done only at parton level, meaning no hadronisation is accounted for, only decays into bare quarks. Since such corrections are taken into account in the analytical estimate, up to $\mathcal{O}(\alpha_s^3)$, as outlined in Eq. (7.2.7), we will rely on these decay widths for $M_N \leq 10$ GeV. The sharp ‘jump’ in the ratio between 10 GeV and 11 GeV is due to neglecting Δ_{QCD} above 10 GeV. The value of the decay width ratio at $M_N = 10$ GeV is $0.9985 \pm 7 \cdot 10^{-4}$, and so the agreement between simulation and Fermi approximation is $< 1\%$, at this point between the QCD-dominated lighter masses and the larger masses where the Fermi approximation breaks down.

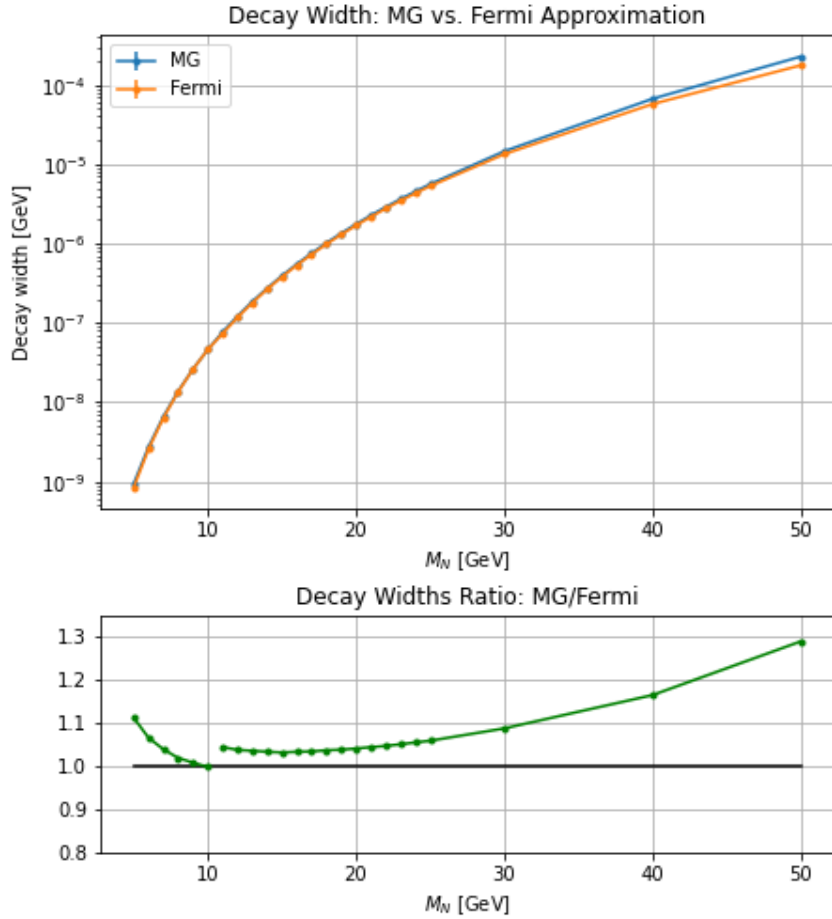


Figure 7.5.: *Top panel:* Decay widths of an HNL, coupled only to τ , as a function of mass. The orange graph is the analytical Fermi approximation, as outlined in Sec. 7.2.1, 7.2.2 and 7.2.3. The blue graph shows the MadGraph simulated HNL decay width. *Bottom panel:* The ratio between the MG generated and Fermi approximated HNL decay widths (green). The value of the decay width ratio at $M_N = 10$ GeV is $0.9985 \pm 7 \cdot 10^{-4}$, and so the agreement between simulation and Fermi approximation is $< 1\%$, at this point between the QCD-dominated lighter masses and the larger masses where the Fermi approximation breaks down.

Data Analysis

This chapter is the ‘heart’ of the thesis - processing the Monte Carlo simulated data, making sense of it and relating it to the real world. The ultimate goal of this process is to quantify the expected sensitivity of the ATLAS experiment to event signatures of an HNL coupled to τ . Before reaching this final sensitivity estimate, there are a couple of bridges to cross. Central to estimating the sensitivity of the ATLAS experiment to the tri-lepton signature $\tau^\pm\tau^\pm l_\alpha^\mp$, is the question: ‘How many events with this signature do we expect to observe, assuming the theory is true?’. This question can be answered using the conceptually straightforward equation[96]:

$$N_{\text{events}} = \underbrace{N_{\text{production, M}}}_{\mathcal{L}_{\text{int.}} \times \sigma_M} \times \text{BR}_{M \rightarrow X} \times P_{\text{decay, X}} \times \epsilon_{\text{detector}} \quad (8.0.1)$$

Eq. (8.0.1) gives the number of events, N_{events} , involving the particle X from the mother particle M . Concretely in this thesis M corresponds to W , and X to N . Also, a few more terms are added to account for the HNL decaying to τ/ν_τ , and for the τ leptons to decay hadronically. This is all specified in Sec. 8.2, in which we will address the last term of Eq. (8.0.1) - The efficiency of the ATLAS detector.

8.1 Event Kinematics

Getting to the detector efficiencies requires applying relevant trigger conditions. But before jumping into that, let us take a look at the event kinematics these rely on.

As mentioned in Sec. 6.2.2 the transverse momentum of the on-shell W boson in the type of process generated, and which is shown in Fig. 5.6, is very important to ensure its final decay products might pass the trigger requirements. The distributions of transverse momenta for the on-shell W bosons are shown in Fig. 8.1. The distributions all peak close to $p_T = 0$, and had these been generated at parton level only, without any particle showering in PYTHIA, the distribution from the data set without any jets would be identical zero. Any transverse momentum components the W s have acquired stem from initial state, soft or hard, radiation from the partons scattering to create the W , or electromagnetic radiation from the W itself. It is also seen that the more hard

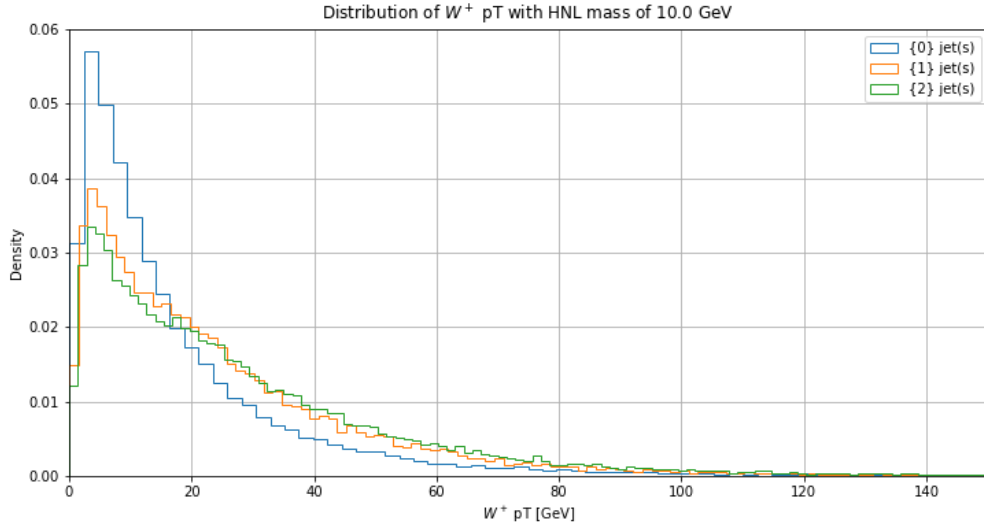


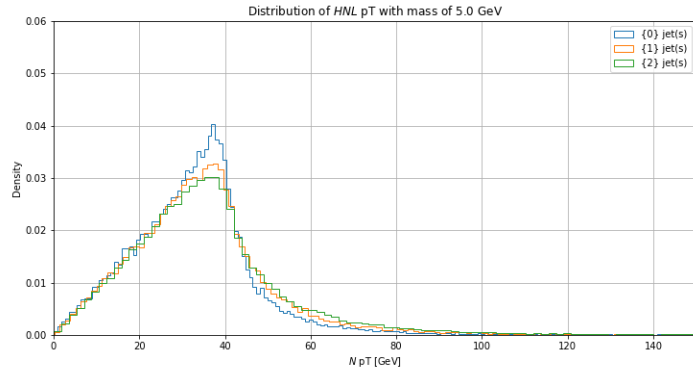
Figure 8.1.: Normalised distributions of W p_T , for up to 0, 1 and 2 jets. This demonstrates an upwards shift in p_T when jets are included in the data generation. These are from the data sets where $M_N = 10$ GeV, however the transverse momentum distributions of the W do not change when adjusting M_N .

jets are allowed in a process the more the W p_T distribution is shifted upwards. The biggest shift being between the case with no jets and the cases with allowing for jets.

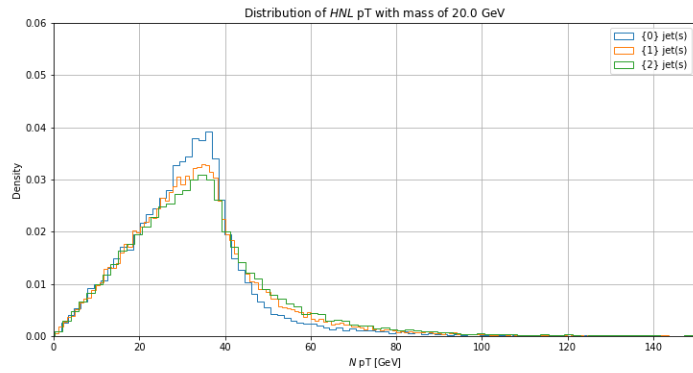
Turning now to the p_T distributions of the HNL, shown in Fig. 8.2, these display a similar trend to the p_T distributions of the mother particle W – the distributions are shifted upwards when jets are included. Here there is a shift towards lower p_T values as M_N increases and becomes comparable to M_W . In the case of $M_N \ll M_W$ the HNL p_T distribution peaks around $M_W/2 \approx 40$ GeV, after which there is a sharp decrease, sharpest in the case of no jets.

Moving on to the p_T distributions of the W 's and HNL's decay products, namely the primary (τ^+), secondary (τ^+), and tertiary (μ^-) charged leptons, we are one step closer to the kinematic quantities relevant to the triggers, as we are nearing observable quantities. These p_T distributions are shown in Fig. 8.2. The primary tau is created at the same vertex as the HNL, and so the p_T distributions of this lepton mirror the corresponding HNL distributions due to the conservation of momentum at each vertex. The secondary and tertiary leptons' distributions are shifted to lower values of p_T , again due to momentum conservation, along with the fact that they are decay products of the HNL – one step further 'out' in the decay chain.

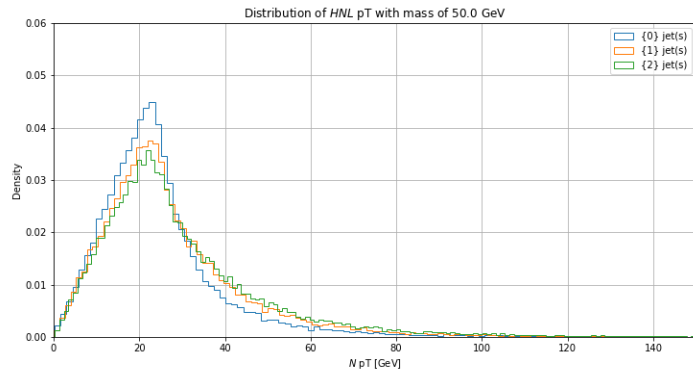
The only directly observable quantity (in the ATLAS detector) discussed here so far is the p_T of the muon. And this is where the search for HNLs coupled to τ flavour starts



(a) Normalised distributions of HNL p_T , for up to 0, 1 and 2 jets, $M_N = 5$ GeV



(b) Normalised distributions of HNL p_T , for up to 0, 1 and 2 jets, $M_N = 20$ GeV



(c) Normalised distributions of HNL p_T , for up to 0, 1 and 2 jets, $M_N = 50$ GeV

Figure 8.2.: Normalised HNL p_T distributions for up to 0, 1 and 2 jets, at $M_N \in [5, 20, 50]$ GeV.

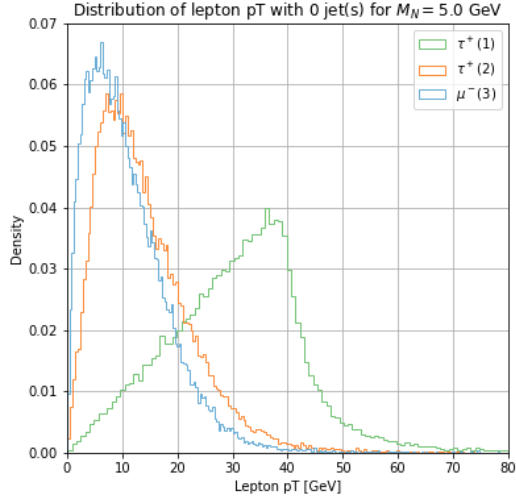
diverging from those coupled to e or μ flavour – unlike the electron or muon, tau decays within the detector, and only its decay products are detected. Besides the technical challenge of reconstructing a tau lepton from its detected decay products, the fact that tau decays, means the production of a tau neutrino, which in turn carries energy, and thus transverse momentum, away undetected. Since the tau triggers considered in this thesis, described in Sec. 5.4, are made to detect hadronically decaying taus, it is the ‘visible’ hadronic decay products of the taus ($\tau_{\text{had-vis}}$) which are of interest here [79]. There are many possible hadronic decay modes of tau leptons, most commonly classified by the number of charged particles are found among its decay products – these are referred to as 1-, 3-, 5-prong (etc.) decays [81].

The amount of different hadronic decay modes combined with the ‘manual’ approach to reading the event structures of the generated data is a potential headache. However, only branching ratios greater than 0.04% are implemented in the PYTHIA tau decay [97]. This means only 1- and 3-prong tau decays are counted in, which simplifies the data analysis a little. A way to simplify the data analysis a lot more is simply by reconstructing the $\tau_{\text{had-vis}}$ momentum from the tau-momentum at the decay vertex and the ν_τ momentum right after the decay vertex. The $\tau_{\text{had-vis}}$ is constituted by charged and neutral hadrons, observed in the hadronic calorimeters [98]. Besides from the ν_τ , escaping the detector as missing energy, and the $\tau_{\text{had-vis}}$, deposited in the calorimeters, a photon may be produced, and is (as far as we know) not counted in the $\tau_{\text{had-vis}}$. The hadronic τ -decay modes involving photons, constitute roughly $\Gamma(\tau \rightarrow \text{had} + \gamma) / \Gamma(\tau \rightarrow \text{all}) \approx 10^{-3}$, see Fig. 8.4. This effectively means that all decay products from the taus (in PYTHIA) are visible to the detector, except for ν_τ . The p_T of the hadronically visible decay products of the primary and secondary taus, reconstructed as described above, are shown in Fig. 8.5. Comparing these distributions to those in Fig. 8.3, it is clear that a lot of transverse momentum is lost to the tau neutrino, and herein lies one of the challenges of a search for HNLs coupled to tau flavour.

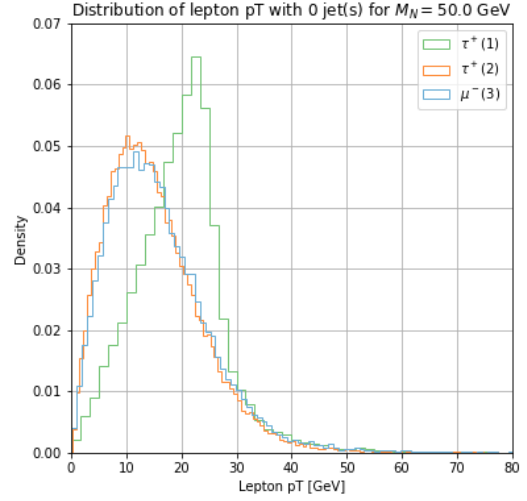
The final kinematic property relevant to the trigger conditions is the angular separation of the taus, ΔR . Examples of these distributions are shown in Fig. 8.6.

8.2 Detector Efficiency

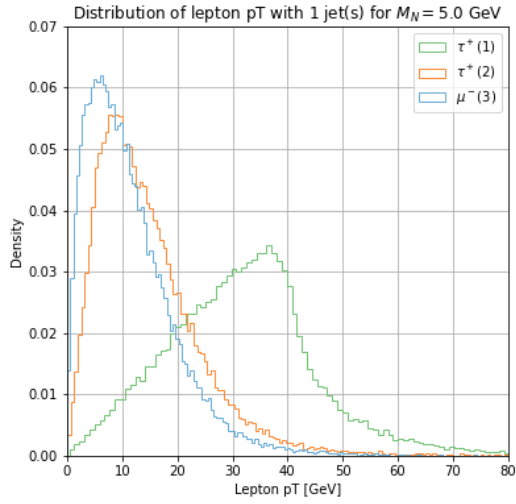
In order to determine how sensitive, if at all, a given experiment is to a hypothesis, the efficiency of the experiment must be found. In this case the experiment is the ATLAS detector, and the hypothesis is the existence of a single HNL coupled to τ . The efficiency is represented as the last term in Eq. 8.0.1, and expresses what fraction of a



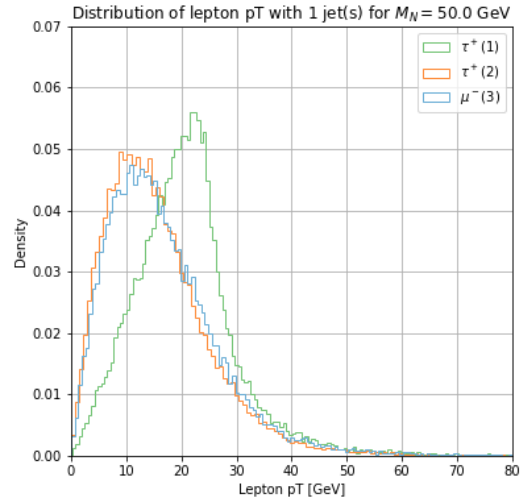
(a) Lepton p_T , 0 jets, $M_N = 5$ GeV



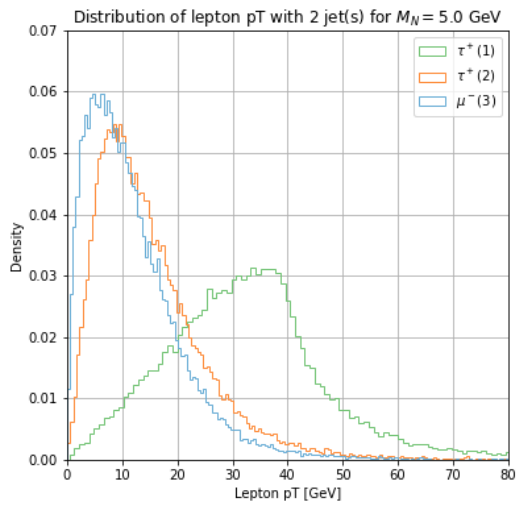
(b) Lepton p_T , 0 jets, $M_N = 50$ GeV



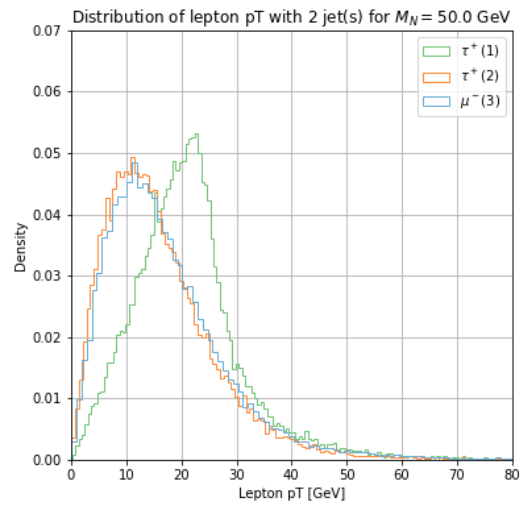
(c) Lepton p_T , 1 jet, $M_N = 5$ GeV



(d) Lepton p_T , 1 jet, $M_N = 50$ GeV



(e) Lepton p_T , 2 jets, $M_N = 5$ GeV



(f) Lepton p_T , 2 jets, $M_N = 50$ GeV

Figure 8.3.: Normalised distributions of primary, secondary and tertiary leptons' p_T for $M_N = 5, 50$ GeV.

Γ_{31}	$a_1(1260)\nu_\tau \rightarrow \pi^- \gamma \nu_\tau$	$(3.8 \pm 1.5) \times 10^{-4}$	∨
Γ_{32}	$K^- \geq 0\pi^0 \geq 0K^0 \geq 0\gamma \nu_\tau$	$(1.552 \pm 0.029)\%$	820 ∨
Γ_{33}	$K^- \geq 1 (\pi^0 \text{ or } K^0 \text{ or } \gamma) \nu_\tau$	$(8.59 \pm 0.28) \times 10^{-3}$	∨

Figure 8.4.: Hadronic decay modes of the τ lepton including a photon. From PDG website: <https://pdglive.lbl.gov/Particle.action?node=S035&init=0>

Quality Cuts	
e	μ
$p_T(e) > 4.5 \text{ GeV}$	$p_T(\mu) > 4.0 \text{ GeV}$
$ \eta(e) \in [0, 1.37] \cup]1.52, 2.47[$	$ \eta(\mu) < 2.5$

Table 8.1.: Specifications for applying the ‘quality’ cuts to e and μ , from Table 1 in [42]. Only processes involving μ as the tertiary charged lepton are explicitly considered in this thesis.

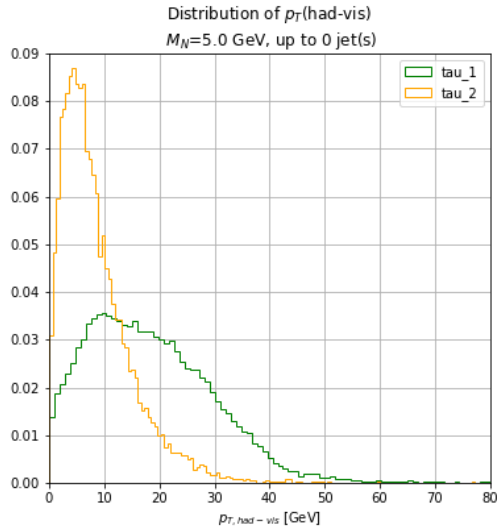
given signal produced in the experiment would be measured and classified correctly. And so, the efficiency is a measure of detection, rather than production.

Since this thesis is examining the potential use of the $\tau\tau$ triggers described in Sec. 5.4, only events where both taus decay hadronically are allowed to ‘pass’*. For this reason, the first sorting of the data is to select all events where both taus decay hadronically. This should reduce the signal with a factor corresponding to the square of the hadronic branching ratio of τ : $(\text{BR}(\tau \rightarrow \text{hadrons}))^2 \approx (0.648)^2 = 0.42$ [81]. This corresponds to the top line in Fig. 8.7. Secondly, the events in which the muon (tertiary charged lepton) passes the ‘quality cuts’/minimum requirements are selected, as listed in Table 8.1. Thirdly, the relevant trigger criteria are applied. The full list of criteria from the $\tau\tau$ triggers are outlined in Sec. 5.4, however only the penultimate set of trigger conditions are applied here. The events are counted as passing if the following trigger conditions are met:

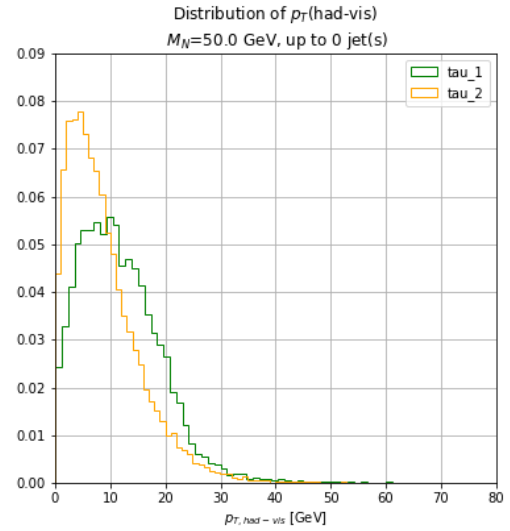
- $p_T(\tau_{\text{leading}}) > 40 \text{ GeV}$
- $p_T(\tau_{\text{subleading}}) > 30 \text{ GeV}$
- $\Delta R(\tau, \tau) < 2.6$

The resulting efficiencies are presented as a ‘cut flow’ diagram in Fig. 8.7.

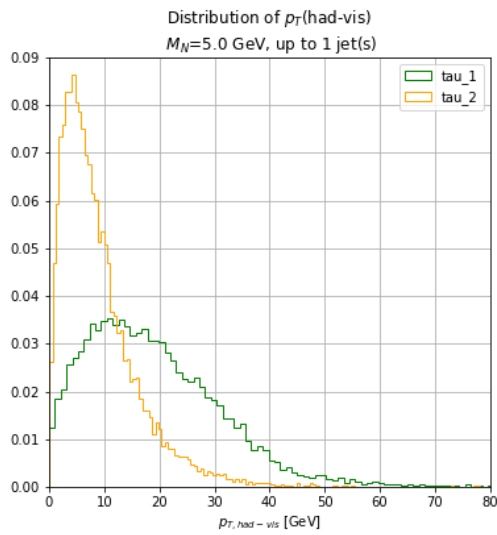
*If the leptonically decaying taus were considered, these would interfere with the tripleton signatures of the existing ATLAS searches, and would require taking HNLs coupled to e and/or μ into consideration as well.



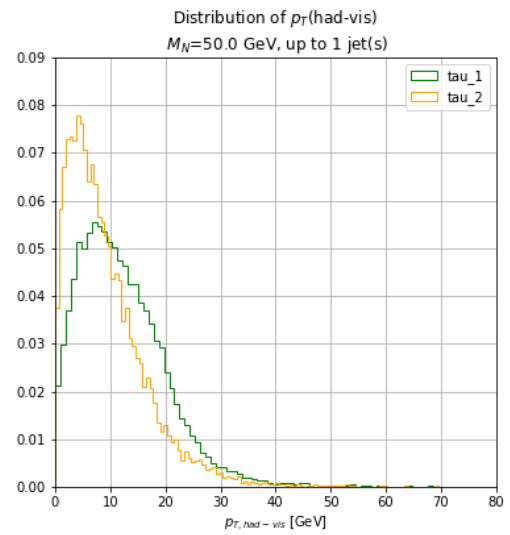
(a) Lepton p_T , 0 jets, $M_N = 5$ GeV



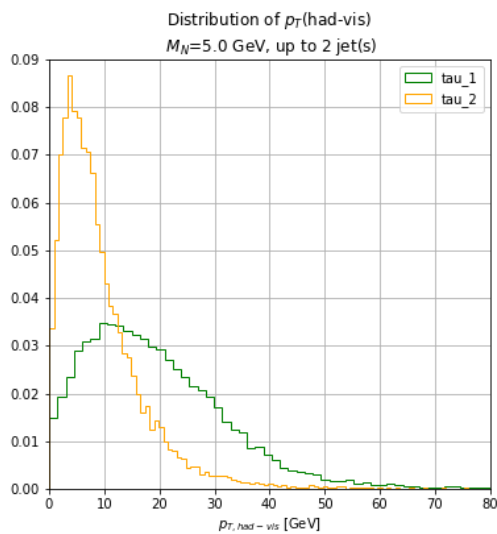
(b) Lepton p_T , 0 jets, $M_N = 50$ GeV



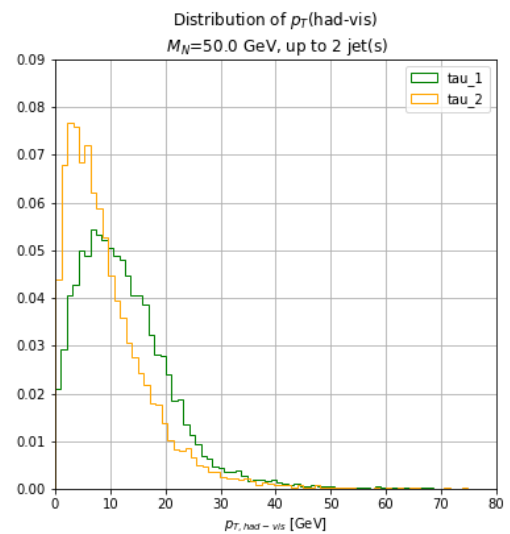
(c) Lepton p_T , 1 jet, $M_N = 5$ GeV



(d) Lepton p_T , 1 jet, $M_N = 50$ GeV



(e) Lepton p_T , 2 jets, $M_N = 5$ GeV



(f) Lepton p_T , 2 jets, $M_N = 50$ GeV

Figure 8.5.: Normalised distributions of primary and secondary taus' visible hadronic p_T components for $M_N = 5, 50$ GeV.

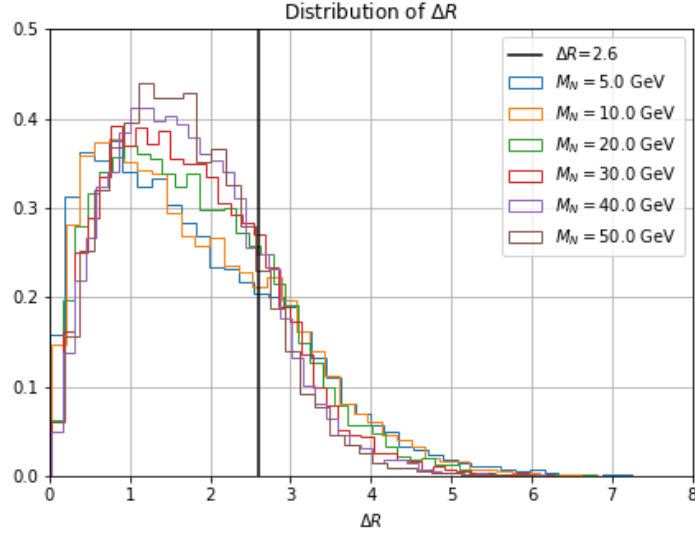


Figure 8.6.: Normalised distributions of $\Delta R(\tau_{1,\text{had-vis}}, \tau_{2,\text{had-vis}})$. These are from the data set without jets, but there are no major differences in the distributions between the data sets.

A few caveats need mentioning: The trigger’s criteria of isolation has been disregarded. The reason for not applying the remaining sets of trigger conditions shown in Fig. 5.7 is that they all[†] involve a lower bound on the transverse momentum of a jet. Reconstructing the momentum of a jet ‘manually’ from the HEPMC output files of PYTHIA is unfeasible, and we have not had any success with integrating existing software designed for this purpose in my scripts for data analysis. This is also the reason for neglecting the isolation criteria, since the unknown jet momentum would be important in this context too.

As seen in Fig. 8.7 The requirements on the kinematics of μ lowers the efficiency by roughly half an order of magnitude, the requirement on $\Delta R(\tau, \tau)$ leaves the efficiencies virtually unchanged, whereas the p_T requirements on τ reduce the efficiencies by 1-2 orders of magnitude. Comparing the final, cumulative efficiencies between the three cases, there is an upwards trend moving from left to right, most notably between the left and right panels, indicating that the efficiency increases with allowing (more) hard jets. When considering that the most limiting requirements to the signal are those pertaining to $p_T(\tau)$, along with the fact that the presence of hard jets allows an, on average, larger p_T component to the W, and subsequently its decay products, it is not all together surprising that the efficiency goes up with the number of jets. For this reason it would be tempting to add an increasingly higher number of hard jets in the

[†]Except the very first trigger condition, requiring $p_T(\tau) > 170$ GeV. This condition would not add any significant efficiency, since the ‘primary’ τ , on average the leading τ in the type of process considered, is very unlikely to even reach half the required p_T . See e.g. Fig. 8.5d.

pursuit of larger efficiencies. However, the cross section of W production alongside N hard jets decreases as N increases, see e.g. Fig. 5 in [82]. This means that the results of allowing for a higher number of hard jets would yield diminishing returns. For this reason [‡] we decided to generate most of the data represented in this thesis allowing for up to 2 hard jets.

8.3 Prompt & Displaced Searches

Now that the generated data has been passed through the trigger conditions, it is time to consider whether the HNLs actually decay to visible (SM) particles within the detector, or if they escape the detector all together. This is of course highly dependent on where a given HNL falls within the $|\theta_{N\tau}|^2 - M_N$ parameter space. The lower the mixing angle, the less the HNL interacts with SM particles and thus the HNL becomes more long lived. Similarly, HNLs become longer lived the lighter their mass. Generally speaking an event, such as an HNL decaying within the ATLAS detector, can fall into one of 3 scenarios:

1. The HNL decays more or less instantaneously, travelling shorter than the distance the detector is able to discern as different from its production point. This is referred to as a *prompt* event.
2. The HNL travels a distance great enough to be classified as different from the point of origin by the detector, but still within the relevant tracker of the detector, for the decay products to be measured. This is referred to as a *displaced* event.
3. The HNL is so long lived that it escapes the detector before decaying.

Case 3. is of course irrelevant for this thesis[§], which leaves the prompt and displaced cases. What exactly is considered prompt or displaced varies from search to search – it depends on the kind of signal searched for, the triggers used and the background expected. In this thesis the demarcation between a prompt and displaced event is adapted from [99], and is set to be a total displacement of $d = 1.0$ mm.

To accommodate the technical constraints as well as time constraints of this thesis, the following simplified model for the calculation of displacement has been adapted. In actual ATLAS searches, different displacement requirements are placed on the

[‡]Along with other reasons, which shall become apparent when discussing displaced sensitivities in Sec. 8.5.

[§]Though long lived ‘exotic’/BSM particles, e.g. HNLs, could be searched for in experiments such as the proposed SHiP experiment[73] at CERN.

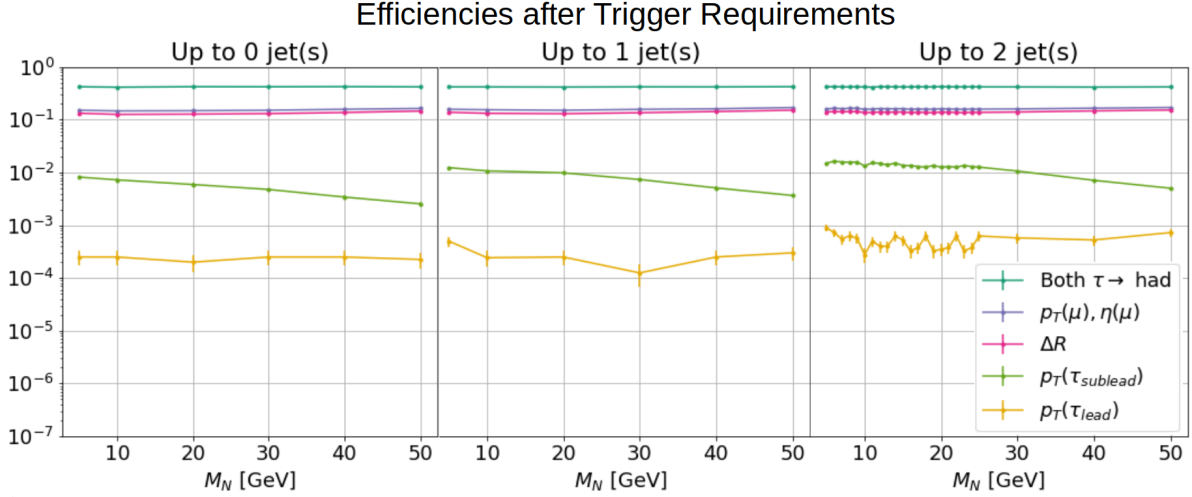


Figure 8.7.: A cut flow diagram, showing the impact on efficiency of each requirement described in Sec. 8.2. The efficiencies are measures of the fraction of generated events to pass the requirements. Each data point represents 40,000 events generated in MG and PYTHIA. From left to right the panels show data for events including up to 0, 1 and 2 hard jets. From top to bottom the curves cumulatively represent: *Teal*: Requiring both taus to decay hadronically, corresponding to $(\text{BR}(\tau \rightarrow \text{hadrons}))^2 \approx 0.42$ [81]. *Purple*: Requiring $p_T(\mu) > 4.0$ GeV and $|\eta(\mu)| < 2.5$. *Pink*: Requiring the angular separation of the taus be $\Delta R(\tau, \tau) < 2.6$. *Green*: Requiring the subleading tau, on average the secondary lepton, $p_T(\tau_{\text{sublead}}) > 30$ GeV. Here only the visible hadronic decay products are considered. *Yellow*: Requiring the leading tau, on average the primary lepton, $p_T(\tau_{\text{lead}}) > 40$ GeV. Again, only the hadronic visible decay products are counted in. The requirements on the kinematics of μ lowers the efficiency by roughly half an order of magnitude, the requirement on $\Delta R(\tau, \tau)$ leaves the efficiencies virtually unchanged, whereas the p_T requirements on τ reduce the efficiencies by 1-2 orders of magnitude. Comparing the cumulative efficiencies (yellow) between the three panels, there is an upwards trend moving from left to right, most notably between the left and right panels, indicating the efficiency increasing with allowing more hard jets. The errors on each data point is taken to be the square root of the number of surviving events, assuming this follows a Poisson distribution, and then normalised by the number of total events.

longitudinal and the transverse displacement of a particle. This is due to the toroidal shape of the ATLAS detector. However we have approximated the ATLAS detector to be spherically symmetric when considering HNL displacement in this thesis, and so left the distinction between longitudinal and transverse displacement out. The probability of an HNL decaying before reaching the minimal displacement is given by:

$$P_{\text{Decay}}^{\text{Prompt}} = 1 - \exp\left(-\frac{d_{\text{min}}}{\gamma c \tau_{\text{SI}}}\right), \quad (8.3.1)$$

and similarly for the displaced case:

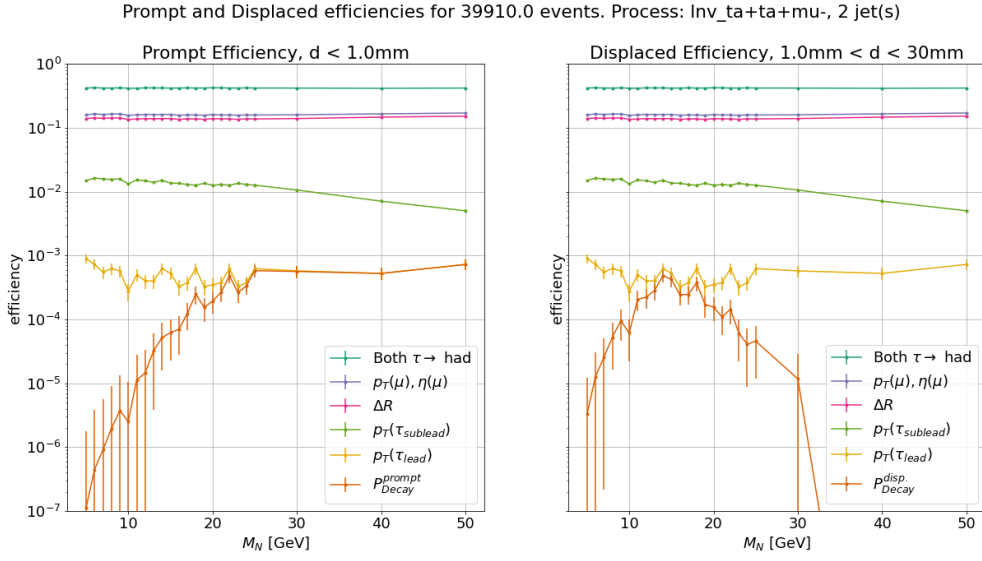
$$P_{\text{Decay}}^{\text{Disp.}} = \exp\left(-\frac{d_{\text{min}}}{\gamma c \tau_{\text{SI}}}\right) - \exp\left(-\frac{d_{\text{max}}}{\gamma c \tau_{\text{SI}}}\right), \quad (8.3.2)$$

where γ is the HNL's Lorentz factor, c is the speed of light and τ_{SI} is the HNL half life in SI units. τ_{SI} , being the inverse of the HNL decay width Γ_N , depends on M_N and $|\theta_{N\tau}|^2$. This dependency is discussed in Sec. 7.2.

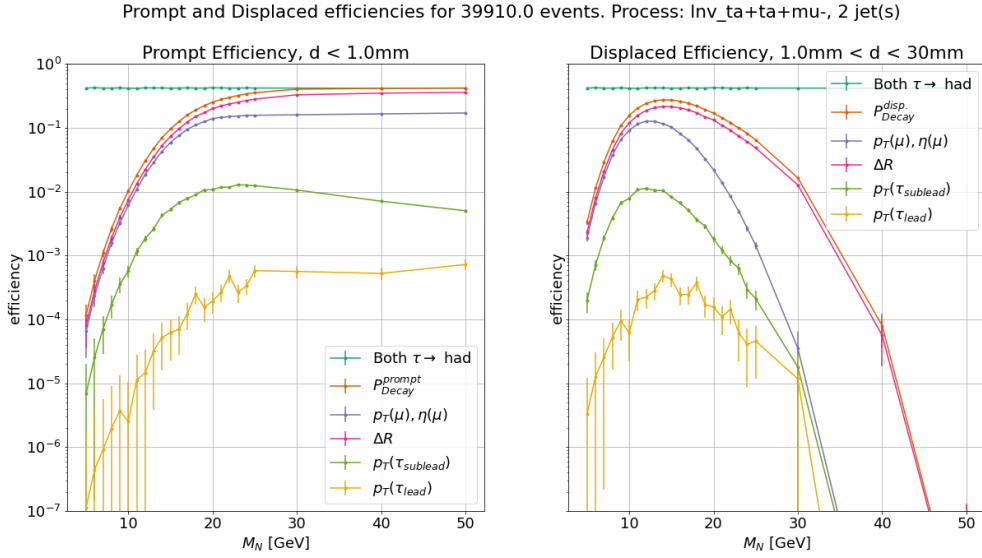
When applying the simplified displacement criteria to the generated events, it is done in the following way:

1. For each event the Lorentz factor is calculated, using the relation $\gamma = \frac{E}{M_N}$.
2. For each mass the half life is calculated based on the MG generated decay width, scaled to the benchmark $|\theta_{N\tau}|^2 = 10^{-6}$, see Table 8.2.
3. Each event, i , is then ascribed two decay weights in the range $[0, 1]$: One representing $P_{\text{Decay}}^{\text{Prompt}}(N_i)$ and one for $P_{\text{Decay}}^{\text{Disp.}}(N_i)$, following the definitions in Eq. (8.3.1) and (8.3.2).
4. The prompt and displaced decay weights respectively are then summed for each event surviving the trigger conditions in Sec. 8.2. This gives rise to an approximation of a prompt and displaced efficiency.

The resulting efficiency estimates are shown in Fig. 8.8, for the generated data allowing for up to 2 hard jets. Since this is the type of process yielding the highest acceptance rate from the trigger conditions, as explained in Sec. 8.2, this is the one generated with the highest resolution in M_N , wherefore it is also best suited to show trends in decay probability. The efficiency estimates for the processes with 0 jets and up to 1 jet are found in Appendix C.



(a) Cut flow diagrams of estimated efficiencies identical to the right most panel in Fig. 8.7, with the final addition of prompt (*left*) and displaced (*right*) decay weights for each event passing the trigger conditions.



(b) Cut flow diagram with the same end result as the one in Fig. 8.8a, but where the prompt (*left*) and displaced (*right*) decay weights are applied immediately after the branching ratio, $(\text{BR}(\tau \rightarrow \text{hadrons}))^2$. This is done to illustrate the shape of the decay probability curves, unobscured by the efficiencies after cuts and trigger requirements.

Figure 8.8.: Estimated prompt (*left*) and displaced(*right*) efficiencies for detection of the tri-lepton signature $\tau^+\tau^+\mu^-$ in the ATLAS detector, allowing for up to 2 hard jets. The branching ratio, cuts and trigger requirements are those described in Sec. 8.2, and the decay weights are calculated as outlined in Sec. 8.3. Each value of M_N marked with a data point represents a simulation of 40 000 events. The displacement demarcations used are: *Prompt* $d < 1$ mm and *displaced* $1 \text{ mm} \leq d \leq 30$ mm.

Observing Fig. 8.8, especially 8.8b, since here the decay probability is applied first and therefore more directly intelligible: For the benchmark of $|\theta_{N\tau}|^2 = 10^{-6}$, and the definition of $d_{\min} = 1.0$ mm the probability of a promptly decaying HNL is almost 1 for $M_N \gtrsim 25$ GeV, below which the probability of prompt decay decreases sharply as M_N decreases. Reducing $|\theta_{N\tau}|^2$ would result in moving the point at which the prompt decay probability reaches ≈ 1 to higher values of M_N . For the same benchmark in $|\theta_{N\tau}|^2$, the probability of an HNL decaying displaced, reaches its maximum around $M_N \approx 15$ GeV. For lower masses the HNL is likely to move beyond d_{\max} before decaying, whereas for higher masses, the HNL is more likely to decay promptly. If $|\theta_{N\tau}|^2$ is decreased the top of the displaced decay probability curve would move towards lower values of M_N . Similarly adjusting d_{\min} and d_{\max} will affect the decay probabilities: Decreasing d_{\min} will for the prompt probability shift the point at which it approaches 1 towards higher masses, whereas for the displaced, this would widen the peak of the probability curve towards higher HNL masses. On the other hand increasing d_{\max} will widen the maximum of the displaced probability curve towards lower values of M_N .

This leads us to a few comments on the choices of d_{\min} and d_{\max} : Requiring a displaced HNL decay vertex dramatically reduces the SM model background [88]. In the 2019 ATLAS HNL search, for HNLs coupled to e and μ , the minimum radial displacement is set to $d = 4.0$ mm, while the constraint of same sign charge of the primary and secondary leptons is relinquished for the displaced search. This displacement requirement ensures a virtually SM background free[¶] search. In this thesis the minimum displacement is kept, non-directionally, at $d = 1.0$ mm, however the same sign charge requirement for the primary and secondary leptons is maintained, which will help to reduce any SM background. In the 2019 ATLAS HNL search, the maximal displacement is set at $d_{\max} = 300$ mm (radially), meaning displaced HNLs decaying up until reaching the innermost silicon microchip tracker (SCT) are considered. In this thesis however, the HNL search attempts the utilisation of the ATLAS $\tau\tau$ triggers, which have been optimised for tau pairs which share a production vertex, as would be the case for tau pairs produced from tree level decay of a Higgs boson. For this reason, setting $d_{\max} = 300$ mm would be unfeasible, since the triggers are likely very ineffective at this displacement. For this reason, the maximal (total) HNL displacement is set to $d_{\text{textmax}} = 30$ mm^{||} for the following analysis in this thesis.

[¶]As discussed in [88]: Background due to cosmic radiation, interaction with the detector material, metastable hadrons decaying or accidental crossing of particle tracks will be present, despite displacement criteria. These types of background are reduced by around one order of magnitude by the added requirement of a prompt lepton (here in the ATLAS paper this would be e or μ , but in this thesis τ) vertex in the same event as the displaced lepton vertex.

^{||}This is done after private communication with S. Xella.

8.4 On Rescaling a MadGraph HNL Cross Section

Before being able to move further in the analysis of the generated data and tackle the rest of Eq. (8.0.1), it is important to examine how to ‘translate’ the differential cross sections provided by the event generator into the corresponding physically meaningful cross section. The methods of rescaling presented in this section are based on [42], section 3.2.2.

In order to take advantage of the numerical wizardry of event generators, certain accommodations must be made. The HeavyN model relies on the use of ‘narrow-width approximation’, which means that the reference input parameter, Γ_{ref} , used for event generation must be $\ll 1$. However, setting this reference parameter too low, e.g. around $\Gamma_{\text{ref}} \approx \mathcal{O}(10^{-8})$ GeV, a conceivable size for an HNL in the considered mass range, see Fig. 7.5, would cause issues with the numerical integration of the event generator, and lead to very long run times and/or cross sections being 0. The same issue arises from setting the reference mixing angle θ_{ref} too low. To avoid these issues the reference parameters used throughout this thesis are: $|\theta_{\text{ref}}| = 10^{-3}$ and $\Gamma_{\text{ref}} = 3.03 \cdot 10^{-2}$ GeV**.

Now, since the generated data has been generated using the reference parameters described above, the obtained cross sections must be rescaled. This can be done by exploiting the straightforward dependence of the cross section for a given process on the reference parameters:

$$\sigma(P) \propto \frac{|\theta_{\alpha(P)}|^2 |\theta_{\beta(P)}|^2}{\Gamma_N}, \quad (8.4.1)$$

where α and β can be any of the three SM lepton flavours, e, μ, τ , but in the case of this thesis, they are both τ . Thus the cross section reported by MadGraph can be rescaled using the following relation:

$$\sigma(M_N, \theta_e, \theta_\mu, \theta_\tau) = \sigma_P^{\text{ref}} \times \frac{|\theta_{\alpha(P)}|^2 |\theta_{\beta(P)}|^2}{|\theta_{\text{ref}}|^4} \times \frac{\Gamma_{\text{ref}}}{\Gamma(M_N, \theta_e, \theta_\mu, \theta_\tau)} \quad (8.4.2)$$

Again, both α and β are τ in the processes considered here, and so $|\theta_{\alpha(P)}|^2 |\theta_{\beta(P)}|^2 \rightarrow |\theta_{N\tau}|^2$. As explained in Sec. 7.2, when the mixing angles $\theta_e = \theta_\mu = 0$, the HNL decay width $\Gamma(M_N, \theta_e, \theta_\mu, \theta_\tau)$ reduces to $\Gamma(M_N, \theta_\tau)$, and so the physical cross section, $\sigma(M_N, \theta_e, \theta_\mu, \theta_\tau)$ is reduced to $\sigma(M_N, \theta_\tau)$. In Eq. (8.4.2) the reference cross section σ_P^{ref} corresponds to the cross section reported by MG.

**This value seems oddly specific for a reference parameter, but was simply chosen because it was a default parameter of the HeavyN model. It carries no deeper meaning.

8.5 Single Event Sensitivity

In Sec. 8.2 we obtained an estimated efficiency, as a function of M_N , of the ATLAS detector in detecting the tri-lepton HNL signature $\tau^+\tau^+\mu^-$, for a single HNL coupled only to τ , in which taus decay hadronically. This was done both for a prompt and displaced case. These efficiencies are a measure of what fraction of such events the ATLAS detector could be expected to measure, given the hypothesis of HNLs. However, this on its own doesn't tell us much about how suitable the ATLAS detector is in such a search. What is ultimately of interest is to obtain a measure for the experiment's sensitivity to the HNL hypothesis, as measured in the M_N - $|\theta_{N\tau}|^2$ parameter space of the hypothesis. This will, in the absence of a discovery, allow for an extended exclusion region in the parameter space of the hypothesis. It will also allow the comparison of ATLAS' sensitivity to the sensitivities of other experiments.

One way to quantify the sensitivity of an experiment is through calculating a 'Single Event Sensitivity' (SES). The SES is a measure for where in the M_N - $|\theta_{N\tau}|^2$ parameter space it would be expected for a given experiment to be able to observe a single event, and thus being a measure of the limit of the experiment's sensitivity towards the hypothesis in question. This limit is found by, once again, turning to the Eq. (8.0.1), setting $N_P = 1$, hence the 'single event', and solving for $|\theta_{N\tau}|^2$:

$$N_P = 1 = \mathcal{L}_{\text{int.}} \times \sigma_{\text{real}}^{(P)} \times \text{BR}(\tau \rightarrow \text{had.})^2 \times \epsilon_{\text{detector}} \times P_{\text{Decay}} \quad (8.5.1)$$

Writing the rescaled cross section out in more detail, as explained in Sec. 8.4, part of the dependence on $|\theta_{N\tau}|^2$ becomes explicit:

$$N_P = 1 = \mathcal{L} \times \sigma_{\text{MG}}^{(P)} \times \frac{|\theta_{N\tau}|^4}{|\theta_{\text{ref}}|^2} \times \frac{\Gamma_{\text{ref}}}{\Gamma_N(M_N, \theta_\tau)} \times \text{BR}(\tau \rightarrow \text{had})^2 \times \epsilon_{\text{detector}} \times P_{\text{Decay}} \quad (8.5.2)$$

Eq. (8.5.2) simplifies a little since the HNL, in the constellation considered here, only couples to τ , and hence the decay width only depends on θ_τ : $\Gamma_N(M_N, \theta_\tau) = |\theta_{N\tau}|^2 \hat{\Gamma}_N(M_N)$.

The second $|\theta_{N\tau}|^2$ dependence is found in the probability of decay, either within the prompt or displaced regions of the detector, as outline in Sec. 8.3:

$$P_{\text{Decay}}^{\text{Prompt}} = 1 - \exp\left(-\frac{d_{\text{min}}}{\gamma c \tau_{\text{SI}}}\right) \quad (8.5.3)$$

$$P_{\text{Decay}}^{\text{Disp.}} = \exp\left(-\frac{d_{\text{min}}}{\gamma c \tau_{\text{SI}}}\right) - \exp\left(-\frac{d_{\text{max}}}{\gamma c \tau_{\text{SI}}}\right), \quad (8.5.4)$$

where the HNL lifetime is given by $\tau_{\text{SI}} = \hbar/\Gamma_N(M_N, \theta_\tau) = \hbar/|\theta_{N\tau}|^2 \hat{\Gamma}_N(M_N)$.

The remaining factors of Eq. (8.5.2) are simply the following constants: The MG generated cross sections (Table 8.3) and HNL decay widths (Table 8.2), the known branching ratio of $\text{BR}(\tau \rightarrow \text{hadrons}) = 64.79 \pm 0.06$ [81], the reference parameters $|\theta_{\text{ref}}|^2 = 10^{-6}$ and $\Gamma_{\text{ref}} = 3.03 \cdot 10^{-2}$, the detector efficiencies seen in Fig. 8.7, and finally the integrated luminosity.

The displaced version of Eq. (8.5.1) now takes the form:

$$1 = k_1 \left(e^{-k_2 x} - e^{-k_3 x} \right) \quad (8.5.5)$$

This is a transcendental equation without an analytical solution, so we proceed by solving numerically for $|\theta_{N\tau}|^2$. Both the prompt and displaced equations have been solved for three different values of the integrated luminosity:

1. The current ATLAS integrated luminosity as Run 2 has been concluded: $\mathcal{L} = (139 \pm 2) \text{ fb}^{-1}$ [75].
2. The projected ATLAS integrated luminosity at the end of Run 3: $\mathcal{L} = (300 \pm 2) \text{ fb}^{-1}$ [100].
3. The projected ATLAS integrated luminosity at the end of the High Luminosity LHC run: $\mathcal{L} = (3000 \pm 2) \text{ fb}^{-1}$ [100].

Furthermore the cross section for the process resulting in the tri-lepton signature $\tau^+ \tau^+ \mu^-$ has been multiplied by a factor of 4. This is to approximate the contribution of the process resulting in the tri-lepton signature $\tau^+ \tau^+ e^-$, as well as both the charge conjugated processes^{††}. The results are shown in Fig. 8.9 and 8.10. These figures show, that if we were looking for just a single HNL event resulting in a tri-lepton signature of the type $\tau^\pm \tau^\pm l_\alpha^\mp$, considering no background, the ATLAS experiment could be sensitive^{‡‡} to HNLs with mixing angles as low as $|\theta_{N\tau}|^2 \approx 5 \cdot 10^{-7}$, both in prompt and displaced searches. However, reality is not background free, nor would the scientific community be satisfied with claiming a discovery of a new particle based

^{††}This assumes lepton universality between e and μ flavours, and neglects the slightly different quality cuts applied to the two flavours in ATLAS (Tab. 8.1). The asymmetry between net positive and net negative electric charge processes in pp collisions has also been neglected in this approximation. We deem these assumptions to be acceptably erroneous, given the general level of precision in the estimations of this thesis.

^{‡‡}Of course accepting the approximations and assumptions described in the previous sections of this thesis as well.

HNL Decay Width	
M_N [GeV]	Γ_N
5.0	$9.414 \cdot 10^{-10} \pm 0.012 \cdot 10^{-10}$
10.0	$4.615 \cdot 10^{-8} \pm 0.003 \cdot 10^{-8}$
20.0	$1.7619 \cdot 10^{-6} \pm 0.0011 \cdot 10^{-6}$
30.0	$1.459 \cdot 10^{-5} \pm 0.001 \cdot 10^{-5}$
40.0	$6.692 \cdot 10^{-5} \pm 0.004 \cdot 10^{-5}$
50.0	$2.278 \cdot 10^{-4} \pm 0.002 \cdot 10^{-4}$

Table 8.2.: The decay widths of HNL for $M_N \in [5, 10, 20, 30, 40, 50]$ GeV, setting $|\theta_\tau|^2 = 1$ and $|\theta_e|^2 = |\theta_\mu|^2 = 0$. Generated in MadGraph as outlined in Sec. 7.2.

HNL Simulated Cross Section			
Process:	$W^+ \rightarrow \tau^+(N \rightarrow \tau^+ \mu^- \bar{\nu}_\mu)$		
M_N [GeV]	σ_{sim} [pb] - No jets	σ_{sim} [pb] - Up to 1 jet	σ_{sim} [pb] - Up to 2 jets
5.0	$8.486 \cdot 10^{-18} \pm 1.2 \cdot 10^{-20}$	$1.245 \cdot 10^{-17} \pm 1.9 \cdot 10^{-20}$	$1.466 \cdot 10^{-17} \pm 1.9 \cdot 10^{-20}$
10.0	$5.262 \cdot 10^{-16} \pm 6.8 \cdot 10^{-19}$	$7.699 \cdot 10^{-16} \pm 1.2 \cdot 10^{-18}$	$9.108 \cdot 10^{-16} \pm 1.3 \cdot 10^{-18}$
20.0	$1.907 \cdot 10^{-14} \pm 2.6 \cdot 10^{-17}$	$2.807 \cdot 10^{-14} \pm 4.2 \cdot 10^{-17}$	$3.305 \cdot 10^{-14} \pm 4.7 \cdot 10^{-17}$
30.0	$1.367 \cdot 10^{-13} \pm 2.0 \cdot 10^{-16}$	$2.012 \cdot 10^{-13} \pm 3.0 \cdot 10^{-16}$	$2.371 \cdot 10^{-13} \pm 3.4 \cdot 10^{-16}$
40.0	$5.010 \cdot 10^{-13} \pm 7.8 \cdot 10^{-16}$	$7.379 \cdot 10^{-13} \pm 1.1 \cdot 10^{-15}$	$8.689 \cdot 10^{-13} \pm 1.5 \cdot 10^{-15}$
50.0	$1.202 \cdot 10^{-12} \pm 1.8 \cdot 10^{-15}$	$1.768 \cdot 10^{-12} \pm 2.7 \cdot 10^{-15}$	$2.088 \cdot 10^{-12} \pm 3.2 \cdot 10^{-15}$

Table 8.3.: The differential cross sections of the process $pp \rightarrow \tau^+ N \rightarrow \tau^+ \tau^+ \mu^-$, with up to 0, 1 and 2 jets, letting PYTHIA8 handle the tau decays and showering. Simulations done for $M_N \in [5, 10, 20, 30, 40, 50]$ GeV, with reference parameters: $|\theta_{\text{ref}}| = 10^{-3}$ and $\Gamma_{\text{ref}} = 3.03 \cdot 10^{-2}$. Generated in MG as outlined in Sec. 6.2.1.

on the observation of a single event – rightly so. But before we discuss these issues further, a discussion on the errors on the sensitivity estimates is in order.

8.5.1 SES Error Propagation

Equation (8.5.1) is an example of a transcendental equation, and therefore has no analytical solution. This means that propagating the error on $|\theta_\tau|^2$ using the standard (analytical) approach with the law of combination of errors is unfeasible[101]. Equation (8.5.1) takes, in the displaced case, the general form:

$$1 = k_1 x \left(e^{-k_2 x} - e^{-k_3 x} \right) \quad (8.5.6)$$

And for the prompt case:

$$1 = k_1 x e^{-k_3 x} \quad (8.5.7)$$

To estimate the error on $|\theta_\tau|^2$ the boot-strap approach would be to repeat the data generation a number of times, and then determine the error from the resulting distribution of $|\theta_\tau|^2$ -values. This approach however is computationally very heavy, and therefore unfeasible within this project.

The method we have chosen for error estimation is instead the following:

1. Propagate the error on the constants k_1 , k_2 and k_3 individually.
2. Solve Eq. (8.5.1) using $k_1 \pm \sigma_1$, $k_2 \pm \sigma_2$ and $k_3 \pm \sigma_3$.
3. Assume the error to follow a Gaussian distribution and take $\sigma_{|\theta|^2} = |\theta|^2(k_1 + \sigma_1, k_2 + \sigma_2, k_3 \pm \sigma_3) - |\theta|^2(k_1 - \sigma_1, k_2 - \sigma_2, k_3 - \sigma_3)$.

In this context σ is of course the standard deviation, rather than the differential cross section, which is its meaning everywhere else in this thesis.

Besides the errors reported by MG on the generated cross section and decay widths, which are reported in Tab. 8.2 and 8.3 and the errors on the (expected) integrated luminosities, there are two significant contributions to the error on the sensitivity estimates: The error on detector efficiencies and the error arising from solving Eq. (8.5.1) using the average Lorentz factor for each M_N considered, rather than solving the equation event by event.

8.6 Exclusion Limits

Now that the concept of sensitivity, as well as how this is calculated, has been established, a discussion of how the sensitivity estimates can be related to existing results is in order. However intuitive the measure of SES might be, it is not all that useful in direct comparison to the existing bounds in the $|\theta_{N\tau}|^2$ - M_N parameter space, as shown in Fig. 4.3c. These exclusion bounds are traditionally given at the 95% CL[41], which we shall approximate in this section.

If the SM background background is assumed to be negligible, i.e. $N_{\text{bkg}} \simeq 0$, the expected number of observed events with the $\tau^\pm\tau^\pm l_\alpha^\mp$ signature is also 0, assuming the HNL hypothesis is false. To this we now add the assumption, that the number of events observed, $N_{\text{HNL, obs.}}$, follow a Poisson distribution. This is assumed, since it is the most appropriate of the common, discrete probability density functions (PDF) to describe a phenomenon with a discrete set of possible outcomes [101]. Ideally we

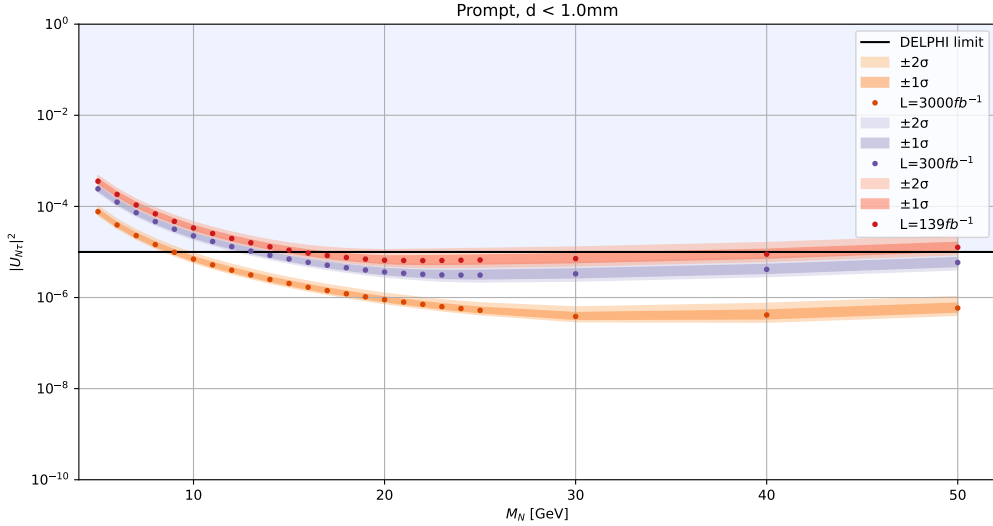


Figure 8.9.: Single event sensitivity for promptly decaying HNLs coupled to τ flavour. The results are shown for three luminosities, from top to bottom curves: *red*: 139 fb^{-1} (Run 2), *purple*: 300 fb^{-1} (Run 3, expected) and *orange*: 3000 fb^{-1} (expected at the end of high-luminosity runs). The maximal displacement is limited to be below 1 mm. Shaded regions show $\pm 1\sigma$ and $\pm 2\sigma$ based on the error estimates (see Section 8.5.1. For comparison, the limits obtained by the DELPHI experiment are shown [47].

would repeat the MG generation of data as described in Ch. 6 a (high) number of times, all using different random ‘seeds’, then repeating the data analysis process on all the data sets, and finally then arrive at a PDF for the distribution of $N_{\text{HNL, obs.}}$. Such a process is called ‘bootstrapping’. However, this is computationally very demanding^{§§}, and thus unfeasible within the scope of this thesis, so the Poisson distribution will do, and is given by [101]:

$$P(n; \lambda) = \frac{e^{-\lambda} \lambda^n}{n!}, \quad (8.6.1)$$

where λ is the mean of the distribution.

With the above assumptions, the question to answer in order to get to a 95% CL on an exclusion bound is: For what mean λ is the probability of measuring 0 events less than or equal to 5%, or $P(0; \lambda) \leq 0.05$? Looking at the first few Poisson distributions reveals that the closet one can get is at $\lambda = 3$, giving $P(0; \lambda = 3) \simeq 0.0498$. Now, to obtain the predicted 95% CL exclusion bound in the $|\theta_{N\tau}|^2 - M_N$ parameter space, we

^{§§}Seeing as each data point on Fig.8.10 represents 40.000 events, including showering, corresponding to 4GB of data, with a runtime of several hours (on my computer), we would be looking at 3-4 weeks of constant simulation to achieve PDFs for the $N_{\text{HNL, obs.}}$ distributions containing just 100 data points each. It would take a disproportionate amount of time, computational power and storage to the, most likely, minuscule deviation it might show in the final expected exclusion bound.

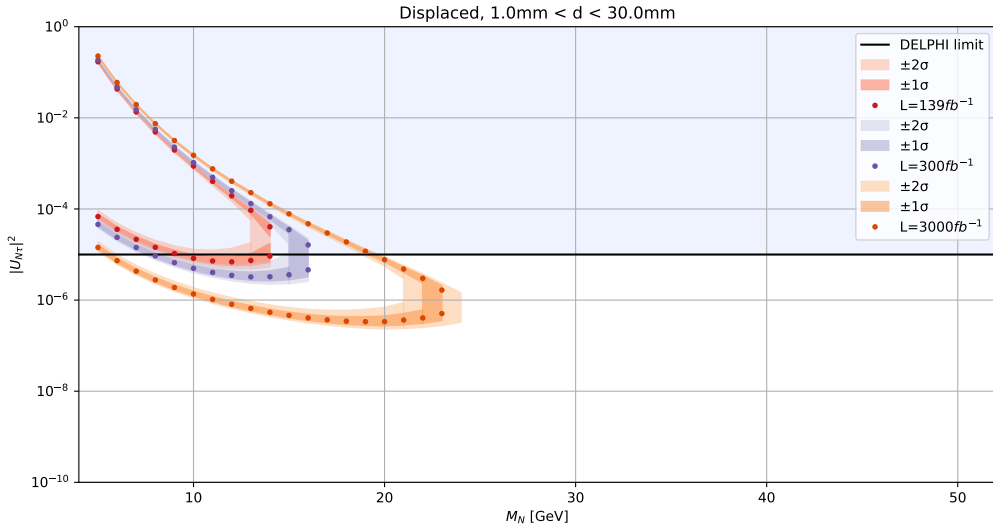


Figure 8.10.: Single event sensitivity for displaced HNLs coupled to τ , decaying within the displacement $1 \text{ mm} \leq d \leq 30 \text{ mm}$. The results are shown for three luminosities, from top to bottom curves: *red*: 139 fb^{-1} (Run 2), *purple*: 300 fb^{-1} (Run 3, expected) and *orange*: 3000 fb^{-1} (expected at the end of high-luminosity runs). The maximal displacement is limited to be below 1 mm. Shaded regions show $\pm 1\sigma$ and $\pm 2\sigma$ based on the error estimates (see Section 8.5.1. For comparison, the limits obtained by the DELPHI experiment are shown [47]. Shaded regions show $\pm 1\sigma$ and $\pm 2\sigma$ based on the error estimates (see Section 8.5.1. The results are based on the average (over events) efficiency, rather than on event-by-event analysis. This approximation may affect the upper boundary of the limit where the dependence on the Lorentz γ factors is exponential. For reference, the previous limits obtained by the DELPHI experiment are shown [47].

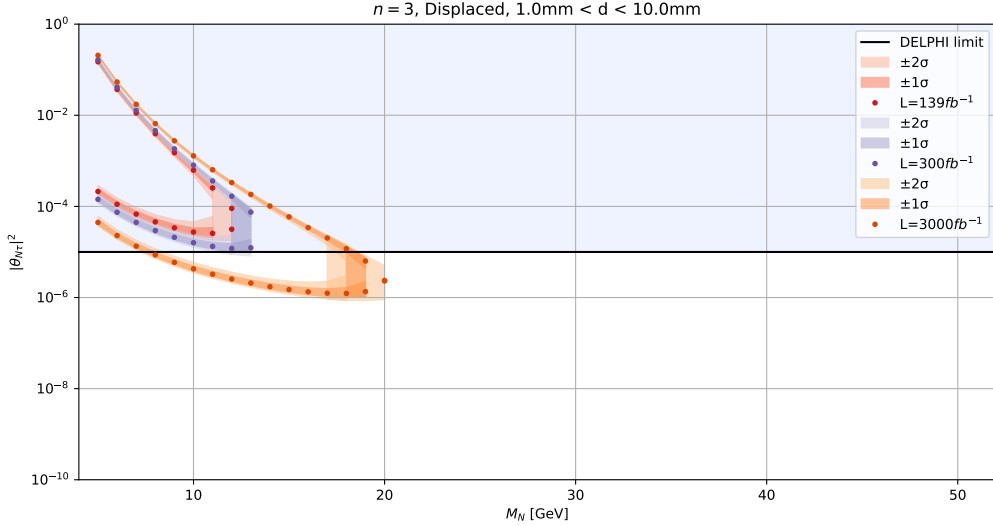


Figure 8.11.: Displaced sensitivity when requiring $N_{\text{events}} = 3$. Decaying within the displacement $1 \text{ mm} \leq d \leq 30 \text{ mm}$. The results are shown for three luminosities, from top to bottom curves: *red*: 139 fb^{-1} (Run 2), *purple*: 300 fb^{-1} (Run 3, expected) and *orange*: 3000 fb^{-1} (expected at the end of high-luminosity runs). This provides the best proxy of an exclusion bound at 95% CL. The DELPHI limit is shown for comparison [47].

repeat the process outline in Sec. 8.5, setting $N_P = 3$ instead of 1. This gives the result shown in Fig. 8.11. Finding the 95% CL exclusion bound is of course a more complex statistical endeavour than the above, but since we do not undertake a proper background analysis in this thesis, setting the expected background event count to anything but zero would be a wildly arbitrary guess.

The prompt sensitivity has been shown in Fig. 8.12 for a varying number of required events, to give a sense of the sensitivity's dependence hereon, but since the assumption of zero SM background cannot reasonably be applied to a prompt search, the remaining analysis pertains only to the displaced search.

Fig. 8.13 shows a parameter exploration of the displaced sensitivities at integrated luminosities $\mathcal{L} = 300 \text{ fb}^{-1}$ and $\mathcal{L} = 3000 \text{ fb}^{-1}$ and minimal displacement $d_{\text{min}} = 1.0 \text{ mm}$, varying d_{max} and the number of events required. This shows that requiring a higher number of observed events, unsurprisingly, results in the raising of the sensitivity bound to higher values of $|\theta_{N\tau}|^2$, but the overall shape of the curve is preserved. On the other hand, increasing d_{max} mainly affects the lower branch of the sensitivity curves, flattening it and so broadening the sensitivity range of M_N to lower masses[¶].

[¶]In Fig. 8.13 the lower branch in the bottom panel has been approximated linearly, because of issues with the numerical solving algorithm. Therefore the bottom panel should be taken as a boundary of $d_{\text{max}} \gg d_{\text{min}}$. The tendency towards the lower branch widening still holds.

Parameter exploration

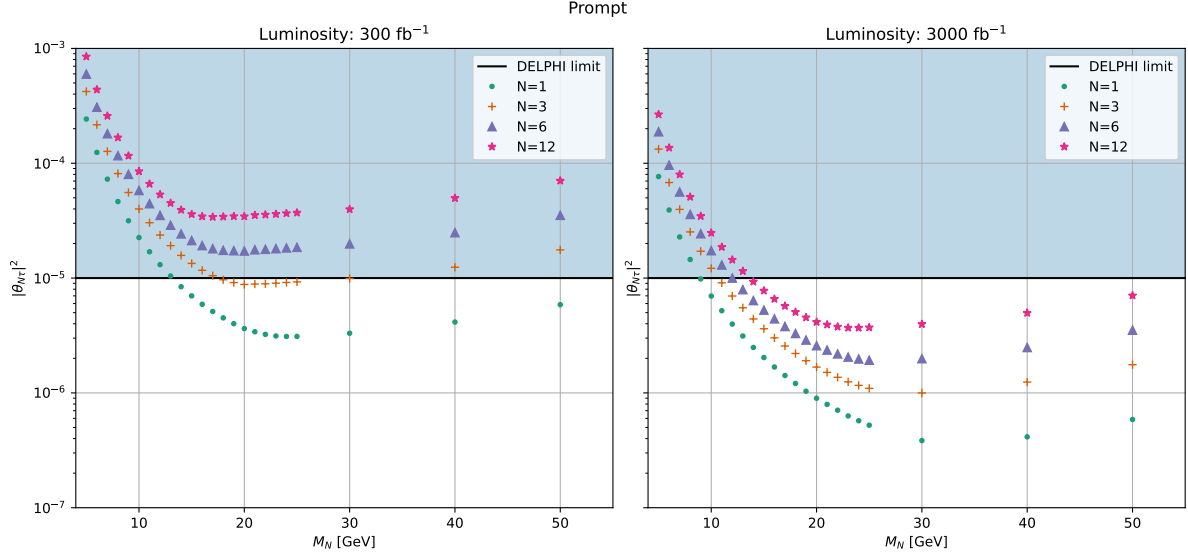


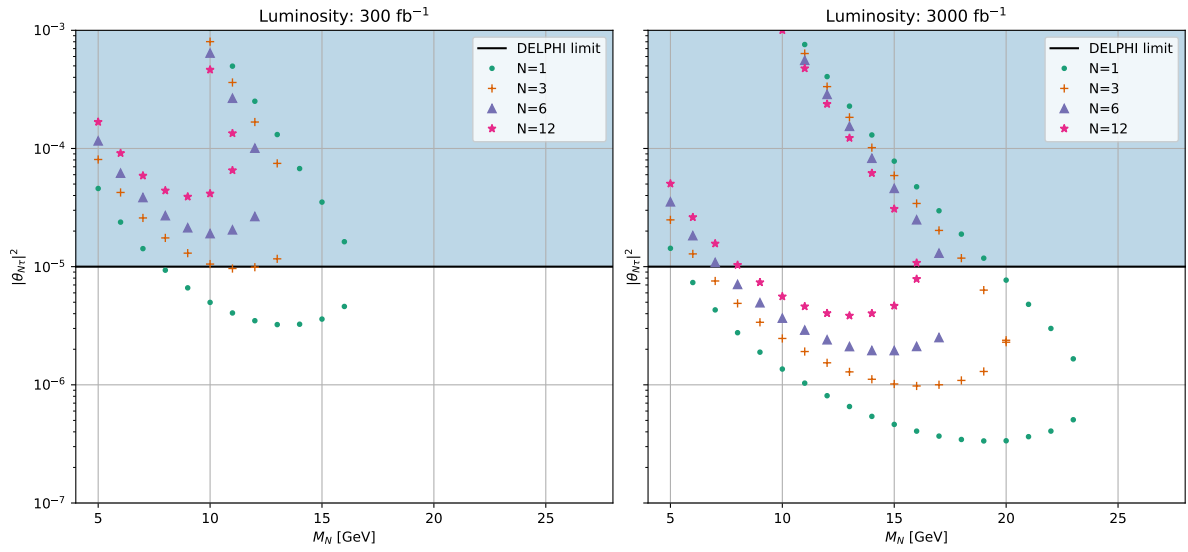
Figure 8.12.: Parameter exploration of prompt ($d_{\max} = 1$ mm) sensitivity estimates for integrated luminosities $\mathcal{L} = 300 \text{ fb}^{-1}$ and $\mathcal{L} = 3000 \text{ fb}^{-1}$, varying the number of events required.

Equivalently the displaced sensitivity is shown in Fig. 8.14 for varying values of d_{\min} . Increasing d_{\min} narrows the shape of the sensitivity curve, as well as shifts the maximum value of M_N to which the experiment is sensitive towards lower masses.

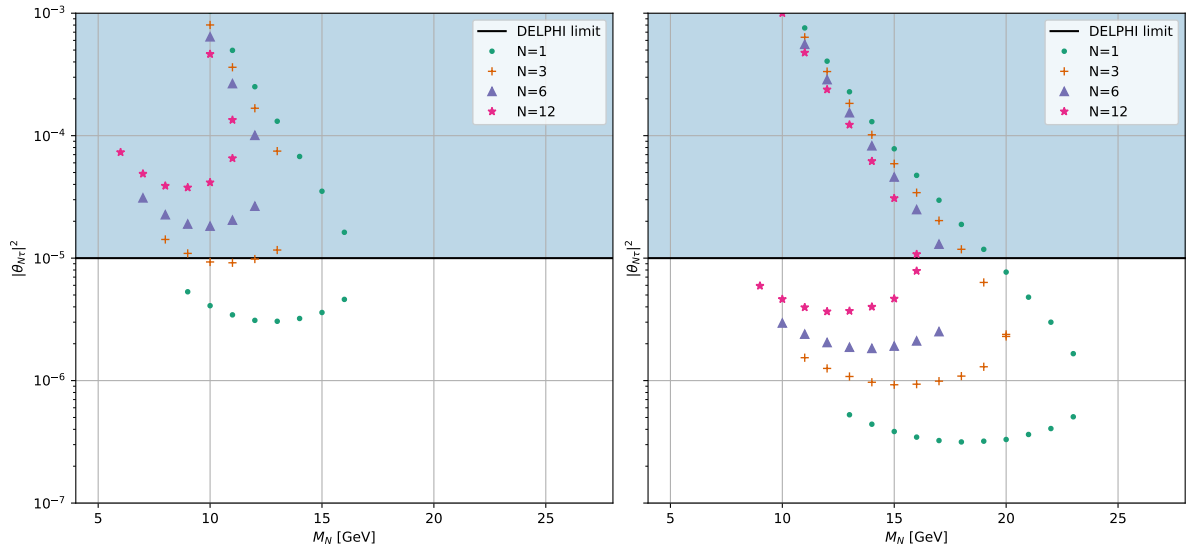
Considering the $N = 3$ sensitivity curve in the top right panel of Fig. 8.13, and interpreting it as a 95% CL exclusion bound, as per the discussion above, this shows the potential to improve the sensitivity to HNLs coupled to τ flavour by up to an order of magnitude compared to the DELPHI limit.

Parameter exploration

$d_{\max} = 30 \text{ mm}$



$d_{\max} = 50 \text{ mm}$



$d_{\max} = 100 \text{ mm}$

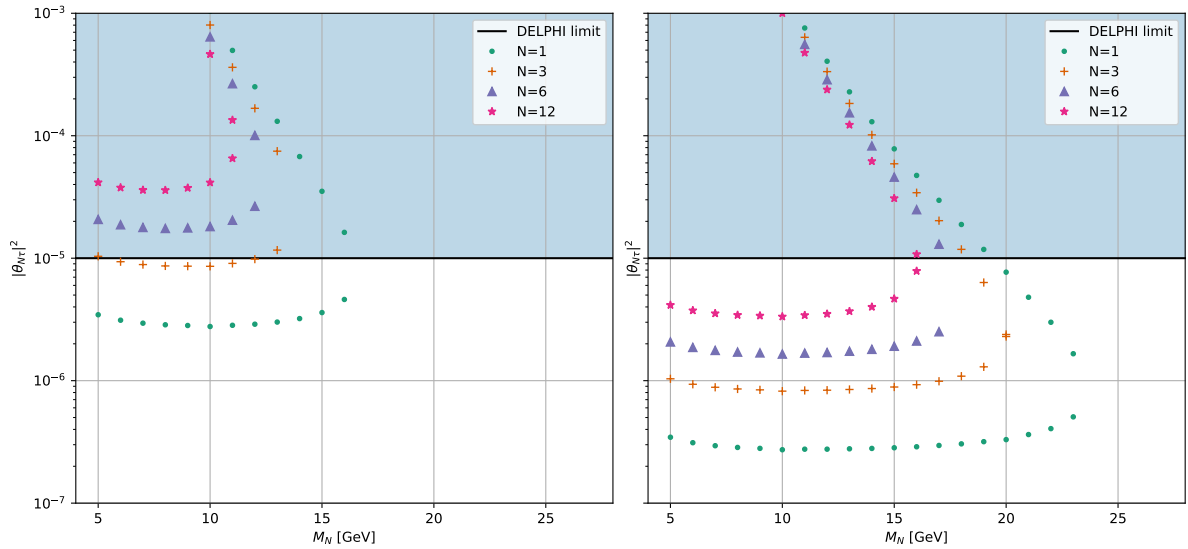


Figure 8.13.: Parameter exploration of displaced ($d_{\min} = 1 \text{ mm}$) sensitivity estimates for integrated luminosities $\mathcal{L} = 300 \text{ fb}^{-1}$ and $\mathcal{L} = 3000 \text{ fb}^{-1}$, varying d_{\max} and the number of events required.

Parameter exploration var. d_{min}

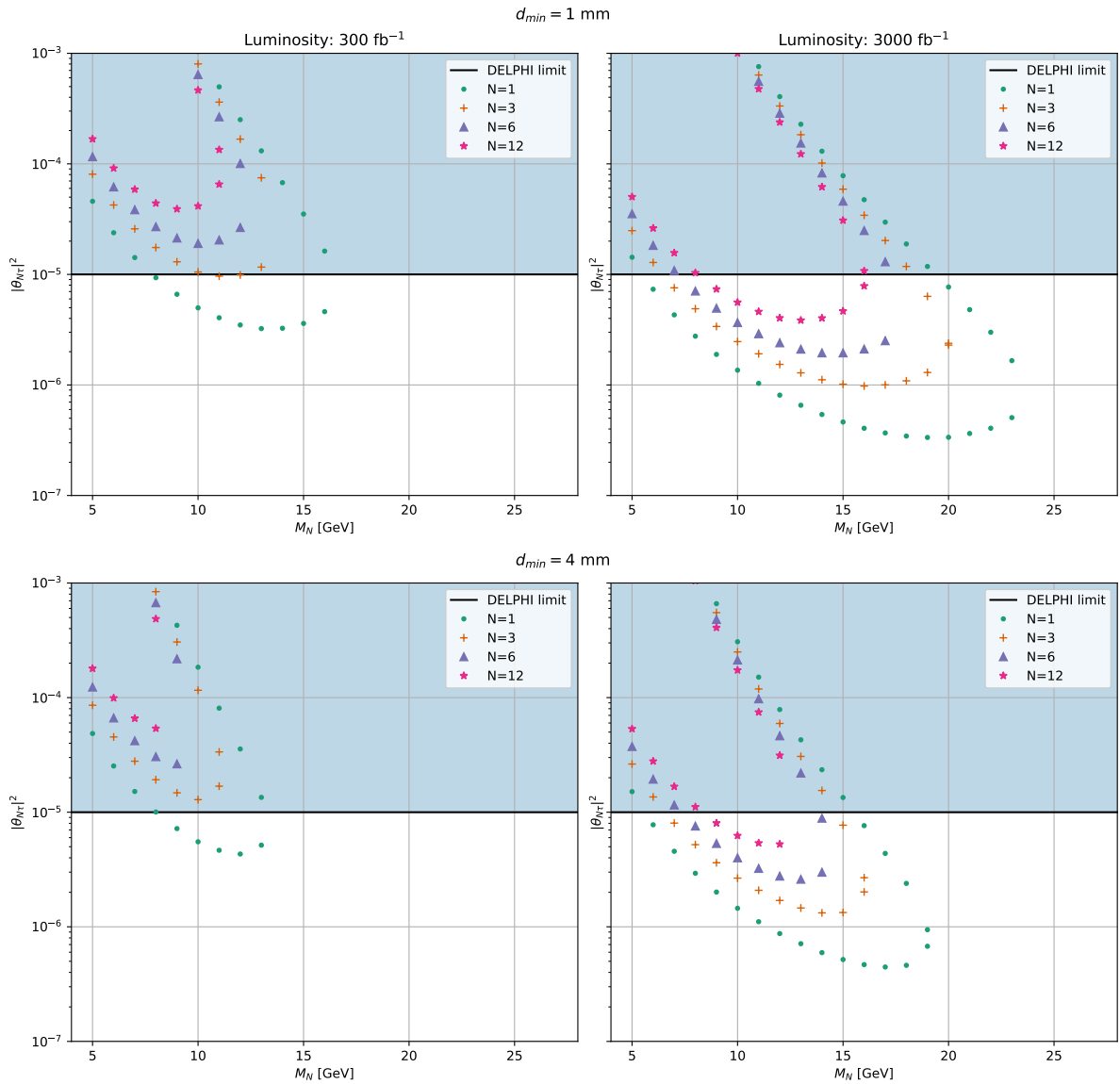


Figure 8.14.: Parameter exploration of displaced ($d_{max} = 30$ mm) sensitivity estimates for integrated luminosities $\mathcal{L} = 300 \text{ fb}^{-1}$ and $\mathcal{L} = 3000 \text{ fb}^{-1}$, varying d_{min} and the number of events required.

Conclusion

The Large Hadron Collider is colloquially referred to as a ‘hadron machine’, given the fact that colliding protons are strongly interacting particles. Nevertheless, LHC is also a powerful ‘weak boson factory’, having as of this point in time produced more than a billion W bosons. This makes LHC, among other things, a perfect place to explore neutrino-related extensions of the Standard Model, as such particles possess weak or weak-like interactions.

The most notable example of such an extension of the Standard Model is that of *heavy neutral leptons*. Introduced around the dawn of the Standard Model, they persist to this day today, some 50+ years later (see e.g. the recent contribution to the Snowmass report [55]) as hypothetical particles, which are able to resolve one or even several beyond-the-Standard-Model phenomena [102]. From a phenomenological point of view HNLs are just neutral massive particles, interacting via weak-like interactions, albeit suppressed by the flavour mixing angles. Searches for HNLs have become a part of every major particle physics experiment in CERN and elsewhere. The results of the negative searches are presented in the ‘mass vs. mixing angle’ parameter space, as Figures 4.3a–4.3c demonstrate. For masses above a few GeV the limits for HNLs mixed with tau flavour are still those from the early 1990s, coming from the DELPHI experiment at LEP1. In particular, the LHC searches for such HNLs were deemed infeasible due to low efficiency of detecting tau-leptons as compared to that for electrons and/or muons (see e.g. another recent NBI thesis [103]).

In this work we demonstrate that the stagnation on this front can be improved if one uses tau triggers, developed with the Higgs boson searches in mind [104]. Such tau-triggers are tuned to efficiently identify hadronically decaying tau-leptons or tau-lepton pairs. We, therefore, develop a search strategy for the following chain of processes:

$$\underbrace{p + p \rightarrow \tau_{\text{had}}^{\pm} + N + j}_{\text{production}} \quad \text{with subsequent} \quad \underbrace{N \rightarrow \tau_{\text{had}}^{\pm} + \ell^{\mp} + \nu_{\ell}}_{\text{decay}}, \quad (9.0.1)$$

where the subscript τ_{had} indicates that τ 's are decaying hadronically, and j denotes one or several QCD jets. An important fact here is that this process can be governed by only a single HNL mixing, $|\theta_{N\tau}|^2 \neq 0$. The presence of the jets is an important factor in allowing the primary τ -lepton to pass the p_T cut of the tau-triggers, and so the presence of at least one jet improves the detector efficiency by almost a factor of 5.

The processes with extra jets of course decrease the production cross-section, but this decrease is somewhat compensated for by the boost in τ 's p_T .

We then demonstrated that the topological trigger option on the τ -trigger menu on its own can achieve a useful level of efficiency, for the case of two τ leptons (with $p_T^{(\tau_1)} \geq 40$ GeV for the primary and $p_T^{(\tau_2)} \geq 30$ GeV for the secondary τ -lepton and with the separation $\Delta R \leq 2.6$ between the two. In the remaining items on the τ -trigger menu lies a potential for further increasing this efficiency, if the simulated jet information is processed explicitly.

Originally the two-tau triggers were designed with the prompt τ -leptons in mind. We, however, propose to use them for both prompt and displaced searches. For the displaced searches we adopt the minimal displacement distance to $d_{\min} \geq 1$ mm. Based on the understanding that the performance of two-tau triggers degrades when there is displacement between τ 's, for our main result we limit the maximal displacement to be $d_{\max} \leq 30$ mm, much smaller than the maximal possible displacement of 300 mm, used in other ATLAS HNL searches [88]. However, we also explore how our results depend on both d_{\min} and d_{\max} . As expected, the number of events for displaced searches grows proportionally to the maximal distance. This warrants exploration of the efficiency of the tau-triggers for the case when two τ 's are displaced. We expect that the displacement cut on the HNL together with the requirement of same sign τ -leptons will greatly reduce SM background. Recent studies by the ATLAS collaboration [72] indeed support this assumption. The detailed background investigation remains for the future studies.

We also perform the analysis for prompt HNL searches, the case when a primary and a secondary τ -vertex is separate by less than 1 mm. In this case the assumption of zero background is more dubious. To this end, along with single event sensitivity we estimated sensitivity towards the detection of 3, ... 12 events. Our main results demonstrate that each of the two cases (prompt and displaced searches) have a potential to go beyond the current limits by at least a few factors. In the best case (displaced vertices with zero SM background and efficiency of tau-triggers unchanged up to $d_{\max} = 30$ mm), one can expect more than an order of magnitude improvement in the mass range $5 \text{ GeV} \leq M_N \leq 20 \text{ GeV}$ for the luminosity $\mathcal{L} = 3000 \text{ fb}^{-1}$. Similarly for the prompt case one can get a single event sensitivity better than previous bounds for masses $10 \text{ GeV} \leq M_N \leq 50 \text{ GeV}$.

To summarise: While it is indeed true that the detection of τ leptons at LHC is very indirect, unlike the electrons and muons, the efficiency of the existing tau-triggers can help to obtain sensitivity, comparable to that of other tri-lepton searches [88, 72]. This thesis demonstrates that a single event sensitivity may reach far beyond

current experimental limits. Even sensitivity estimates where 3 events are required, which in the context of this thesis, is the best proxy for a 95% CL exclusion limit when no background is assumed, has the potential to improve the current bound by an order of magnitude. This is most relevant in the displaced case, since the background assumption is far more reasonable here. Though a lot of important details have been deliberately skipped when doing this work, our results do suggest that it would make sense to process our Monte Carlo generated data through the whole ATLAS pipeline and, if successful, to run analysis on the actual data. This work is, of course, beyond this thesis.

As with any scientific work, the process of this thesis has been marked with a lot of diverging ideas, rabbit holes and dead ends. And, as is almost always the case, hindsight is 20/20 vision, or at least clearer, and so in this final section, we wish to provide a list of ideas and reflections on any further work along the vein of this thesis:

1. As our signal contains both jets and hadronically decaying taus, one should impose jet isolation criteria, making sure that decay products of τ 's do not end up in the vicinity of jets. Imposing this criteria would reduce the sensitivity, but knowing by how much requires doing the analysis. This would require employing software to extract the jet properties from the HEPMC files.
2. Utilise the remaining tau trigger conditions, which all include cuts on hard jets. As with the above point, this requires mastery of the simulated jet information, but would most likely result in an increased sensitivity.
3. Displacement cuts were implemented purely radially in this thesis. They should be re-done by properly defining longitudinal and transverse impact parameters and defining displacement as in [88, 72].
4. When doing displacement analysis, using the average Lorentz factor to calculate sensitivities will generate sizeable errors in determining the upper branch of the sensitivity curve [96]. This should instead be done event by event for a more accurate result.
5. One can try to look at leptonically decaying taus as well, similar to the spirit of the thesis [103].
6. Conducting a background analysis would be beneficial to better examine the prospects of prompt searches. Besides, a thorough background analysis becomes increasingly important for displaced searches as the instantaneous luminosity goes up.

7. It would also be interesting to examine the possibility of using Machine Learning to reconstruct the value of M_N based on event kinematics. This holds the potential to move broaden the search from being focused only on detecting a certain particle signature, e.g. a tri-lepton signature, to also include the possibility of measuring M_N .

Bibliography

- [1] *Standard Model Summary Plots June 2021*. Tech. rep. All figures including auxiliary figures are available at <https://atlas.web.cern.ch/Atlas/GROUPS/PHYSICS/PUBNOTES/ATLAS-CONF-2021-032>. Geneva: CERN, July 2021.
- [2] Luca Clissa. *Survey of Big Data sizes in 2021*. 2022.
- [3] Maria Girone. „Big data analytics and the LHC“. In: (2016). *CF ’16 Proceedings of the ACM International Conference on Computing Frontiers*. ISBN: 978-1-4503-4128-8.
- [4] T. Aaltonen *et al.* „High-precision measurement of the W boson mass with the CDF II detector“. In: *Science* 376.6589 (2022), pp. 170–176.
- [5] Georges Aad *et al.* „Observation of a new particle in the search for the Standard Model Higgs boson with the ATLAS detector at the LHC“. In: *Phys. Lett. B* 716 (2012), pp. 1–29. arXiv: 1207.7214 [hep-ex].
- [6] Serguei Chatrchyan *et al.* „Observation of a New Boson at a Mass of 125 GeV with the CMS Experiment at the LHC“. In: *Phys. Lett. B* 716 (2012), pp. 30–61. arXiv: 1207.7235 [hep-ex].
- [7] S. F. Novaes. „Standard model: An Introduction“. In: *10th Jorge Andre Swieca Summer School: Particle and Fields*. Jan. 1999, pp. 5–102. arXiv: hep-ph/0001283.
- [8] P. A. Zyla *et al.* „Review of Particle Physics“. In: *PTEP* 2020.8 (2020), p. 083C01.
- [9] H. David Politzer. „Reliable Perturbative Results for Strong Interactions?“ In: *Phys. Rev. Lett.* 30 (1973). Ed. by J. C. Taylor, pp. 1346–1349.
- [10] David J. Gross and Frank Wilczek. „Ultraviolet Behavior of Nonabelian Gauge Theories“. In: *Phys. Rev. Lett.* 30 (1973). Ed. by J. C. Taylor, pp. 1343–1346.
- [11] S. L. Glashow. „Partial Symmetries of Weak Interactions“. In: *Nucl. Phys.* 22 (1961), pp. 579–588.
- [12] Steven Weinberg. „A Model of Leptons“. In: *Phys. Rev. Lett.* 19 (1967), pp. 1264–1266.
- [13] Abdus Salam. „Weak and Electromagnetic Interactions“. In: *Conf. Proc. C* 680519 (1968), pp. 367–377.

- [14] Peter W. Higgs. „Broken Symmetries and the Masses of Gauge Bosons“. In: *Phys. Rev. Lett.* 13 (1964). Ed. by J. C. Taylor, pp. 508–509.
- [15] F. Englert and R. Brout. „Broken Symmetry and the Mass of Gauge Vector Mesons“. In: *Phys. Rev. Lett.* 13 (1964). Ed. by J. C. Taylor, pp. 321–323.
- [16] C. Dohmen *et al.* „Test of lepton flavor conservation in $\mu \rightarrow e$ conversion on titanium“. In: *Phys. Lett. B* 317 (1993), pp. 631–636.
- [17] Manuel Meucci. „MEG II experiment status and prospect“. In: (Jan. 2022). arXiv: 2201.08200 [hep-ex].
- [18] Aji Daniel. „The $\mu 2e$ experiment at Fermilab“. In: *PoS HQL2016* (2017), p. 019.
- [19] Vardan Khachatryan *et al.* „Search for Lepton-Flavour-Violating Decays of the Higgs Boson“. In: *Phys. Lett. B* 749 (2015), pp. 337–362. arXiv: 1502.07400 [hep-ex].
- [20] Georges Aad *et al.* „Search for lepton-flavour-violating $H \rightarrow \mu\tau$ decays of the Higgs boson with the ATLAS detector“. In: *JHEP* 11 (2015), p. 211. arXiv: 1508.03372 [hep-ex].
- [21] Georges Aad *et al.* „Search for the lepton flavor violating decay $Z \rightarrow e\mu$ in pp collisions at \sqrt{s} TeV with the ATLAS detector“. In: *Phys. Rev. D* 90.7 (2014), p. 072010. arXiv: 1408.5774 [hep-ex].
- [22] Georges Aad *et al.* „Search for charged-lepton-flavour violation in Z -boson decays with the ATLAS detector“. In: *Nature Phys.* 17.7 (2021), p. 819. arXiv: 2010.02566 [hep-ex].
- [23] Sheldon L. Glashow and Steven Weinberg. „Natural Conservation Laws for Neutral Currents“. In: *Phys. Rev. D* 15 (1977), p. 1958.
- [24] Michelle J. Dolinski, Alan W. P. Poon, and Werner Rodejohann. „Neutrinoless Double-Beta Decay: Status and Prospects“. In: *Ann. Rev. Nucl. Part. Sci.* 69 (2019), pp. 219–251. arXiv: 1902.04097 [nucl-ex].
- [25] B. Pontecorvo. „Inverse beta processes and nonconservation of lepton charge“. In: *Zh. Eksp. Teor. Fiz.* 34 (1957), p. 247.
- [26] Frederick Reines and Clyde L. Cowan. „The neutrino“. In: *Nature* 178 (1956), pp. 446–449.
- [27] G. Danby, J. M. Gaillard, Konstantin A. Goulianos, L. M. Lederman, Nari B. Mistry, M. Schwartz, and J. Steinberger. „Observation of High-Energy Neutrino Reactions and the Existence of Two Kinds of Neutrinos“. In: *Phys. Rev. Lett.* 9 (1962), pp. 36–44.

- [28] Samoil M. Bilenky. „Neutrino oscillations: brief history and present status“. In: *22nd International Baldin Seminar on High Energy Physics Problems: Relativistic Nuclear Physics and Quantum Chromodynamics*. Aug. 2014. arXiv: 1408.2864 [hep-ph].
- [29] Ivan Esteban, M. C. Gonzalez-Garcia, Michele Maltoni, Thomas Schwetz, and Albert Zhou. „The fate of hints: updated global analysis of three-flavor neutrino oscillations“. In: *JHEP* 09 (2020), p. 178. arXiv: 2007.14792 [hep-ph].
- [30] European Space Agency (ESA). *The cosmic budget of 'ordinary' matter*. <https://sci.esa.int/web/xmm-newton/-/60430-the-cosmic-budget-of-ordinary-matter>. June 2018.
- [31] Jaco de Swart, Gianfranco Bertone, and Jeroen van Dongen. „How Dark Matter Came to Matter“. In: *Nature Astron.* 1 (2017), p. 0059. arXiv: 1703.00013 [astro-ph.CO].
- [32] P. A. R. Ade *et al.* „Planck 2015 results. XIII. Cosmological parameters“. In: *Astron. Astrophys.* 594 (2016), A13. arXiv: 1502.01589 [astro-ph.CO].
- [33] A. D. Sakharov. „Violation of CP Invariance, C asymmetry, and baryon asymmetry of the universe“. In: *Pisma Zh. Eksp. Teor. Fiz.* 5 (1967), pp. 32–35.
- [34] Laurent Canetti, Marco Drewes, and Mikhail Shaposhnikov. „Matter and Antimatter in the Universe“. In: *New J. Phys.* 14 (2012), p. 095012. arXiv: 1204.4186 [hep-ph].
- [35] Mark Thomson. *Modern Particle Physics*. English. 1st edition. Cambridge, United Kingdom ; New York: Cambridge University Press, Sept. 2013.
- [36] K. Kajantie, M. Laine, K. Rummukainen, and Mikhail E. Shaposhnikov. „The Electroweak phase transition: A Nonperturbative analysis“. In: *Nucl. Phys. B* 466 (1996), pp. 189–258. arXiv: hep-lat/9510020.
- [37] Matthew D. Schwartz. *Quantum Field Theory and the Standard Model*. English. 1st edition. New York: Cambridge University Press, Dec. 2013.
- [38] Julien Lesgourgues, Gianpiero Mangano, Gennaro Miele, and Sergio Pastor. *Neutrino Cosmology*. Cambridge: Cambridge University Press, 2013.
- [39] Steven Weinberg. „Baryon and Lepton Nonconserving Processes“. In: *Phys. Rev. Lett.* 43 (1979), pp. 1566–1570.
- [40] G. Anamiati, Oscar Castillo-Felisola, Renato M. Fonseca, J. C. Helo, and M. Hirsch. „High-dimensional neutrino masses“. In: *JHEP* 12 (2018), p. 066. arXiv: 1806.07264 [hep-ph].
- [41] Prateek Agrawal, Martin Bauer, James Beacham, *et al.* „Feebly-Interacting Particles:FIPs 2020 Workshop Report“. In: *arXiv:2102.12143 [hep-ph]* (Feb. 2021). arXiv: 2102.12143.

- [42] Jean-Loup Tastet, Oleg Ruchayskiy, and Inar Timiryasov. „Reinterpreting the ATLAS bounds on heavy neutral leptons in a realistic neutrino oscillation model“. In: (July 2021). [_eprint: 2107.12980](#).
- [43] Jean-Loup Tastet. „Searching for Heavy Neutral Leptons at CERN“. English. PhD. Niels Bohr Institute, Feb. 2021.
- [44] Marcin Chrzaszcz, Marco Drewes, Tomás E. Gonzalo, Julia Harz, Suraj Krishnamurthy, and Christoph Weniger. „A frequentist analysis of three right-handed neutrinos with GAMBIT“. In: *Eur. Phys. J. C* 80.6 (2020), p. 569. [arXiv: 1908.02302 \[hep-ph\]](#).
- [45] Anupama Atre, Tao Han, Silvia Pascoli, and Bin Zhang. „The Search for Heavy Majorana Neutrinos“. In: *JHEP* 05 (2009), p. 030. [arXiv: 0901.3589 \[hep-ph\]](#).
- [46] Kyrylo Bondarenko, Alexey Boyarsky, Dmitry Gorbunov, and Oleg Ruchayskiy. „Phenomenology of GeV-scale Heavy Neutral Leptons“. In: *JHEP* 11 (2018), p. 032. [arXiv: 1805.08567 \[hep-ph\]](#).
- [47] P. Abreu *et al.* „Searches for heavy neutrinos from Z decays“. In: *Phys. Lett. B* 274 (1992), pp. 230–238.
- [48] Matthias Komm. „Heavy neutral lepton searches at the LHC“. In: *PoS LHCP2021* (2021), p. 001.
- [49] Robert E. Shrock. „General Theory of Weak Leptonic and Semileptonic Decays. 1. Leptonic Pseudoscalar Meson Decays, with Associated Tests For, and Bounds on, Neutrino Masses and Lepton Mixing“. In: *Phys. Rev. D* 24 (1981), p. 1232.
- [50] R. E. Shrock. „New Tests For, and Bounds On, Neutrino Masses and Lepton Mixing“. In: *Phys. Lett. B* 96 (1980), pp. 159–164.
- [51] Robert E. Shrock. „General Theory of Weak Processes Involving Neutrinos. 2. Pure Leptonic Decays“. In: *Phys. Rev. D* 24 (1981), p. 1275.
- [52] Michael Gronau, Chung Ngoc Leung, and Jonathan L. Rosner. „Extending Limits on Neutral Heavy Leptons“. In: *Phys. Rev. D* 29 (1984), p. 2539.
- [53] W. Buchmuller and C. Greub. „Heavy Majorana neutrinos in electron - positron and electron - proton collisions“. In: *Nucl. Phys. B* 363 (1991), pp. 345–368.
- [54] Dmitry Gorbunov and Mikhail Shaposhnikov. „How to find neutral leptons of the ν MSM?“ In: *JHEP* 10 (2007). [Erratum: *JHEP* 11, 101 (2013)], p. 015. [arXiv: 0705.1729 \[hep-ph\]](#).
- [55] Asli M. Abdullahi *et al.* „The Present and Future Status of Heavy Neutral Leptons“. In: *2022 Snowmass Summer Study*. Mar. 2022. [arXiv: 2203.08039 \[hep-ph\]](#).

- [56] Georges Aad *et al.* „Inclusive search for same-sign dilepton signatures in pp collisions at $\sqrt{s} = 7$ TeV with the ATLAS detector“. In: *JHEP* 10 (2011), p. 107. arXiv: 1108.0366 [hep-ex].
- [57] Georges Aad *et al.* „Search for heavy neutrinos and right-handed W bosons in events with two leptons and jets in pp collisions at $\sqrt{s} = 7$ TeV with the ATLAS detector“. In: *Eur. Phys. J. C* 72 (2012), p. 2056. arXiv: 1203.5420 [hep-ex].
- [58] Serguei Chatrchyan *et al.* „Search for heavy Majorana Neutrinos in $\mu^\pm\mu^\pm +$ Jets and $e^\pm e^\pm +$ Jets Events in pp Collisions at $\sqrt{s} = 7$ TeV“. In: *Phys. Lett. B* 717 (2012), pp. 109–128. arXiv: 1207.6079 [hep-ex].
- [59] D. Liventsev *et al.* „Search for heavy neutrinos at Belle“. In: *Phys. Rev. D* 87.7 (2013). [Erratum: *Phys.Rev.D* 95, 099903 (2017)], p. 071102. arXiv: 1301.1105 [hep-ex].
- [60] Roel Aaij *et al.* „Search for Majorana neutrinos in $B^- \rightarrow \pi^+ \mu^- \mu^-$ decays“. In: *Phys. Rev. Lett.* 112.13 (2014), p. 131802. arXiv: 1401.5361 [hep-ex].
- [61] Georges Aad *et al.* „Search for heavy Majorana neutrinos with the ATLAS detector in pp collisions at $\sqrt{s} = 8$ TeV“. In: *JHEP* 07 (2015), p. 162. arXiv: 1506.06020 [hep-ex].
- [62] Vardan Khachatryan *et al.* „Search for heavy Majorana neutrinos in $\mu^\pm\mu^\pm +$ jets events in proton-proton collisions at $\sqrt{s} = 8$ TeV“. In: *Phys. Lett. B* 748 (2015), pp. 144–166. arXiv: 1501.05566 [hep-ex].
- [63] Vardan Khachatryan *et al.* „Search for heavy Majorana neutrinos in $e^s e^s +$ jets and $e^s \mu^s +$ jets events in proton-proton collisions at $\sqrt{s} = 8$ TeV“. In: *JHEP* 04 (2016), p. 169. arXiv: 1603.02248 [hep-ex].
- [64] Vladimir V. Gligorov, Simon Knapen, Michele Papucci, and Dean J. Robinson. „Searching for Long-lived Particles: A Compact Detector for Exotics at LHCb“. In: *Phys. Rev. D* 97.1 (2018), p. 015023. arXiv: 1708.09395 [hep-ph].
- [65] A. Izmaylov and S. Suvorov. „Search for heavy neutrinos in the ND280 near detector of the T2K experiment“. In: *Phys. Part. Nucl.* 48.6 (2017), pp. 984–986.
- [66] Eduardo Cortina Gil *et al.* „Search for heavy neutral lepton production in K^+ decays“. In: *Phys. Lett. B* 778 (2018), pp. 137–145. arXiv: 1712.00297 [hep-ex].
- [67] Albert M Sirunyan *et al.* „Search for heavy Majorana neutrinos in same-sign dilepton channels in proton-proton collisions at $\sqrt{s} = 13$ TeV“. In: *JHEP* 01 (2019), p. 122. arXiv: 1806.10905 [hep-ex].
- [68] Albert M Sirunyan *et al.* „Search for heavy neutral leptons in events with three charged leptons in proton-proton collisions at $\sqrt{s} = 13$ TeV“. In: *Phys. Rev. Lett.* 120.22 (2018), p. 221801. arXiv: 1802.02965 [hep-ex].

- [69] Morad Aaboud *et al.* „Search for heavy Majorana or Dirac neutrinos and right-handed W gauge bosons in final states with two charged leptons and two jets at $\sqrt{s} = 13$ TeV with the ATLAS detector“. In: *JHEP* 01 (2019), p. 016. arXiv: 1809.11105 [hep-ex].
- [70] Georges Aad *et al.* „Search for heavy neutral leptons in decays of W bosons produced in 13 TeV pp collisions using prompt and displaced signatures with the ATLAS detector“. In: *JHEP* 10 (2019), p. 265. arXiv: 1905.09787 [hep-ex].
- [71] Eduardo Cortina Gil *et al.* „Search for K^+ decays to a muon and invisible particles“. In: *Phys. Lett. B* 816 (2021), p. 136259. arXiv: 2101.12304 [hep-ex].
- [72] „Search for heavy neutral leptons in decays of W bosons using a dilepton displaced vertex in $\sqrt{s} = 13$ TeV pp collisions with the ATLAS detector“. In: (Apr. 2022). arXiv: 2204.11988 [hep-ex].
- [73] SHiP Collaboration. „Sensitivity of the SHiP experiment to Heavy Neutral Leptons“. In: *arXiv:1811.00930 [hep-ex, physics:hep-ph]* (Apr. 2019). arXiv: 1811.00930.
- [74] J. T. Boyd. *LHC Run-2 and Future Prospects*. Jan. 2020. arXiv: 2001.04370 [hep-ex].
- [75] *Luminosity determination in pp collisions at $\sqrt{s}=13$ TeV using the ATLAS detector at the LHC*. en. Tech. rep. ATLAS-CONF-2019-021. Publication Title: CERN Document Server. ATLAS-COM-CONF-2019-036, June 2019.
- [76] The ATLAS Collaboration, G. Aad, E. Abat, *et al.* „The ATLAS Experiment at the CERN Large Hadron Collider“. en. In: *Journal of Instrumentation* 3.08 (Aug. 2008). Publisher: IOP Publishing, S08003–S08003.
- [77] Joao Pequeno and Paul Schaffner. „How ATLAS detects particles: diagram of particle paths in the detector“. Jan. 2013.
- [78] Matthew D. Schwartz. „TASI Lectures on Collider Physics“. In: *arXiv:1709.04533 [hep-ph]* (Sept. 2017). arXiv: 1709.04533.
- [79] The ATLAS Collaboration. „The ATLAS Tau Trigger in Run 2“. In: *CERN Conference note* (July 2017).
- [80] The ATLAS Collaboration. „Performance of the ATLAS Trigger System in 2010“. In: *The European Physical Journal C* 72.1 (Jan. 2012). arXiv: 1110.1530, p. 1849.
- [81] Particle Data Group, P A Zyla, R M Barnett, *et al.* „Review of Particle Physics“. In: *Progress of Theoretical and Experimental Physics* 2020.8 (Aug. 2020), p. 083C01.
- [82] ATLAS Collaboration. „Measurements of the W production cross sections in association with jets with the ATLAS detector“. In: *The European Physical Journal C* 75.2 (Feb. 2015). arXiv: 1409.8639, p. 82.

- [83] Celine Degrande, Olivier Mattelaer, Richard Ruiz, and Jessica Turner. „Fully-Automated Precision Predictions for Heavy Neutrino Production Mechanisms at Hadron Colliders“. In: *Physical Review D* 94.5 (Sept. 2016). arXiv: 1602.06957, p. 053002.
- [84] Johan Alwall, Michel Herquet, Fabio Maltoni, Olivier Mattelaer, and Tim Stelzer. „MadGraph 5 : Going Beyond“. In: *JHEP* 06 (2011), p. 128. arXiv: 1106.0522 [hep-ph].
- [85] Torbjörn Sjöstrand, Stefan Ask, Jesper R. Christiansen, Richard Corke, Nishita Desai, Philip Ilten, Stephen Mrenna, Stefan Prestel, Christine O. Rasmussen, and Peter Z. Skands. „An introduction to PYTHIA 8.2“. In: *Comput. Phys. Commun.* 191 (2015), pp. 159–177. arXiv: 1410.3012 [hep-ph].
- [86] Enrico Bothmann *et al.* „Event Generation with Sherpa 2.2“. In: *SciPost Phys.* 7.3 (2019), p. 034. arXiv: 1905.09127 [hep-ph].
- [87] Christian Bierlich, Smita Chakraborty, Nishita Desai, *et al.* *A comprehensive guide to the physics and usage of PYTHIA 8.3*. Tech. rep. arXiv:2203.11601. arXiv:2203.11601 [hep-ex, physics:hep-ph] type: article. arXiv, Mar. 2022.
- [88] ATLAS Collaboration. „Search for heavy neutral leptons in decays of W bosons produced in 13 TeV pp collisions using prompt and displaced signatures with the ATLAS detector“. In: *Journal of High Energy Physics* 2019.10 (Oct. 2019). arXiv: 1905.09787, p. 265.
- [89] CMS Collaboration. „Search for heavy neutral leptons in events with three charged leptons in proton-proton collisions at $\sqrt{s} = 13$ TeV“. In: *Physical Review Letters* 120.22 (May 2018). arXiv: 1802.02965, p. 221801.
- [90] CMS Collaboration. „Search for long-lived heavy neutral leptons with displaced vertices in proton-proton collisions at $\sqrt{s} = 13$ TeV“. In: *arXiv:2201.05578 [hep-ex]* (Jan. 2022). arXiv: 2201.05578.
- [91] J. Alwall, R. Frederix, S. Frixione, V. Hirschi, F. Maltoni, O. Mattelaer, H.-S. Shao, T. Stelzer, P. Torrielli, and M. Zaro. „The automated computation of tree-level and next-to-leading order differential cross sections, and their matching to parton shower simulations“. In: *Journal of High Energy Physics* 2014.7 (July 2014). arXiv: 1405.0301, p. 79.
- [92] Daniel Alva, Tao Han, and Richard Ruiz. „Heavy Majorana Neutrinos from $W\gamma$ Fusion at Hadron Colliders“. In: *Journal of High Energy Physics* 2015.2 (Feb. 2015). arXiv: 1411.7305, p. 72.
- [93] L. Garren, I. G. Knowles, T. Sjöstrand, and T. Trippe. „Monte carlo particle numbering scheme“. en. In: *The European Physical Journal C - Particles and Fields* 15.1 (Mar. 2000), pp. 205–207.

- [94] Kyrylo Bondarenko, Alexey Boyarsky, Dmitry Gorbunov, and Oleg Ruchayskiy. „Phenomenology of GeV-scale Heavy Neutral Leptons“. en. In: (May 2018).
- [95] Michael E. Peskin and Daniel V. Schroeder. *An Introduction To Quantum Field Theory*. English. 1st edition. CRC Press, Sept. 2019.
- [96] Kyrylo Bondarenko, Alexey Boyarsky, Maksym Ovchynnikov, and Oleg Ruchayskiy. „Sensitivity of the intensity frontier experiments for neutrino and scalar portals: analytic estimates“. In: *JHEP* 08 (2019). _eprint: 1902.06240, p. 061.
- [97] Philip Ilten. „Tau Decays in Pythia 8“. In: *Nuclear Physics B - Proceedings Supplements* 253-255 (Aug. 2014). arXiv: 1211.6730, pp. 77–80.
- [98] ATLAS Collaboration. „Identification and energy calibration of hadronically decaying tau leptons with the ATLAS experiment in $\sqrt{s}=8$ TeV“. In: *arXiv:1412.7086 [hep-ex]* (July 2015). arXiv: 1412.7086.
- [99] Fabian A.J. Thiele. „An ATLAS Search for Sterile Neutrinos“. English. PhD. Copenhagen: University of Copenhagen, Oct. 2019.
- [100] I. Zurbano Fernandez *et al.* „High-Luminosity Large Hadron Collider (HL-LHC): Technical design report“. In: 10/2020 (Dec. 2020). Ed. by I. Béjar Alonso, O. Brüning, P. Fessia, L. Rossi, L. Tavian, and M. Zerlauth.
- [101] R. J. Barlow. *Statistics: A Guide to the Use of Statistical Methods in the Physical Sciences*. English. Chichester, England ; New York: Wiley, Nov. 1993.
- [102] Alexey Boyarsky, Oleg Ruchayskiy, and Mikhail Shaposhnikov. „The role of sterile neutrinos in cosmology and astrophysics“. In: *Annual Review of Nuclear and Particle Science* 59.1 (Nov. 2009). arXiv: 0901.0011 version: 2, pp. 191–214.
- [103] Arnau Morancho Tardà. „Search for prompt heavy neutral lepton decays into tau leptons with the ATLAS detector“. MA thesis. University of Copenhagen, May 2022.
- [104] *TauTriggerPublicResults < AtlasPublic < TWiki*.

Acknowledgements

Firstly, I would like to thank my supervisor, Oleg Ruchayskiy, without whom this thesis would not exist. For your encouragement, for spurring my curiosity for physics continuously, for allowing me the space to err and for not shying away from philosophising on the meaning of life and the nature of physics. Also, thank you for taking me seriously, while in the same breath teaching me to not take myself and my work all too seriously.

Secondly, Jean-Loup Tastet for all your support with MadGrpah and PYTHIA - always so willing to share your intricate knowledge on these somewhat opaque systems. For this I am extremely grateful!

Thirdly, to my office mates in the 'seesaw-playground': Arnau, Edis, Jonathan, Katinka and Mads. Thank you for our blackboard discussions, focus sessions and your company. And to my friend and long-distance 'office mate': Andy. For your help with this thesis, for our regular afternoon tea breaks, and for supplying me with a steady stream of motivational cat photos.

Finally, I would like to thank my family for all your support and encouragement throughout this process! And especially Anders, my partner. Thank you for always feeding me, for being my IT support and debugging-assistant when my own patience faltered and for your unconditional support through a very challenging process!

I am so grateful to you all!

HNL Invariant Mass Reconstructions with Varying Decay Widths

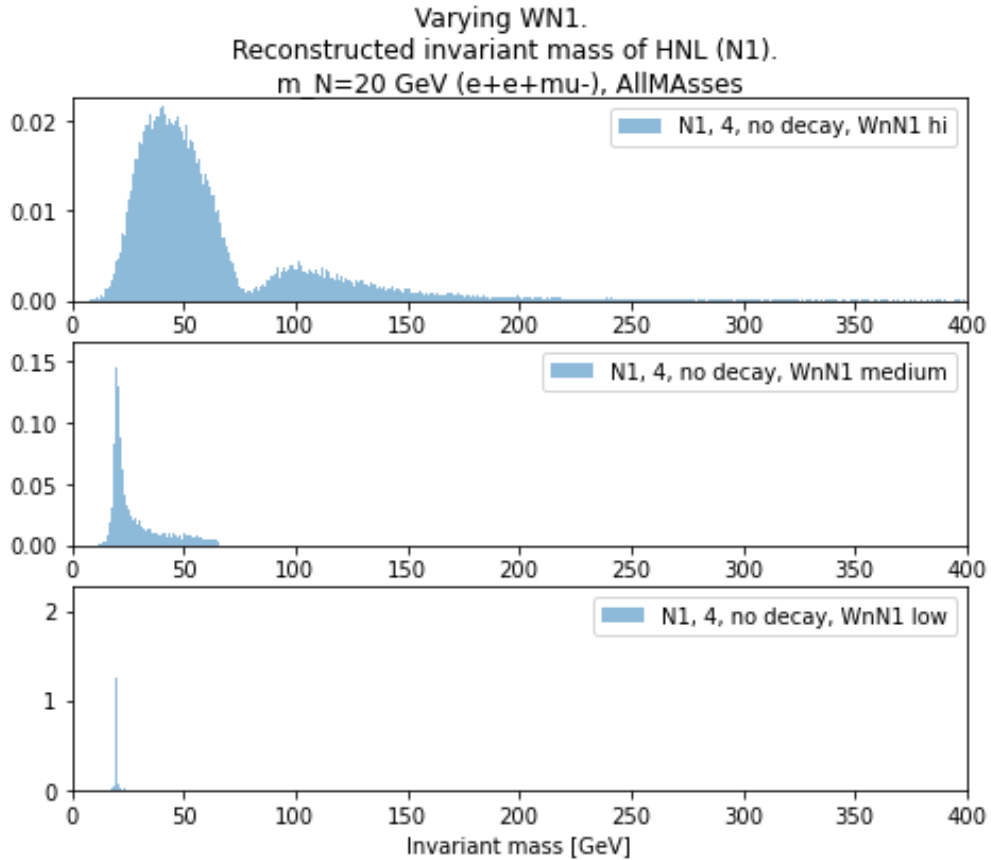


Figure A.1.: The HNL invariant mass reconstructed from its decay products, as generated by MadGraph, using the HeavyN model. The process used here has the same overall structure as the one shown in Fig.5.5, except with e^+ instead of τ^+ . Three different decay widths for the HNL were used: *Top panel* $\Gamma_N \approx \mathcal{O}(10)$ GeV, *Middle panel* $\Gamma_N \approx \mathcal{O}(1)$ GeV, *Bottom panel* $\Gamma_N \approx \mathcal{O}(10^{-1})$ GeV. This illustrates the issues arising from data generation using parameters where the Narrow Width Approximation no longer holds.

HNL Lorentz Factors

B

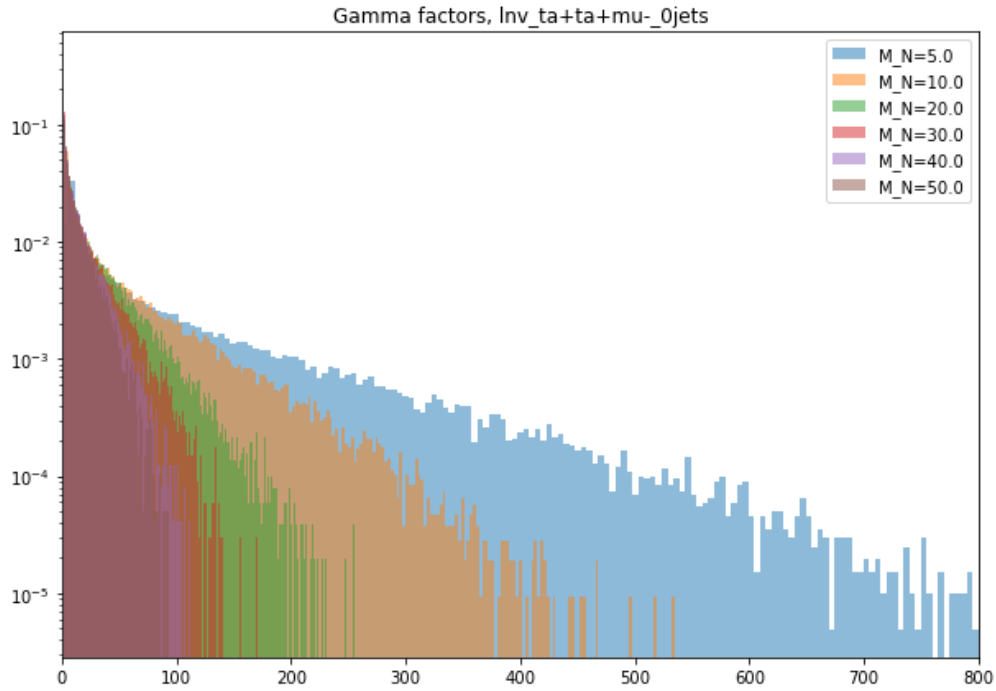


Figure B.1.: Normalised distribution of HNL Lorentz factors for the process $pp \rightarrow \tau^+\tau^+\mu^-$ with no hard jets. 40.000 events per M_N represented. The Lorentz factor runs along the x-axis.

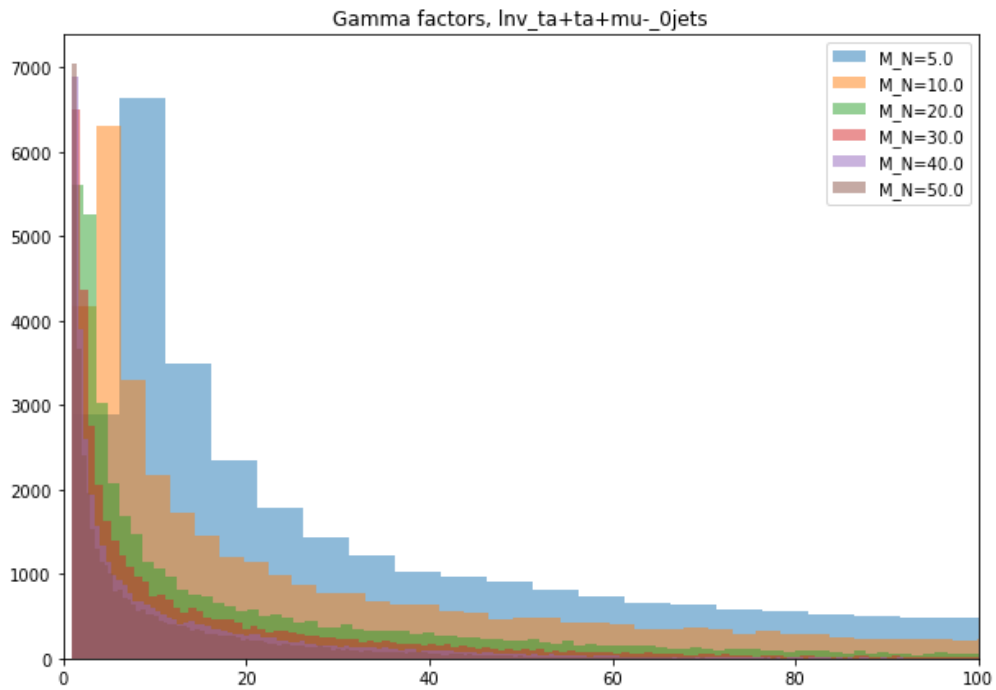
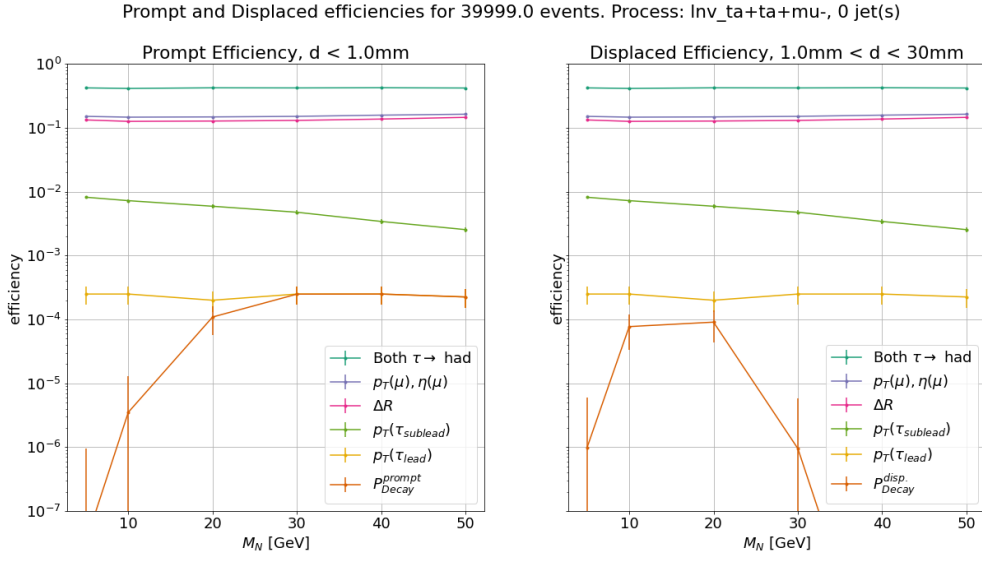


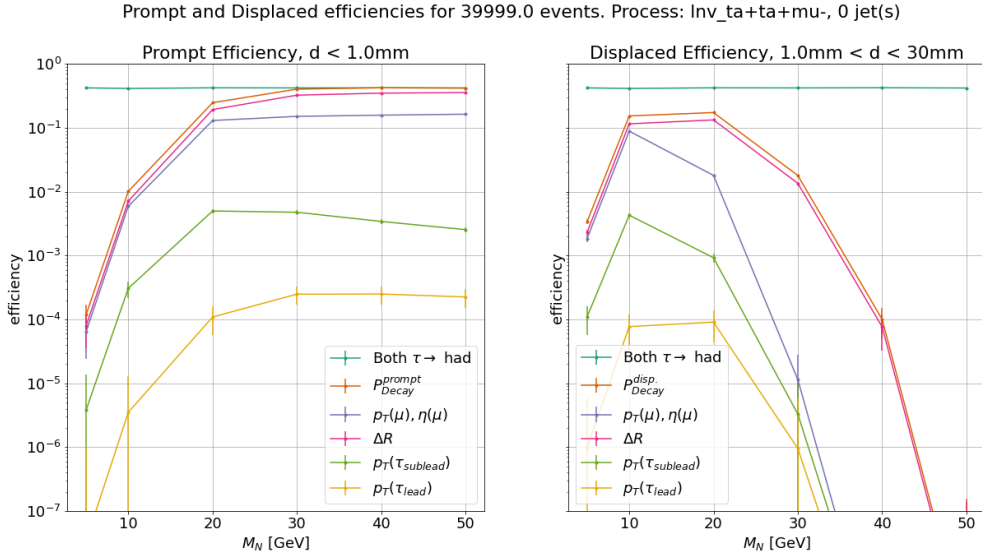
Figure B.2.: Same as Fig. B.1, but with logarithmic y-axis, to better show the tails of the distributions.

Approximation of Efficiencies after Decay

C

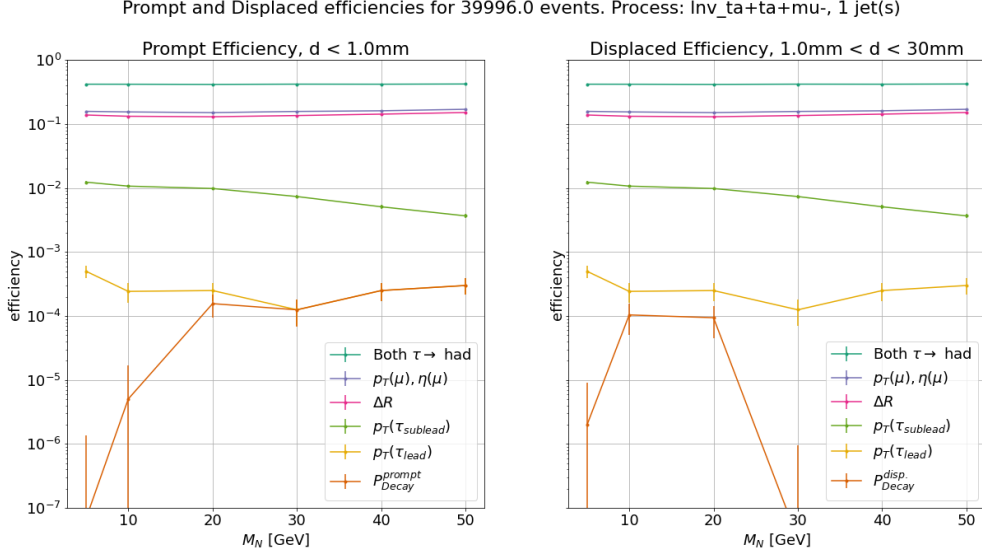


(a) Cut flow diagrams of estimated efficiencies identical to the left most panel in Fig. 8.7, with the final addition of prompt (*left*) and displaced (*right*) decay weights for each event passing the trigger conditions.

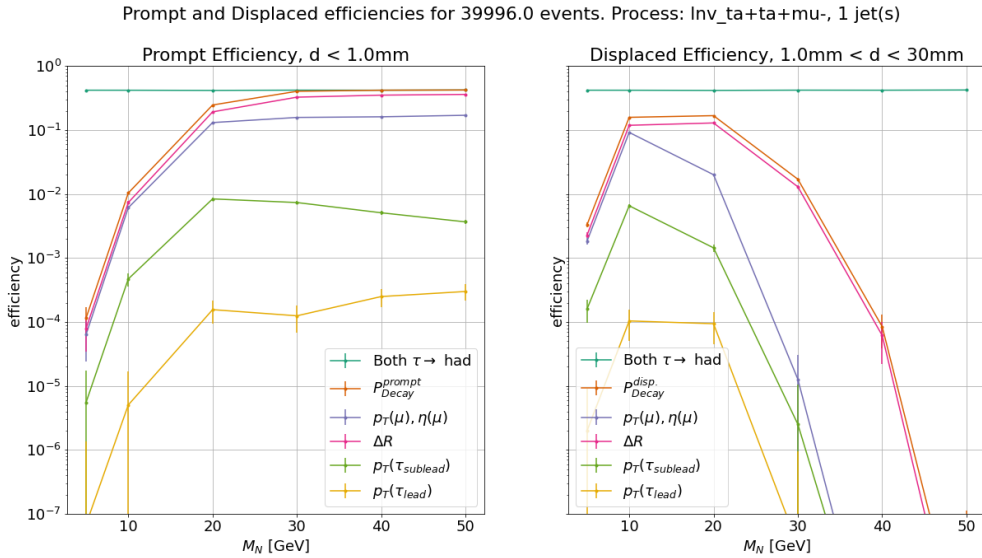


(b) Cut flow diagram with the same end result as the one in Fig. C.1a, but where the prompt (*left*) and displaced (*right*) decay weights are applied immediately after the branching ratio, $(\text{BR}(\tau \rightarrow \text{hadrons}))^2$. This is done to illustrate the shape of the decay probability curves, unobscured by the efficiencies after cuts and trigger requirements.

Figure C.1.: Estimated prompt (*left*) and displaced(*right*) efficiencies for detection of the tri-lepton signature $\tau^+\tau^+\mu^-$ in the ATLAS detector, allowing for no hard jets. The branching ratio, cuts and trigger requirements are those described in Sec. 8.2, and the decay weights are calculated as outlined in Sec. 8.3. Each value of M_N marked with a data point represents a simulation of 40.000 events. The displacement demarcations used are: *Prompt* $d < 1.0\text{mm}$ and *displaced* $1.0\text{mm} < d < 30.0\text{mm}$.



(a) Cut flow diagrams of estimated efficiencies identical to the centre panel in Fig. 8.7, with the final addition of prompt (*left*) and displaced (*right*) decay weights for each event passing the trigger conditions.



(b) Cut flow diagram with the same end result as the one in Fig. C.2a, but where the prompt (*left*) and displaced (*right*) decay weights are applied immediately after the branching ratio, $(\text{BR}(\tau \rightarrow \text{hadrons}))^2$. This is done to illustrate the shape of the decay probability curves, unobscured by the efficiencies after cuts and trigger requirements.

Figure C.2.: Estimated prompt (*left*) and displaced(*right*) efficiencies for detection of the tri-lepton signature $\tau^+\tau^+\mu^-$ in the ATLAS detector, allowing for up to 1 hard jet. The branching ratio, cuts and trigger requirements are those described in Sec. 8.2, and the decay weights are calculated as outlined in Sec. 8.3. Each value of M_N marked with a data point represents a simulation of 40.000 events. The displacement demarcations used are: *Prompt* $d < 1.0\text{mm}$ and *displaced* $1.0\text{ mm} < d < 30.0\text{ mm}$.

Solving for Single Event Sensitivity

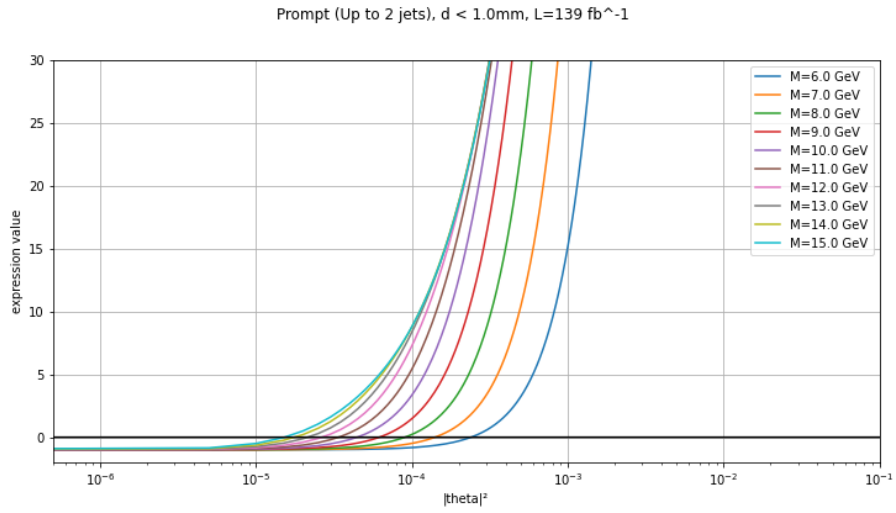
Figures D.1 and D.2 showing the expression from Eq. (8.5.2):

$$N_P - 1 = \mathcal{L} \times \sigma_{\text{MC}}^{(P)} \times \frac{|\theta_{N\tau}|^4}{|\theta_{\text{ref}}|^2} \times \frac{\Gamma_{\text{ref}}}{\Gamma_N(M_N, \theta_\tau)} \times \text{BR}(\tau \rightarrow \text{had})^2 \times \epsilon_{\text{detector}} \times P_{\text{Decay}} - 1, \quad (\text{D.0.1})$$

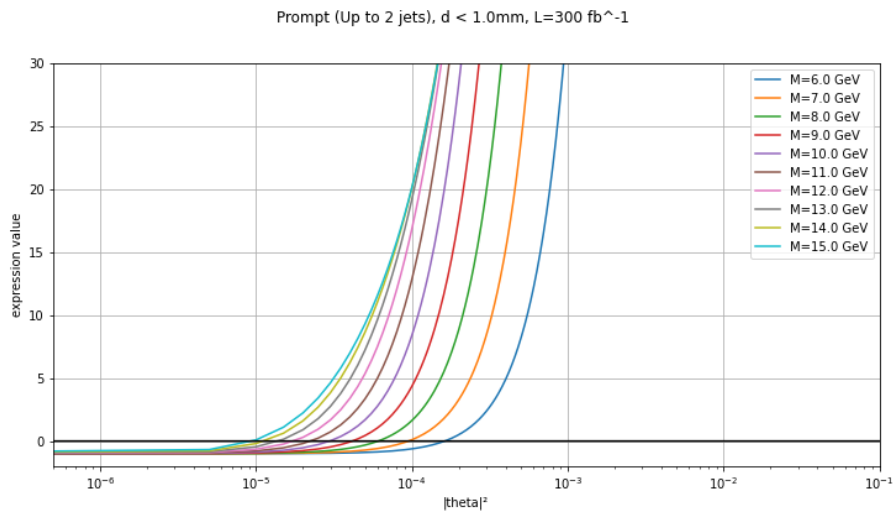
where the decay probabilities of prompt and displaced decays respectively are given by:

$$P_{\text{Decay}}^{\text{Prompt}} = 1 - \exp\left(-\frac{d_{\text{min}}}{\gamma c \tau_{\text{SI}}}\right) \quad (\text{D.0.2})$$

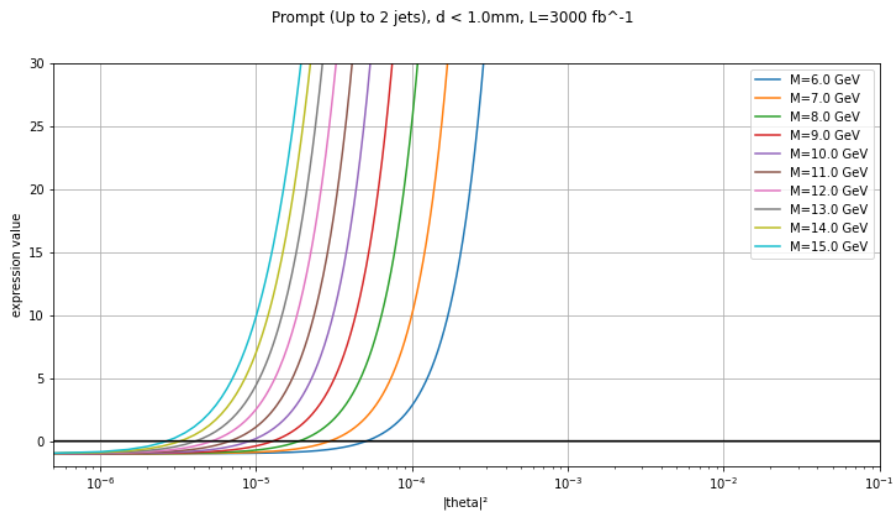
$$P_{\text{Decay}}^{\text{Disp.}} = \exp\left(-\frac{d_{\text{min}}}{\gamma c \tau_{\text{SI}}}\right) - \exp\left(-\frac{d_{\text{max}}}{\gamma c \tau_{\text{SI}}}\right), \quad (\text{D.0.3})$$



(a) Integrated luminosity: $\mathcal{L} = 139\text{ fb}^{-1}$.

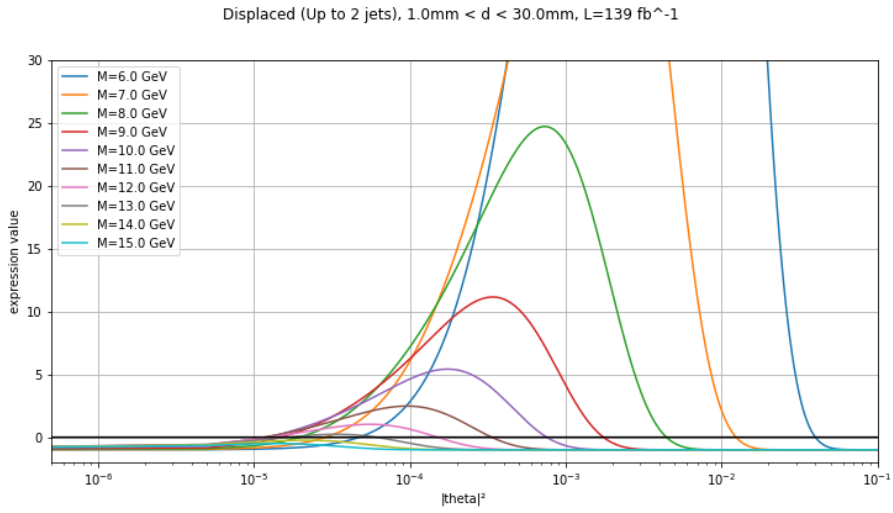


(b) Integrated luminosity: $\mathcal{L} = 300\text{ fb}^{-1}$.

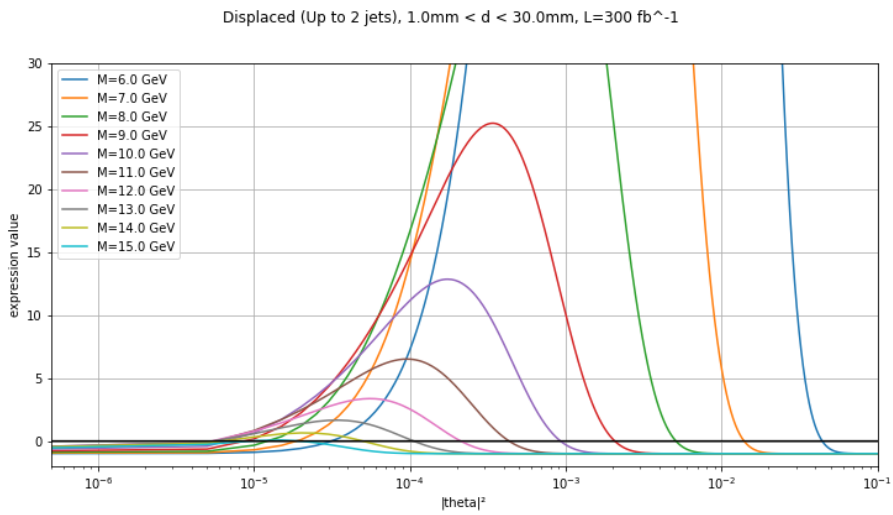


(c) Integrated luminosity: $\mathcal{L} = 3000\text{ fb}^{-1}$.

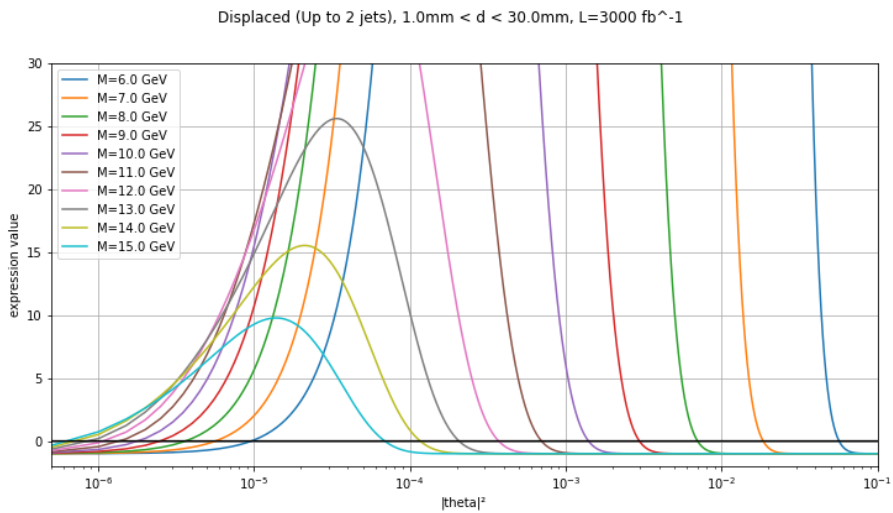
Figure D.1.: Eq. (D.0.1) in the prompt case, plotted for a range of M_N and integrated luminosities. The maximum displacement is taken to be 1 mm.



(a) Integrated luminosity: $\mathcal{L} = 139\text{ fb}^{-1}$.



(b) Integrated luminosity: $\mathcal{L} = 300\text{ fb}^{-1}$.



(c) Integrated luminosity: $\mathcal{L} = 3000\text{ fb}^{-1}$.

Figure D.2.: Eq. (D.0.1) in the displaced case, plotted for a range of M_N and integrated luminosities. The minimum displacement is taken to be 1 mm, and the maximum 30 mm.